

UCGE Reports

Number 20300

**Department of Geomatics Engineering**

**Use of Wheel Speed Sensors to Enhance a Reduced IMU  
Ultra-Tight GNSS Receiver**  
(URL: <http://www.geomatics.ucalgary.ca/graduatetheses>)

**by**

**Tao Li**

December 2009



UNIVERSITY OF CALGARY

USE OF WHEEL SPEED SENSORS TO ENHANCE A REDUCED IMU

ULTRA-TIGHT GNSS RECEIVER

by

TAO LI

A THESIS

SUBMITTED TO THE FACULTY OF GRADUATE STUDIES

IN PARTIAL FULFILMENT OF THE REQUIREMENTS FOR THE

DEGREE OF MASTER OF SCIENCE

GEOMATICS ENGINEERING

CALGARY, ALBERTA

DECEMBER 2009

© Tao Li (2009)

## **Abstract**

With the increasing demand for land vehicle navigation, modern vehicle systems are often equipped with Global Positioning System (GPS) receivers and vehicle sensors to provide position, velocity and attitude information. However, for cost sensitive applications, instead of using a full six degree of freedom Inertial Measurement Unit (IMU), vehicle sensors normally consist of low cost reduced MEMS (Micro-Electro-Mechanical Systems) IMU sensors. Typical vehicle sensor setups have two horizontal accelerometers and one vertical gyroscope along with individual wheel speed sensors. This is the setup assumed in this thesis, whose main objective is to study various ultra-tight methods of integrating GPS with full and reduced inertial sensors and other vehicle sensors.

A pseudo-signal approach is employed for the reduced IMUs. The unavailable output signals of the reduced IMU (i.e., vertical accelerometer and horizontal gyros) are replaced by pseudo signals that have constant values. Therefore, the outputs of the vertical accelerometer are assumed as gravity and the two horizontal gyros are assumed as zero. Then these pseudo signals combined with the real horizontal accelerometer and vertical gyro outputs are fed into the full IMU/GPS navigation algorithm to obtain the final navigation solution.

In order to limit the errors induced by the reduced MEMS IMU/GPS integrated system, a wheel speed sensor and non-holonomic constraints derived three-dimensional velocity updates are applied. The 3D velocity updates improve the velocity and attitude estimates of the integration filter. The improved positioning estimates in turn help the receiver

carrier tracking loops. The benefits of each constraint including the vertical, lateral and longitudinal ones are investigated.

A field test is conducted under different operational environments to evaluate the performance of the ultra-tightly coupled GPS/vehicle sensor system. The analysis is performed in both the GPS signal tracking domain and navigation domain. In the tracking domain, phase lock indicators (PLIs) are used to evaluate the carrier phase tracking ability. In the navigation domain, the root mean square position, velocity and attitude errors are used to assess the performance of the navigation solutions. The above performance parameters are compared between different receiver architectures including the standard GPS receiver (without attitude information) and the ultra-tightly coupled GPS receiver with different IMUs.

## **Acknowledgements**

First of all, I would like to thank my supervisor, Dr. Gérard Lachapelle for his guidance, support and continuous encouragement during my studies. Further, I would like to express my gratitude to my co-supervisor, Dr. Mark Petovello. He leads me into the world of the GNSS navigation. His knowledge and patient supervision helps me to finish my master degree. I would like to acknowledge all the other examining committee members Dr. Kyle O’Keefe and Swavik Spiewak for taking time to read the draft.

The financial support of General Motors of Canada, the Natural Science and Engineering Research Council of Canada, Alberta Advanced Education and Technology and the Western Economic Diversification Canada is also acknowledged.

Special thanks to Dr. Debo Sun, he always kindly solves my problems and answers my questions. I am also grateful to those graduate students Jared Bancroft, Tao Lin, Peng Xie, Da Wang, Ping Luo in the PLAN group who helped my field test, shared the discussions and answered my questions.

Finally, and most importantly, I would like to thank my parents, for their unconditional love, encouragement and understanding through all of my years. This work would not have been possible without their support.

## Table of Contents

Abstract.....	iii
Acknowledgements.....	v
List of Tables .....	x
List of Figures.....	xi
Notation.....	xiv
CHAPTER ONE: INTRODUCTION.....	1
1.1 BACKGROUND .....	1
1.1.1 GPS/INS integration strategies.....	1
1.1.2 Integration of GPS / reduced IMU .....	4
1.1.3 Integration of GPS / INS / wheel speed sensor .....	5
1.1.4 Tracking loops.....	7
1.2 PREVIOUS RESEARCH AND ASSOCIATED LIMITATIONS.....	10
1.3 OBJECTIVES AND TASKS.....	12
1.4 THESIS OUTLINE.....	14
CHAPTER TWO: REVIEW OF GPS RECEIVER.....	16
2.1 GENERAL GPS RECEIVER ARCHITECTURE .....	16
2.2 GPS FRONT-END.....	19
2.3 ACQUISITION.....	21
2.4 TRACKING.....	23
2.4.1 Standard GPS receiver.....	24
2.4.2 Estimator-based GPS receiver.....	25
2.4.3 Vector-based GPS receiver.....	27

2.4.4 Ultra-tight GPS receiver .....	29
CHAPTER THREE: ULTRA-TIGHTLY COUPLED GPS/INS INTEGRATION .....	31
3.1 OVERVIEW OF INERTIAL NAVIGATION SYSTEM.....	31
3.1.1 Coordinate frames and transformations.....	32
3.1.2 Mechanization equations .....	37
3.2 OVERVIEW OF INS/GPS INTEGRATION STRATEGIES .....	43
3.2.1 Loosely coupled integration .....	43
3.2.2 Tightly coupled integration .....	45
3.3 ULTRA-TIGHT GPS/INS INTEGRATION .....	46
3.3.1 Extended Kalman filter (EKF) .....	48
3.3.2 INS error models .....	54
3.3.3 GPS error models .....	58
3.3.4 GPS/INS integration filter .....	59
3.3.5 Channel filter .....	63
3.3.6 Vector-based NCO updates .....	69
CHAPTER FOUR: ULTRA-TIGHTLY COUPLED GPS /VEHICLE SENSOR INTEGRATION .....	72
4.1 OVERVIEW OF VEHICLE SENSORS .....	72
4.1.1 MEMS IMU .....	74
4.1.2 Wheel speed sensor .....	76
4.2 IMU NOISE CHARACTERIZATION.....	78
4.2.1 Sensor model .....	78
4.2.2 Allan variance.....	80

4.3 ULTRA-TIGHT INTEGRATION OF GPS/REDUCED IMU.....	84
4.4 ULTRA-TIGHT INTEGRATION OF WHEEL SPEED SENSOR.....	88
4.4.1 Non-holonomic constraints .....	88
4.4.2 Three-dimensional velocity updates.....	90
CHAPTER FIVE: FIELD TEST RESULTS AND PERFORMANCE ANALYSIS .....	96
5.1 FIELD TEST DESCRIPTION.....	96
5.1.1 Equipment setup .....	96
5.1.2 Test environments .....	99
5.2 DATA PROCESSING.....	104
5.2.1 Reference solution.....	104
5.2.2 Noise identification of the production IMU .....	104
5.2.3 Filtering raw wheel speed sensor outputs.....	107
5.2.4 Data processing summary.....	108
5.3 DATA ANALYSIS STRATEGIES.....	109
5.4 OPEN SKY TEST RESULTS .....	111
5.4.1 Tracking domain.....	111
5.4.2 Navigation domain .....	118
5.5 FOLIAGE TEST RESULTS.....	133
5.5.1 Tracking domain.....	133
5.5.2 Navigation domain .....	140
CHAPTER SIX: CONCLUSIONS AND RECOMMENDATIONS .....	147
6.1 CONCLUSIONS.....	148
6.2 RECOMMENDATIONS .....	149

REFERENCES .....152

## List of Tables

Table 4.1: Specifications of different IMUs .....	75
Table 4.2: Relationship between Allan variance and different errors .....	83
Table 5.1: Identified noise parameters using Allan variance.....	106
Table 5.2: Velocity and attitude error for full Crista IMU .....	122
Table 5.3: Standard Deviations of three-dimensional velocity updates .....	123
Table 5.4: RMS position errors for full Crista IMU .....	124
Table 5.5: Velocity and attitude errors for reduced Crista IMU.....	127
Table 5.6: RMS position errors for reduced Crista IMU .....	127
Table 5.7: Velocity and attitude errors for the production IMU.....	129
Table 5.8: RMS position errors for the production IMU .....	130
Table 5.9: Velocity and attitude errors for reduced HG1700 .....	131
Table 5.10: RMS position errors for reduced HG1700.....	132
Table 5.11: RMS Position and velocity errors for standard GPS .....	132
Table 5.12: Velocity and attitude errors for full Crista IMU .....	143
Table 5.13: RMS position errors for full Crista.....	143
Table 5.14: Velocity and attitude errors for reduced IMUs.....	145
Table 5.15: RMS position errors for reduced IMUs.....	145
Table 5.16: RMS Position and velocity errors for standard GPS .....	146

## List of Figures

Figure 2.1: Generic diagram of a software based GPS receiver (Tsui 2000) .....	17
Figure 2.2: Block diagram of a GPS Front-end (Modified from Kaplan, 1996) .....	20
Figure 2.3: Two-dimensional C/A code search (Modified from Kaplan, 1996) .....	22
Figure 2.4: Standard GPS receiver architecture.....	25
Figure 2.5: Estimator-based GPS receiver architecture .....	26
Figure 2.6: Vector-based GPS receiver architecture.....	28
Figure 2.7: Ultra-Tight GPS receiver architecture.....	29
Figure 3.1: Local level frame and ECEF frame .....	34
Figure 3.2: Body frame and vehicle frame .....	35
Figure 3.3: Local level frame (l-frame) INS mechanizations .....	42
Figure 3.4: Block diagram of loosely coupled integration .....	44
Figure 3.5: Block diagram of tightly coupled integration.....	45
Figure 3.6: EKF computation procedure .....	53
Figure 3.7: Structure of EKF based tracking loop .....	64
Figure 4.1: Typical vehicle sensor configurations (Modified Bosch 2009) .....	73
Figure 4.2: Operation principles of wheel speed sensor .....	77
Figure 4.3: Clusters used for Allan variance computation .....	80
Figure 4.4: Outputs of full IMU during typical vehicle dynamics .....	84
Figure 4.5: Histogram plot of Z-acceleration outputs.....	85
Figure 4.6: Histogram plot of horizontal gyro outputs .....	86
Figure 4.7: Pseudo-signal approach for reduced IMU.....	87
Figure 4.8: Block diagram of filter updates using non-holonomic constraints.....	89
Figure 4.9: Block diagram of filter updates using 3D velocity constraints .....	90

Figure 4.10: Simplified vehicle model.....	93
Figure 5.1: Schematic of vehicle equipment setup .....	98
Figure 5.2: Equipment setup .....	99
Figure 5.3: Open sky test environment .....	100
Figure 5.4: Satellite sky plot of open sky test.....	101
Figure 5.5: Test trajectory of the open sky scenario.....	101
Figure 5.6: Foliage test environment .....	102
Figure 5.7: Test trajectory of the foliage scenario .....	103
Figure 5.8: Satellite sky plot of foliage test .....	103
Figure 5.9: Allan deviation plot of the production gyro .....	105
Figure 5.10: Allan deviation plot of the production accelerometers .....	106
Figure 5.11: Filtered velocity from wheel speed sensor.....	107
Figure 5.12: Block diagram of data processing .....	108
Figure 5.13: PRN 20 Tracking results .....	112
Figure 5.14: Mean and standard deviation of PLI as a function of $C/N_0$ for PRN 20 ....	113
Figure 5.15: PRN 16 Tracking results .....	113
Figure 5.16: Mean and standard deviation of PLI as a function of $C/N_0$ for PRN 16 ....	114
Figure 5.17: Mean and standard deviation of PLI as a function of $C/N_0$ for PRN 20 ....	115
Figure 5.18: Mean and standard deviation of PLI as a function of $C/N_0$ for PRN 16 ....	116
Figure 5.19: Mean and standard deviation of PLI as a function of $C/N_0$ for PRN 20 ....	117
Figure 5.20: Mean and standard deviation of PLI as a function of $C/N_0$ for PRN 16 ....	117
Figure 5.21: Reference velocity plots of the open sky test.....	118
Figure 5.22: Reference attitude plots of the open sky test.....	119
Figure 5.23: PDOP and satellite number plots of the open sky test .....	119

Figure 5.24: Velocity and attitude error plots for full Crista .....	120
Figure 5.25: Velocity and attitude error plots for full Crista+3D .....	121
Figure 5.26: Velocity and attitude error plots for reduced Crista .....	125
Figure 5.27: Velocity and attitude error plots for reduced Crista + 3D .....	126
Figure 5.28: Velocity and attitude errors plots for the production IMU .....	128
Figure 5.29: Velocity and attitude error plots for the production IMU + 3D .....	129
Figure 5.30: Velocity and attitude error plots for reduced HG1700 .....	130
Figure 5.31: Tracking performance of PRN 4 .....	134
Figure 5.32: Mean and standard deviation of PLI as a function of $C/N_0$ for PRN 4 .....	135
Figure 5.33: Tracking performance of PRN 23 .....	135
Figure 5.34: Mean and standard deviation of PLI as a function of $C/N_0$ for PRN 23 ....	136
Figure 5.35: Mean and standard deviation of PLI as a function of $C/N_0$ for PRN 4 .....	138
Figure 5.36: Mean and standard deviation of PLI as a function of $C/N_0$ for PRN 23 ....	138
Figure 5.37: Mean and standard deviation of PLI as a function of $C/N_0$ for PRN 4 .....	139
Figure 5.38: Mean and standard deviation of PLI as a function of $C/N_0$ for PRN 23 ....	140
Figure 5.39: Reference velocity plots of the foliage test .....	141
Figure 5.40: Reference attitude plots of the foliage test .....	141
Figure 5.41: PDOP and satellite number plots of the foliage test .....	142
Figure 5.42: Velocity and attitude error plots for full Crista IMU .....	144

## Notation

### List of Acronyms

3D	Three-Dimensional
ADC	Analog to Digital Converter
AGC	Automatic Gain Control
C/A	Coarse / Acquisition
C/N <sub>0</sub>	Carrier to Noise Density
C3NAV2™	Combined Code and Carrier Phase for Navigation using GPS
CAN	Controller Area Network
CF	Compact Flash
CG	Center of Gravity
DAQ	Data Acquisition Device
DGPS	Differential GPS
DLL	Delay Lock Loop
DSP	Digital Signal Processor
ECEF	Earth Center Earth Fixed
EKF	Extended Kalman Filter
GNSS	Global Navigation Satellite System
GPS	Global Positioning System
GSRx-ut™	GNSS Software Navigation Receiver, Ultra-tight version
IF	Intermediate Frequency
ILANA	Aided Inertial Land Navigation System
IMU	Inertial Measurement Unit

INS	Inertial Navigation System
LLF	Local Level Frame
LNA	Low Noise Amplifier
LO	Local Oscillator
MEMS	Micro Electro-Mechanical Systems
NI	National Instruments
NCO	Numerically Controlled Oscillator
PDOP	Position Dilution of Precision
PLAN	Position, Location And Navigation
PLI	Phase Lock Indicator
PLL	Phase Lock Loop
PRN	Pseudo Random Noise
RHCP	Right Hand Circularly Polarized
RF	Radio Frequency
RMS	Root Mean Square
SD	Secure Digital
SDR	Software Defined Radio
SNR	Signal to Noise Ratio
STD	Standard Deviation
WSS	Wheel Speed Sensor
VSS	Vehicle Speed Sensor
ZUPT	Zero Velocity Update

## List of Symbols

$A$	Tracked Signal amplitude
$F(t)$	System dynamics matrix
$G(t)$	Shaping matrix
$H_{3D}$	Design matrix of 3D velocity updates
$H_k$	Design matrix at time $t_k$
$H_{ZUPT}$	Design matrix of ZUPT updates
$I$	In phase
$K_k$	Kalman gain matrix at time $t_k$
$L_{CG}^{IMU}$	Lever arm between the IMU and center of gravity (CG) of the vehicle
$M$	Meridian radius of the earth curvature
$N$	Prime vertical radius of the earth curvature
$P_{k,k-1}$	A priori covariance matrix at $t_k$
$P_{k-1}$	<i>Posteriori</i> covariance matrix at time $t_{k-1}$
$Q$	Quadrature phase
$Q(t)$	Spectral density matrix of $\mathbf{w}(t)$
$Q_k$	Discrete process noise at $t_k$
$(R_b^l)_{i,j}$	Element at the i-th row and j-th column of the $R_b^l$ matrix
$R_b^l$	Rotation matrix from the b-frame to the l-frame
$R_e^l$	Rotation matrix from e-frame to l-frame

$R_1, R_2, R_3$	Rotation matrixes about x ,y and z axis respectively
$S_a$	Scale factor of the accelerometer
$S_g$	Scale factor of the gyro
$S_f, S_\omega$	Scale factors of accelerometers and gyros
$S_{WSS}$	Scale factor of a wheel speed sensor
$\mathbf{b}$	Accelerometer bias
$\mathbf{b}_{to}, \mathbf{d}_{to}$	Turn-on bias vector of accelerometers and gyros
$cdt$	Receiver clock drift state
$cdt_s$	Satellite clock drift
$ct$	Receive clock bias state
$ct_s$	Satellite clock bias in metres
$c\Delta d_g$	Group delay
$\mathbf{d}$	Gyroscope bias
$\mathbf{f}^b$	Specific force vector from the IMU accelerometer triad
$f^E, f^N, f^U$	Specific force expressed in the local level frame.
$f(x(t), t)$	Nonlinear function
$f_c$	Code chipping rate
$f_k, \phi_k$	Doppler and phase at the time $t_k$ .
$\mathbf{g}^l$	Earth's local gravity vector
$n_{WSS}$	Measurement noise of wheel speed sensor

$\mathbf{n}_{3D}$	Measurement noise of 3D velocity updates
$\mathbf{n}_{ZUPT}$	Measurement noise of ZUPT updates
$\mathbf{r}^l$	Position vector expressed in the l-frame
$t_{receiver}$	Receiver time
$v_{WSS}^V$	Wheel speed expressed in v-frame
$\mathbf{v}_k$	Discrete measurement noise vector
$\mathbf{v}^l$	Velocity vector expressed in the l-frame
$w_A$	Driving noise of the amplitude
$w_{\delta\tau}$	Driving noise of the code tracking error
$w_{\delta b}$	Driving noise for the clock bias
$w_{\delta l}$	Driving noise for the clock drift
$w_{\delta a}$	Driving noise to account for line-of-sight acceleration
$\mathbf{w}_{k-1}$	Driving noise vector from $t_{k-1}$ to $t_k$
$\mathbf{w}_f$	Wideband noise of an accelerometer
$\mathbf{w}_\omega$	Wideband noise of a gyroscope
$\mathbf{w}(t)$	Noise vector
$\gamma$	Normal gravity
$\delta(t)$	Dirac delta function
$\delta a$	Frequency rate error of the NCO
$\delta f$	Frequency tracking error

$\delta\mathbf{x}_{ib}^b$	Accelerometer sensor noise vector
$\delta f_{k+1}^i, \delta\phi_{k+1}$	Doppler and phase error estimates at time $t_{k+1}$ .
$\delta\mathbf{x}(t)$	Error state vector
$\delta\mathbf{x}_k$	System state (error) vector at $t_k$
$\delta\mathbf{Z}_{3D}$	Measurement misclosure of 3D velocity updates
$\delta\mathbf{Z}_k$	Measurement error vector at time $t_k$
$\delta\mathbf{Z}_{ZUPT}$	Measurement misclosure of ZUPT updates
$\delta\tau$	Code phase tracking error
$\delta\tau_{k+1}$	Code phase error estimate at time $t_{k+1}$
$\delta\phi$	Phase tracking error
$\delta\boldsymbol{\omega}_{ib}^b$	Gyroscope sensor noise vector
$\theta$	Pitch angle
$\dot{\lambda}$	Longitude rate
$\boldsymbol{\rho}_{INS}$	INS derived pseudorange vector
$\dot{\boldsymbol{\rho}}_{INS}$	INS derived pseudorange rate $\dot{\rho}_{INS}^i$ vector
$\sigma^2(T)$	Allan Variance with time cluster T
$\tau_k$	Code phase at the previous epoch at the time $t_k$
$\dot{\phi}$	Latitude rate
$\phi$	Roll angle
$\psi$	Azimuth angle

$\omega_{wss}$	Angular velocity of the wheel revolution
$\omega_{el}^l$	Transport rate
$\omega_{ib}^b$	Angular rate vector sensed by a gyroscope triad
$\omega_{ie}^l$	Earth rotation rate projected into the l-frame
$\Delta d_{tr}$	Tropospheric delay in metres
$\Delta \tilde{v}_f^b$	Velocity increments from an accelerometer outputs
$\Delta \tilde{\theta}_{ib}^b$	Angular increments from a gyro outputs
$\Phi_{k,k-1}$	State transition matrix from $t_{k-1}$ to $t_k$
$\Omega_{bc}^a$	Skew-symmetric matrix form of vector $\omega_{bc}^a$

## CHAPTER ONE: INTRODUCTION

Cost, accuracy, availability and reliability are four major concerns for land vehicle navigation. For this reason, extensive research has been dedicated to improving navigation performance and decreasing system cost in the past decades. The integration of the Global Positioning System (GPS) and Inertial Navigation System (INS) has been widely used in land vehicle navigation to provide more accurate information and to have higher availability compared to stand alone GPS or INS system.

This thesis investigates an ultra-tight integration strategy to fuse GPS and low cost inertial sensors for cost sensitive land vehicle applications. Due to the performance degradation induced by the low quality reduced inertial sensors installed in the vehicle, wheel speed sensors and non-holonomic constraints, aside from GPS, are used to constrain the INS errors. Finally, the performance of the integrated system is evaluated in different operational environments.

### 1.1 Background

#### *1.1.1 GPS/INS integration strategies*

The integration of GPS and INS improves the system accuracy, continuity, and reliability relative to either system alone due to their complimentary features (Rogers 2000). Specifically, GPS combined with INS can limit the INS error growth and provide online estimation of inertial sensor errors while INS can bridge the GPS signal gaps and improve the sensitivity and reliability of GPS receivers in degraded signal environments (Brenner 1995).

GPS/INS integration strategies can be mainly divided into loose coupling, tight coupling and ultra-tight coupling. The loose and tight couplings have been widely researched for many years (e.g., Greenspan 1996, Jekeli 2001, Shin 2001, Gautier & Parkinson 2003, Petovello 2003, Rogers 2007). With the advances of Micro Electro-Mechanical Systems (MEMS), the low cost, low power consumption and light weight of MEMS inertial sensors have been widely used in navigation applications. However, these benefits are offset by increased errors that cause a more rapid degradation in the navigation solution compared with higher quality sensors. The performance of loosely and tightly coupled MEMS IMU/GPS integration has also been investigated in recent years (Shin 2005, Godha 2006, Fujiwara et al 2007, Yang 2008).

A loosely coupled system uses the GPS and INS to produce estimates of navigation states separately. The GPS and INS estimates are then fed into a Kalman filter to produce improved state estimates and to estimate the error states of the INS (Shin 2001, Petovello 2003, Kreye et al 2004, Godha 2006, Gebre-Egziabher 2007).

A tightly coupled system combines the inertial sensors and GPS at a lower level. The raw pseudorange and pseudorange rate measurements from the GPS receiver are fed into the navigation filter. This allows the navigation filter to estimate the error states of the INS system when GPS solution is not available. Some tightly coupled systems also use the acceleration information provided by the INS to predict the Doppler shift caused by the user's dynamics. It is known as the tight integration with INS derived Doppler aiding. This improves the tracking performance of the GPS receiver and enhances its ability to

maintain lock in high dynamic environments (Kreye et al 2000, 2004, Greenspan 1996). The bandwidth of the tracking loop can also be narrowed because user dynamics can be compensated by INS (Alban et al 2003, Chiou 2005, Gebre-Egziabher 2005, Gao & Lachapelle 2006, Yang & El-Sheimy 2006, Yang 2008).

The original concept of ultra-tight integration is based on vector tracking (Spilker 1996). In this case, the individual tracking loop of each satellite is eliminated and replaced by the navigation filter. The pseudorange and pseudorange rate derived from the user's position and velocity from the filter are used to control the numerically controlled oscillators (local signal generators) of the GPS receiver (Pany et al 2005, Pany & Eissfeller 2006, Petovello et al 2008). Therefore, noise can be reduced in all channels and tracking performance can be improved in weaker signal and jamming signal environments.

The architecture of ultra-tight integration is similar to that of vector tracking except for the inclusion of INS information. Between navigation filter updates, the user's position and velocity information can be obtained by INS propagation in an ultra-tight configuration whereas in vector tracking this information can be only obtained by predicting the navigation solution forward using past estimates (Li & Wang 2006a, 2006b; Petovello et al 2006, 2008).

In order to reduce the computation burden, many studies use a federated or cascaded approach to implement the vector-based or ultra-tight receiver (Abbott & Lillo 2003; Kim et al 2003; Jovancevic et al 2004; Babu & Wang 2006; Buck et al 2006; Ohlmeyer 2006;

Petovello et al 2006, 2008). In this case, each channel has an individual Kalman filter that estimates the tracking errors for that channel.

### ***1.1.2 Integration of GPS / reduced IMU***

For cost sensitive applications of land vehicle navigation, full IMU with three accelerometers and three gyroscopes can be simplified to a reduced configuration with two accelerometers and one gyroscope or with three accelerometers and one gyroscope (Daum et al 1994, Brandit & Gardner 1998, Phuyal 2004, Niu et al 2007b, Sun et al 2008).

Daum (1994) used one gyroscope and two accelerometers in an Aided Inertial Land Navigation System (ILANA). The system also included an odometer and a GPS receiver. However, in this system, accelerometers were used to estimate roll and pitch angles, rather than to generate the vehicle velocity estimates by integration of accelerations, as is the case with regular inertial navigation systems. Such a sensor configuration is sensitive to dynamics experienced by the vehicle, yielding pitch and roll angle errors. A wheel speed sensor was used as the primary instrument for measurement of the vehicle velocity. GPS was used as an aiding source of the position, velocity, and heading information.

Brandit & Gardner (1998) used non-holonomic constraints on the motion of the land vehicles to derive a set of navigation equations for the reduced inertial sensors, namely one accelerometer and three gyroscopes. The motion of the vehicle was measured by accelerometers. In addition, a wheel speed sensor was used as a tachometer to provide

auxiliary information about the vehicle's speed. A second accelerometer was also used to provide redundant data that helps to reduce the overall system error.

Phuyal (2004) used a single gyroscope aligned vertically to measure azimuth rate and an accelerometer or a wheel speed sensor to measure the vehicle forward linear motion to form a 2-D navigation solution. Simulation results were employed to evaluate the position errors arising from ignoring the small quantities in the navigation equations.

Niu (2007b) implemented the pseudo signal approach for reduced IMU/GPS navigation systems. The main concept of this reduced IMU approach is to replace the unavailable signals by pseudo signals that have constant values plus white noise. Since land vehicles mainly run on relatively flat roads with ramps inclined typically less than 5 degrees, the output of the vertical accelerometer is assumed to be composed mainly of the local gravity plus the addition of road vibrations or undulations. A similar analysis can be applied to the two horizontal gyro case. These pseudo signals were fed into the full INS/GPS navigation algorithm to obtain the final navigation solution.

### ***1.1.3 Integration of GPS / INS / wheel speed sensor***

As per some of the above studies, a wheel speed sensor, which is standard equipment in most vehicles, can be used to further improve navigation accuracy and system redundancy (Gao 2007). The integration of a wheel speed sensor with GPS/INS has been extensively investigated during recent years. To integrate a wheel speed sensor with other sensors, the centralized and decentralized approaches have been studied by many researchers (Kubo et

al 1999, Numajima et al 2002, Clark et al 2006, Gao 2007, Gao et al 2007, Niu et al 2007a) as described in more details below.

Kubo (1999) implemented a centralized GPS/INS/Wheel speed sensor integrated system in the wander angle frame for land-vehicle positioning. The system operated in two modes, namely DGPS/INS mode and INS/Wheel speed sensor mode. When GPS was available, the accurate GPS solutions were used as measurements in the Kalman filter to calibrate wheel speed sensor and to estimate inertial sensor errors. When GPS was unavailable, the wheel speed sensor-derived velocity was used as measurements instead.

Numajima (2002) investigated the integration of DGPS/INS/Wheel speed sensor for land-vehicle in-motion alignment by using a decentralized Kalman filter. The system could do initial alignment under a large heading error when GPS signals were blocked. Clark (2006) analyzed the performance of two-wheel robot navigation using low cost GPS and INS aiding. Two wheel speed sensors were also equipped to provide both velocity and heading information. The influence of wheel slippage and radius error was investigated in their paper.

Since the wheel speed sensor only measures velocity in a forward direction, non-holonomic constraints and wheel speed sensor-derived velocity can form 3-D auxiliary velocity updates for the Kalman filter. Improvement of position and attitude accuracy can be obtained when using 3D auxiliary velocity updates in MEMS based

integrated systems (Niu et al 2007a). Shin (2001, 2005) also did some work with low-cost sensors and non-holonomic constraints.

Non-holonomic constraints applied to wheel speed sensor integration are effective only when the vehicle operates on a flat road and without side slip (Brandit & Gardner 1998, Dissanayake et al 2001); they are no longer valid when the vehicle jumps off the road or operates on an icy or bumpy road (Gao 2007, Gao et al 2007, Niu et al 2007a). In a land vehicle navigation system, the violation of non-holonomic constraints is always accompanied by larger side slip angles (Gao 2007, Niu et al 2007a). A large side slip angle that exceeds a specific threshold is usually coupled with road undulations and/or poor tire conditions, high vehicle dynamics including fast driving, sharp turns as well as high pitch and roll angular rates. Typical side slip angles range approximately from zero to 30 degrees (Ray 1995). Anderson & Bevly (2004) investigated a model-based Kalman filter with GPS velocity measurements to estimate side slip. Gao (2007) used on-board vehicle sensors to detect violations of non-holonomic constraints.

#### ***1.1.4 Tracking loops***

Tracking loops play an important role in the operation of a GPS receiver. Tracking loops allow the ephemeris information (broadcast by the GPS satellites) to be decoded and used to determine the position of satellites. They are also used to generate the pseudorange measurements for computing the user's position (Lashley & Bevly 2006). In the receiver's tracking loop, the Phase Lock Loops (PLLs) are used to track the carrier

Doppler on each satellite while Delay Lock Loops are used to track the code phase offsets.

Tracking characteristics of a PLL are mainly determined by the design of the loop filter (Van Dierendonck 1996). The response of the PLL to its inputs is very important. The inputs are considered to represent the dynamics of the received signals which are a function of the receiver's position, velocity, and acceleration. A change in position can be represented as a change in the phase of the received signals. A change in velocity results in the relative Doppler frequency shift between the satellite and the receiver. The frequency variations of the received signal can be translated into phase ramps. Therefore, only third and higher order loops can track frequency ramps (Hamm et al 2004). However, third and higher order loops are not unconditionally stable (Best 1999, Gao & Lachapelle 2006).

It is obvious that one of the major drawbacks of tracking loops is their limited ability to track the dynamics of the relative motion between the receiver and satellites. This can cause the tracking loops to lose lock during high dynamic manoeuvres. In order to improve the response of the tracking loops to platform dynamics, the bandwidth of the loop filter must be increased. However, this also increases the amount of noise passed by the filter, thus degrading measurement accuracy. A second shortcoming of conventional tracking loops is that they employ fixed bandwidths and gains regardless of high or low Signal to Noise Ratio (SNR) of received signals. In practice, the SNR is different depending on the operational environment (Yu 2007, Yu et al 2006). In the extreme case

when a satellite is blocked, the tracking loops are in a state of random walk (Van Dierendonck 1996). Some research has been done to improve carrier tracking performance in dynamic environments by using adaptive bandwidth PLL (Legrand & Macabiau 2001, Lian 2004). However, the adaptive PLL algorithm is restricted to high SNR and low dynamics environments (Lian 2004).

A Kalman filter has the capacity to overcome the drawbacks of the conventional tracking loops. The Kalman filter is, in essence, a filter with time varying gains. The gains vary with the changing measurement noise statistics and process noise statistics. The measurement noise statistics vary with SNR levels whereas the process noise statistics vary with user dynamics. Given the process and measurement noise covariance matrices, the Kalman filter can optimally estimate the states of interest and separate them from noise (Grewal & Andrews 1993, 2001; Brown & Hwang 1992, Gelb 1974). The code tracking and carrier tracking can be combined into one Kalman filter, which replaces the two tracking loops for each channel with a single Kalman filter per satellite (Grewal & Andrews 2001). The measurements and system models for Kalman filter-based tracking have been investigated by many researchers (e.g., Petovello et al 2006, Humphreys et al 2005, Ziedan & Carrison 2004, Jee et al 2003, Psiaki & Jung 2002, Psiaki 2001).

Similarly, the vector based tracking operates by using an Extended Kalman Filter (EKF) to estimate the user's position, clock bias, and clock drift, which allows the code offsets of the PRN sequences to be predicted. The user's position can be determined by using

information from the stronger signals present. Thus the weaker signals can be accurately estimated based on the states of the EKF (Petovello et al 2008, 2008; Spilker 1996).

## **1.2 Previous Research and Associated Limitations**

Studies involving low cost MEMS IMU that have been conducted during the last few years have been mainly concentrated on the loosely and tightly coupled integration (Li et al 2006, Shin 2005, Godha 2006). Yang (2008) studied MEMS-based INS aided GPS receiver using tight integration, however, only conventional PLL tracking loops and 1 ms integration time were used. In order to fully examine the performance of INS aided tracking loop, both Kalman filter-based and conventional tracking should be investigated. Besides, longer integration time might help to evaluate performance of tracking under weaker signal environments.

Ultra-tight integration of low cost IMU have not been fully investigated (Beser 2002, Gunawardena et al 2004, Babu & Wang 2006). Previous research on the ultra-tight integration is mainly based on tactical grade IMU or simulated IMU outputs (Brown et al 2005, Babu & Wang 2006, Petovello et al 2007, Soloviev et al 2007, Li & Wang 2006, Petovello et al 2008). Although both simulations and the field test results proved that the quality of the IMU plays a minimal role on overall channel filter performance compared to the influence of the oscillator (O'Driscoll et al 2008, Petovello et al 2008), it is still important to compare the obtained navigation solutions between ultra-tight and tight integration, especially in degraded signal environments.

Similarly, for the reduced IMU/GPS integration, current research is focused on loosely coupled integration (Phuyal 2004, Niu et al 2007b, Sun et al 2008); ultra-tight integration with reduced IMU has not been widely investigated. Besides, comprehensive analysis of performance degradation using reduced IMU configuration has not been conducted until recently (Phuyal 2004, Niu et al 2007b, Petovello et al 2007, Yang 2008). The impact of omitted sensors on the tracking loops still needs to be investigated.

Moreover, although integration of wheel speed sensors has been widely used in land vehicle navigation with full IMU configuration (Kubo et al 1999, Gao 2007, Niu et al 2007a, Spangenberg et al 2007), performances of wheel speed sensor aiding with reduced IMU configurations have not been studied. Gao (2007) used on-board vehicle sensors to avoid performance degradation due to violations of non-holonomic constraints, however fault detection techniques without additional sensor aiding is also necessary to reduce the system cost.

The operational environment of a navigation system plays an important role in the quality of derived solutions (Petovello 2003). In most previous studies on ultra-tight integration, the performance in urban environments is more commonly quantified by simulated degraded signals using attenuators. It is generally not representative of performance in actual foliage environments (Godha 2006). The reason for this is two-fold. First, GPS outages in foliage environments vary in frequency, duration, and are often a blend of complete and partial outages. Second, in actual conditions GPS data (when available) is degraded primarily by poor satellite geometry, low  $C/N_0$  and multipath (Lachapelle 2007).

Such problems cause large measurement errors that can introduce a bias in the estimated parameters (Petovello 2003). In simulation mode however, the GPS data before and after the simulated outage is mostly clean and fault free; so, the results obtained by simulation of a GPS outage are likely to be optimistic relative to the actual performance of standalone INS in urban canyon environments (Godha 2006).

### **1.3 Objectives and Tasks**

The main objective of this thesis is to use wheel speed sensors to enhance the performance of ultra-tightly coupled integration with low cost reduced MEMS IMUs. Reduced MEMS sensors are used because of their low cost, low power consumption, light weight and small size and thus increased applicability to commercial land vehicle navigation. The tracking performance of this system including carrier frequency and carrier phase tracking are given special considerations. Different operational environments especially in degraded signal reception will help to fully study the stability and robustness of the tracking loops.

A field test is conducted to evaluate the performance of the ultra-tightly coupled GPS receiver under actual driving conditions. A 2009 GMC Acadia from General Motors (GM) is used as the test vehicle. The GPS Intermediate Frequency (IF) samples are collected by a front-end designed by National Instruments (NI). The raw GPS pseudorange and Doppler measurements together with tactical grade IMU (HG1700) measurements are used with a NovAtel OEM4 GPS receiver in order to generate reference solution. A data acquisition program is developed to collect an external production IMU outputs via an NI

multi-function Data Acquisition Device (DAQ) and onboard vehicle sensor outputs via a Controller Area Network (CAN) receiver.

A post mission processing procedure to integrate GPS, MEMS IMUs and vehicle sensors in ultra-tight mode is used to generate the positioning and tracking domain results for the purpose of performance analysis. The algorithms of the vehicle sensor integration and 3D velocity updates are implemented in GSNRx-ut™, which is an ultra-tight software GNSS receiver developed by the PLAN group of the University of Calgary.

The specific objectives and tasks are as follows:

1. *To implement and analyze the performance of ultra-tight coupled integration with full MEMS IMU.* Taking into account the large turn-on bias and scale factors of MEMS sensors, new states are added to current navigation filters of an ultra-tight receiver. In order to evaluate the performance of this system, the tracking performance is assessed in terms of carrier frequency tracking and carrier phase tracking; the accuracy of navigation solution including position, velocity and attitude accuracy is also be analyzed. Results from ultra-tight integration with HG1700 are also be used as a reference.

2. *To implement and analyze the performance of ultra-tight coupled integration with reduced tactical grade IMU and with MEMS IMU.* A pseudo signal approach is used in this work. Similar data analysis strategies are applied to the ultra-tight integration of reduced IMU. To compare the results between full and reduced IMU integration, the

accuracy of reduced system and major effects that leads to performance degradation are estimated and analysed.

3. To investigate performance improvement in ultra-tight coupled integration when using non-holonomic constraints and a wheel speed sensor. 3D velocity updates, as mentioned earlier, are employed in this work to improve the position velocity and attitude accuracy of MEMS-based INS systems. The contributions of the lateral, vertical and wheel speed sensor derived velocity updates to the navigation solution are analyzed, respectively. Furthermore, the performance of the 3D velocity updates is also analyzed in the signal tracking domain.

4. *To evaluate the performance of the integrated system in different operating environments.* Both tracking performance and accuracy of navigation solution are analyzed by using field test data. The tracking performance is analyzed in light of Doppler accuracy, phase lock indicator and estimated carrier to noise density. The accuracy of navigation solution is also assessed in terms of position, velocity and attitude.

#### **1.4 Thesis Outline**

Chapter Two provides an overview of different structures of GPS receivers. The conventional GPS signal processing techniques are introduced including acquisition, tracking, and measurements generations. In terms of the tracking loop structure, the standard, estimator based, vector based and ultra-tight GPS receivers are reviewed and compared. Their advantages and disadvantages are investigated.

Chapter Three provides the implementation details of ultra-tight coupled GPS/INS integration. A general overview of INS and different GPS/INS integration strategies is presented. The extended Kalman filter based system and measurement model used for GPS/INS integration are explained in detail. In addition, the vector-based tracking loop feed back from the integrated navigation solution is introduced.

Chapter Four focuses on the ultra-tightly coupled integration of GPS and vehicle sensors. The sensor error model for MEMS IMUs used in this thesis is introduced. The concept of the pseudo signal approach used for reduced IMU integration is reviewed. The non-holonomic constraints and wheel speed sensor derived 3D velocity updates are explained in detail.

Chapter Five provides the field test descriptions and presents the results in different operational environments. Both tracking performance and accuracy of navigation solution are analyzed with different receiver architectures and different sensor configurations.

Chapter Six summarizes the work presented in this thesis, and draws conclusions from the test results and analysis. Several recommendations for the future work are also presented.

## CHAPTER TWO: REVIEW OF GPS RECEIVER

This chapter provides an overview of the concept of a GPS receiver and the operations it performs. In a GPS receiver the signal is processed to obtain the carrier Doppler, carrier phase and code phase, which in turn is used to calculate the user position and velocity. Therefore, the operations of a GPS receiver can be divided into two domains: the signal processing domain and navigation domain. This chapter starts with the introduction of a general GPS receiver architecture in Section 2.1. Then the principles of the front-end, acquisition and tracking are described in Sections 2.2, 2.3 and 2.4 respectively. In Section 2.4, the standard, estimator-based, vector-based, and ultra-tight receiver architectures are presented along with a brief discussion of their advantages and disadvantages.

### 2.1 General GPS Receiver Architecture

Modern GPS receiver designs are evolving rapidly towards using higher and higher levels of integrated circuits. Also, as microprocessors or Digital Signal Processors (DSP) become more and more powerful and cost effective, the principles of Software Defined Radios (SDR) are used to design and implement GPS receivers to decrease the development time and improve flexibility (Kaplan 1996). A high-level block diagram of a modern generic software based GPS receiver which is used to represent a general GPS receiver architecture is shown in Figure 2.1.

The GPS Radio Frequency (RF) signals of all satellites in view are received by a Right Hand Circular Polarization (RHCP) antenna with nearly a hemispherical (i.e., above the local horizon) gain pattern. In the front-end portion shown in the upper block of Figure

2.1, the RF signals are prefiltered, amplified and down-converted to Intermediate Frequency (IF) signals. At the end of the front-end block, IF signals are sampled by the Analog to Digital (A/D) converter into digital IF signals (Kaplan 1996, Van Dierendonck 1996).

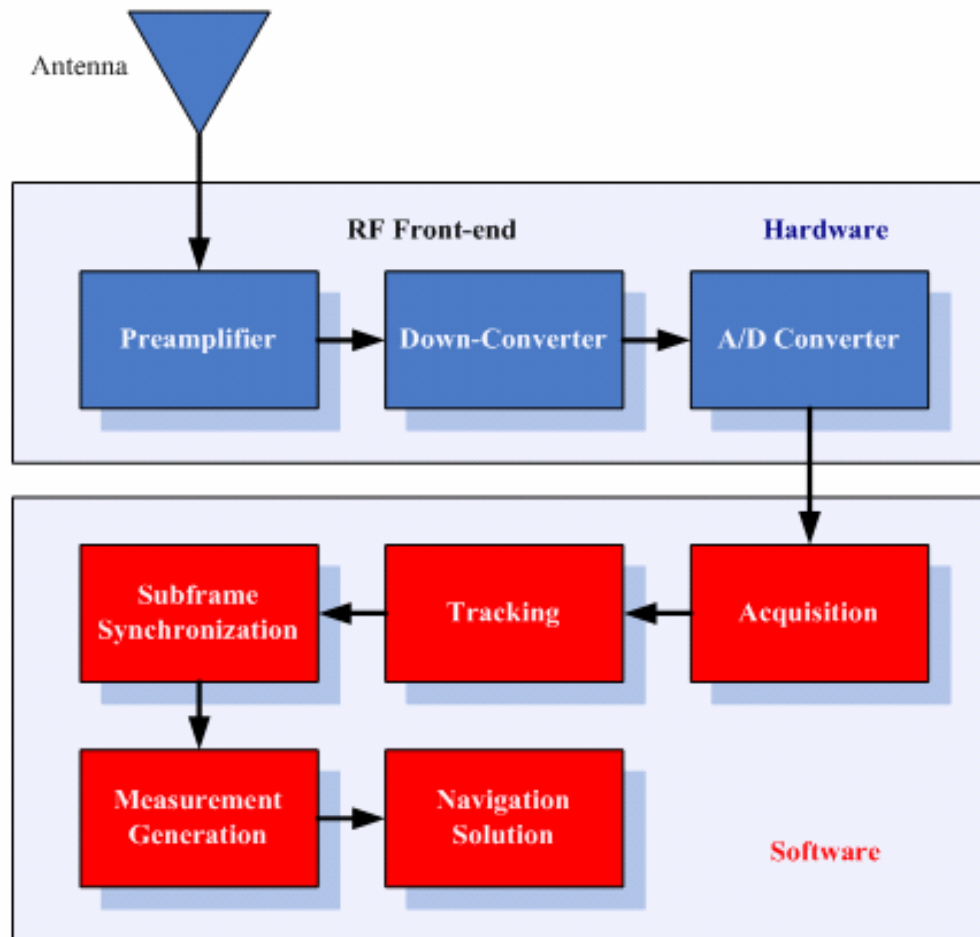


**Figure 2.1: Generic diagram of a software based GPS receiver (Tsui 2000)**

Then, the down-converted and sampled IF signals are processed by the software receiver shown in the bottom part of Figure 2.1. In order to find out which satellites are in view, the digitized IF signals go through an acquisition process. If a satellite is visible, the acquisition gives rough estimates of the satellite's Doppler frequency and code phase. The

Doppler frequency is caused by the relative motion between the satellite and the receiver. For high dynamics applications, the maximum Doppler approaches as high as 10 kHz; for a stationary receiver on Earth, the Doppler frequency shift will never exceed 5 KHz (Tsui 2000). The code phase denotes the point in the current received signal where the C/A code begins.

The acquisition provides only rough estimates of the Doppler frequency and code phase parameters. The main purpose of tracking is to refine these estimates, keep tracking the change of carrier Doppler, carrier phase and code phase, demodulate the navigation data from the specific satellite and generate measurements for navigation solution. The input signal is first multiplied with a local carrier replica to wipe off the carrier wave from the signal. Then, the code wipe-off is obtained by multiplication with a local code replica. Finally, the navigation messages can be demodulated after the carrier and code wipe-off. So the tracking block has to generate two local replicas, one for the carrier and the other for the code, to perfectly track and demodulate the signal of one satellite.

When the local signals are properly aligned with the incoming signal, the C/A code and the carrier wave can be removed completely, leaving only the navigation data bits. The value of a data bit is found by integrating over a navigation bit period of 20 ms. After reading adequate data, the beginning of a subframe must be found in order to find the time when the data was transmitted from the satellite. The time of transmission is then obtained and the ephemeris data for the satellite is decoded, which is used later to calculate the position of the satellite at the time of transmission.

The pseudorange measurements are then generated based on the time of transmission from the satellite and the time of arrival at the receiver. The code phase can be used to calculate the satellite transmit time, which can be used to compute the pseudorange measurements. Doppler and carrier phase measurements can be obtained from the carrier tracking loops directly (Kaplan 1996).

Finally, the navigation algorithm incorporates the GPS raw measurements with the GPS satellite orbit information to generate position and velocity estimates. The estimator, which could be least-squares or Kalman filter, is used to estimate the required positioning parameters. The typical estimated states of a GPS receiver are three position and velocity components, the receiver clock bias and the clock drift. In case of the GPS/INS integration, some extra states such as attitude and inertial sensor biases and drifts could be included in the navigation estimator (Petovello 2003, Godha 2006).

## **2.2 GPS Front-end**

The GPS front-end is the only hardware used within the design concept of SDR. The general block diagram of a GPS front-end is shown in Figure 2.2. The RF signals are amplified by a Low Noise Amplifier (LNA), which effectively determines the noise figure of the receiver. A passive bandpass prefilter between the antenna and LNA may be used to minimize out-of-band RF interference. It is noted that sometimes the LNA is included in the GPS antenna. This kind of antennas is called active antennas.

Then, these amplified and prefiltered RF signals are down-converted to IF signals using mixing frequencies from Local Oscillators (LOs). The LOs are derived from the reference oscillator by the frequency synthesizer, based on the frequency plan of the receiver design. The LO signal mixing process generates both upper and lower sidebands of the signals, hence the lower sidebands are selected and the upper sidebands and leak-through signals are filtered out by a post-mixer bandpass filter (Kaplan 1996). The Doppler of the satellites resulting from the relative motion and clock drift are preserved after the mixing process. Only the carrier frequency is lowered, the Doppler remains referenced to the original L-band signal.

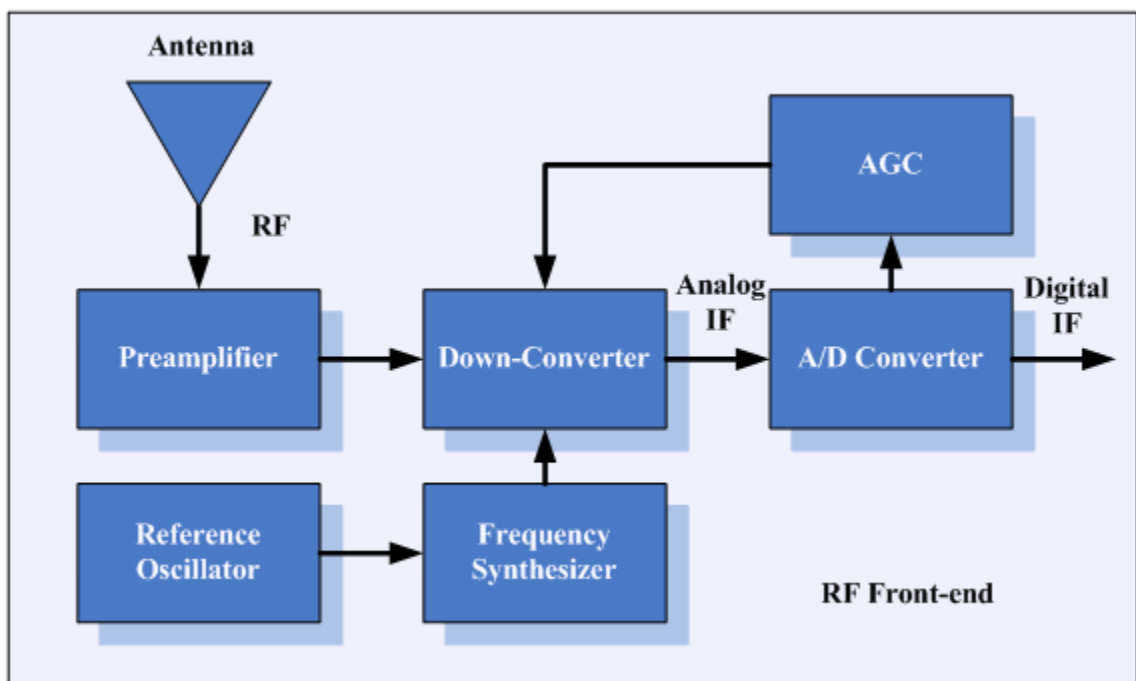


**Figure 2.2: Block diagram of a GPS Front-end (Modified from Kaplan, 1996)**

The A/D conversion process and Automatic Gain Control (AGC) functions take place at IF. The sampling frequency must be high enough to provide a single-sided bandwidth that

will support the PRN code chipping frequency (Kaplan 1996). An anti-aliasing filter must be used to suppress the unwanted out-of-band noise to levels which are considerably low when this noise is aliased into the GPS signal pass-band by the A/D conversion process. The signals from all GPS satellites in view are buried in thermal noise at IF (Kaplan 1996, Van Dierendonck 1996)

### **2.3 Acquisition**

GPS signal acquisition is a search process to detect visible satellites. This search process attempts different combinations of locally generated code and the carrier of the satellite to acquire the signal. The range dimension is associated with the replica code where as the Doppler dimension is associated with the replica carrier. The initial C/A code search usually tries all the 1,023 C/A code phases in the range dimension. If the range and Doppler uncertainty are known, then the search pattern should cover the 3-sigma values of the uncertainty (Kaplan 1996). If the uncertainty is large in either or both dimensions, the search space is correspondingly large, and the expected search time increases. Some criteria such as tone search detector and M of N search detector must be used to determine when to terminate the search process for a given satellite and select another candidate satellite (Kaplan 1996).

The code phase is typically searched in increments of  $1/2$  chip. Each code phase search increment is a code bin. Each Doppler bin is roughly  $2/3T$  Hz, where T is the search dwell time or integration time (the longer the dwell time, the smaller the Doppler bin). The

combination of one code bin and one Doppler bin is a cell. Figure 2.3 illustrates the two-dimensional search process (Kaplan 1996).

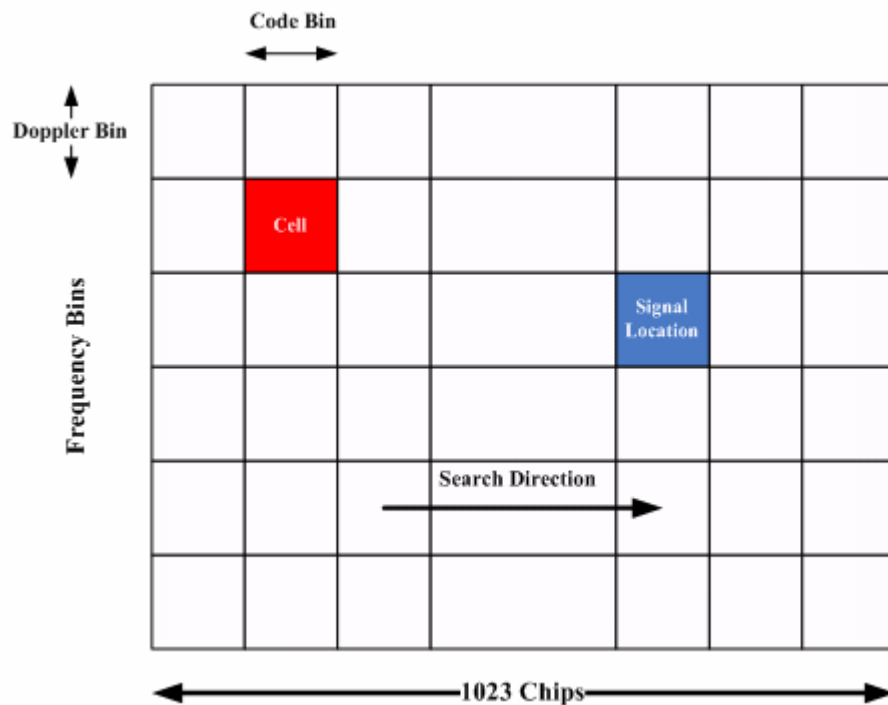


**Figure 2.3: Two-dimensional C/A code search (Modified from Kaplan, 1996)**

The search dwell times can vary from less than 1 ms (Doppler bins of about 667 Hz) for strong signals up to 10 ms (67-Hz Doppler bins) for weaker signals. The poorer the expected  $C/N_0$ , then the longer the integration time (and overall search time) must be used in order to have reasonable success of signal acquisition (O'Driscoll et al 2008, O'Driscoll 2007, Kaplan 1996). Signal obscuration (trees, buildings, snow or ice on the antenna, and so forth), RF interference, ionospheric scintillation, and antenna gain roll-off can all significantly reduce the  $C/N_0$  relative to that of an open sky environment.

It is important to recognize that the C/A code autocorrelation and cross-correlation sidelobes can cause false detections if these sidelobes are adequately strong compared with the main correlation peak. The increment of sidelobes is inversely proportional to the search dwell time. To overcome this problem, a combination of both increased dwell time (to minimize sidelobes) and a high detector threshold setting (to reject sidelobes) can be used for the initial search pass. On subsequent search passes, the dwell time and threshold can be decreased. The drawback of this scheme is the increased search time when the  $C/N_0$  is low. During the dwell time,  $T$ , in each cell, the in-phase component  $I$  and quadrature-phase component  $Q$  from the correlator after carrier and code wipe-off are used to compute the integrated correlation envelope  $\sqrt{I^2 + Q^2}$ . Each envelope is compared to a threshold to determine the presence or absence of signal. The detection of the signal is a statistical process because each cell either contains noise with the signal absent or noise with the signal present.

## 2.4 Tracking

Tracking loops play an important role in the operation of a receiver. Tracking loops not only refine the rough estimates of the carrier frequency, carrier phase and code phase obtained from acquisition, but also keep track of the carrier Doppler, phase and the code offset for each visible satellite due to the line of sight (LOS) motion between the satellite and receiver and the receiver's clock drift. They are also used to generate the pseudorange and carrier phase measurements for computing the user's position and Doppler measurements for the velocity. In terms of tracking schemes, the architectures of GPS

receivers can be divided into standard, estimator-based, vector-based and ultra-tight receivers. Each of these is introduced below.

#### ***2.4.1 Standard GPS receiver***

The standard GPS receiver architecture, also known as a scalar-tracking architecture, is shown in Figure 2.4. The digital IF samples are passed to each channel in parallel to a signal processing block where Doppler removal (baseband mixing) and correlation (de-spreading) are performed. The correlator outputs are then sent to discriminators and loop filters to determine the error between the local generated signals and incoming signals. Note that there usually are separate loops for code, frequency and phase tracking. More information on discriminators and loop filters is available in Ward et al (2006). The local signal generators are used for Doppler removal and correlation and are updated using the loop filter outputs. Finally, each channel's measurements are incorporated into the navigation filter to estimate position, velocity and time (Kaplan 1996, Van Dierendonck 1996).

The benefits of the standard receiver architecture are its relative simplicity and robustness. In the case of robustness, such a receiver architecture has independently operated channels and therefore one tracking channel cannot corrupt another one. However, on the downside, the fact that the signals are inherently related via the receiver's position and velocity is completely ignored. Furthermore, the possibility for one tracking channel to aid another channels is lost. For more information on scalar-tracking, refer to, for

example, Spilker (1996), Van Dierendonck (1996), Misra & Enge (2001) or Ward et al (2006).

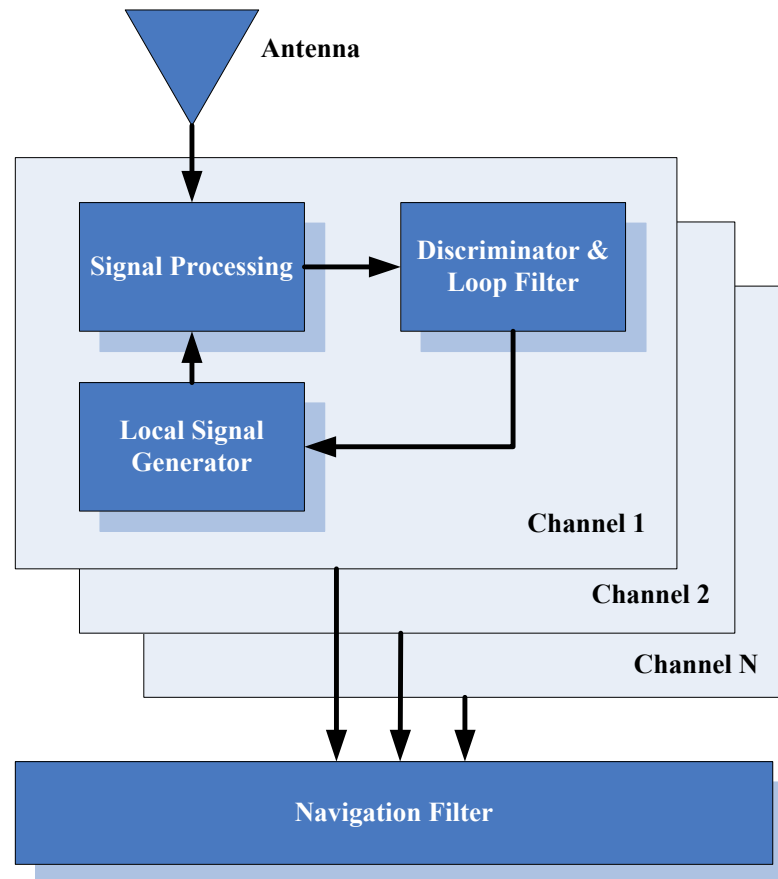


**Figure 2.4: Standard GPS receiver architecture**

#### ***2.4.2 Estimator-based GPS receiver***

In the estimator-based receiver architecture, the discriminator and loop filters for the carrier and code tracking loops of the standard receiver are replaced by a single Kalman Filter. Other similar estimators could also be used, although the Kalman Filter is well suited for this purpose. It is noted that some implementations only replace the carrier tracking loop with the Kalman Filter for specific purposes such as when the receiver is operating under high dynamics or scintillation environments (Psiaki et al 2007, Beach &

Kintner 2001). The overall receiver architecture is shown in Figure 2.5; the red elements highlight differences relative to the standard receiver.

The benefit of the Kalman filter for error estimation is that it allows for weighting of the measurements (correlator outputs, in this case) based on their estimated accuracies. In the implementation of this thesis, the weighting is based on the signal power. The measurement weighting scheme outperforms traditional loop filters, which assume that all measurements (from the discriminators) contain an equal amount of information in choosing the optimum loop bandwidth under certain conditions (Petovello et al 2007, 2008).

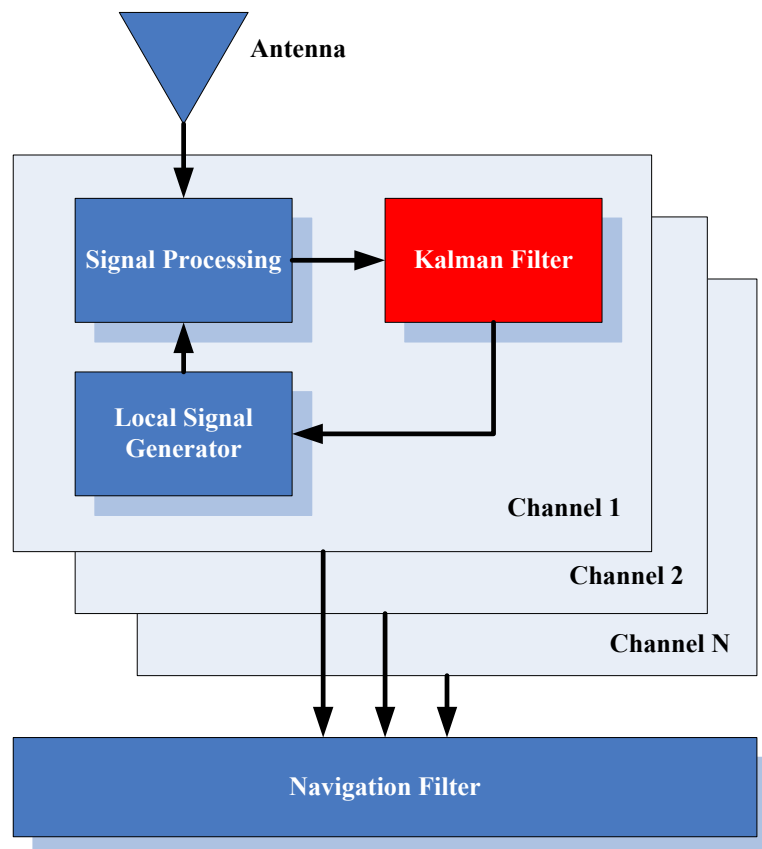


**Figure 2.5: Estimator-based GPS receiver architecture**

### ***2.4.3 Vector-based GPS receiver***

In contrast to the standard GPS receiver architecture (using either a standard or estimator-based approach), vector-tracking estimates the position and velocity of the receiver directly. The general vector tracking architecture is shown in Figure 2.6 in the orange elements highlight the differences between the estimator-based and vector-based receiver. In vector-based GPS receivers, the individual tracking loops are eliminated and are replaced by the navigation filter (for the estimator-based approach, this feedback is not present.) With the position and velocity of the receiver known, the feedback to the local signal generators is obtained from the computed range and range rate to each satellite. (Petovello et al 2006, 2007, 2008; Lashley 2006; Lashely & Bevly 2006). It is also noted that, for efficiency, many implementations of vector-based receivers employ a federated or cascaded approach (Abbott & Lillo 2003; Kim et al 2003; Jovancevic et al 2004; Ohlmeyer 2006; Petovello et al 2007, 2008). In this case, as illustrated in Figure 2.6, each channel still has an associated Kalman filter that estimates the tracking errors for that channel. Such implementations reduce the order of the navigation filter and decrease input rate into the navigation filter by using local filters. Also as shown in this figure, the feedback to the NCO is obtained from the Kalman filter and the navigation solution. The navigation filter only updates the code NCO and provides the Doppler information since the navigation accuracy is not sufficient for carrier phase tracking. The channel filter only updates the carrier phase, which is illustrated with a red line in Figure 2.6. The primary advantages of vector-tracking are that the shared position and velocity information can be used to aid the tracking of the signals with low  $C/N_0$  (Spilker 1996). From an estimation point of view, the central Kalman Filter generates optimum estimates

of signal parameters of each satellite (e.g., carrier Doppler, carrier phase and code phase) based on the correlation outputs from all channels; the noise is therefore reduced in all channels. Vector-tracking is also able to improve tracking in weak-signal or jamming environments, especially when integrated with inertial sensors (Gustafson et al 2000, Ohlmeyer 2006, Pany & Eissfeller 2006). The primary drawback is that tracking of all satellites is intimately related, and any error in one channel can potentially have a negative effect on other channels (Petovello et al 2007, 2008; Lashley 2006; Lashely & Bevely 2006).

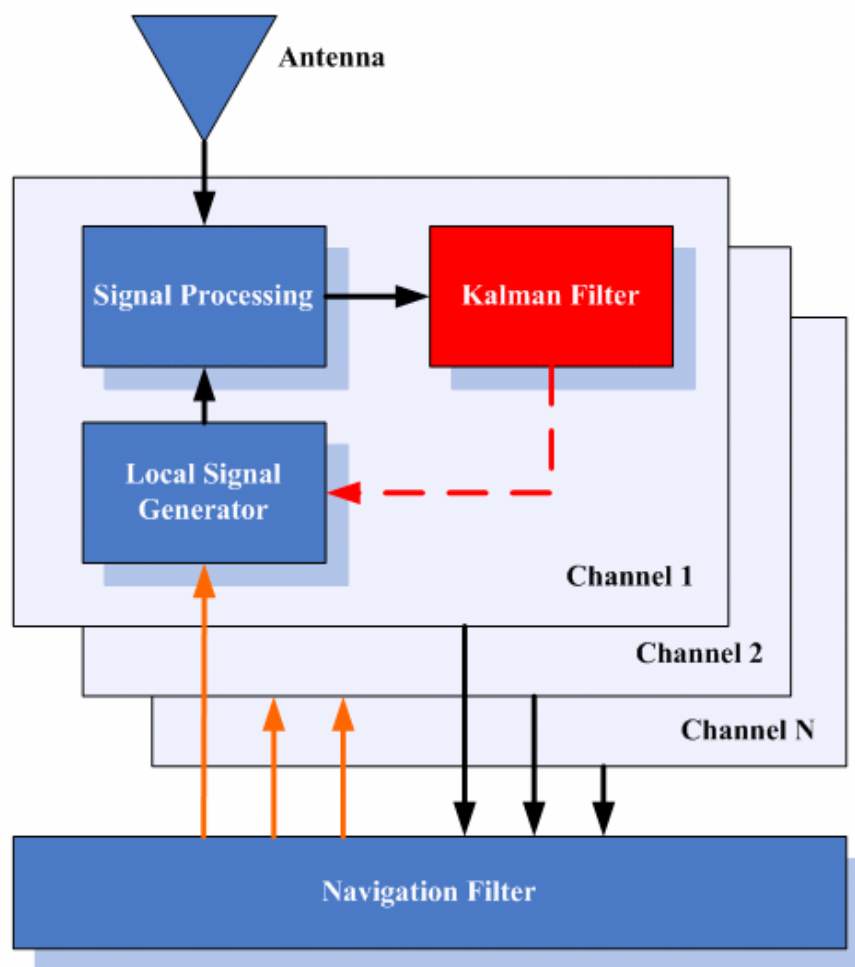


**Figure 2.6: Vector-based GPS receiver architecture**

#### 2.4.4 Ultra-tight GPS receiver

The ultra-tight GPS receiver architecture implemented in this thesis is based on the vector-based receiver as shown in Figure 2.7, where yellow blocks illustrate the differences from the vector-based approach. The main difference from the vector-tracking architecture is the inclusion of an IMU and a set of INS mechanization equations. Therefore the navigation filter is changed to include both the GPS and INS states (Petovello et al 2007, 2008; Ziedan 2006).

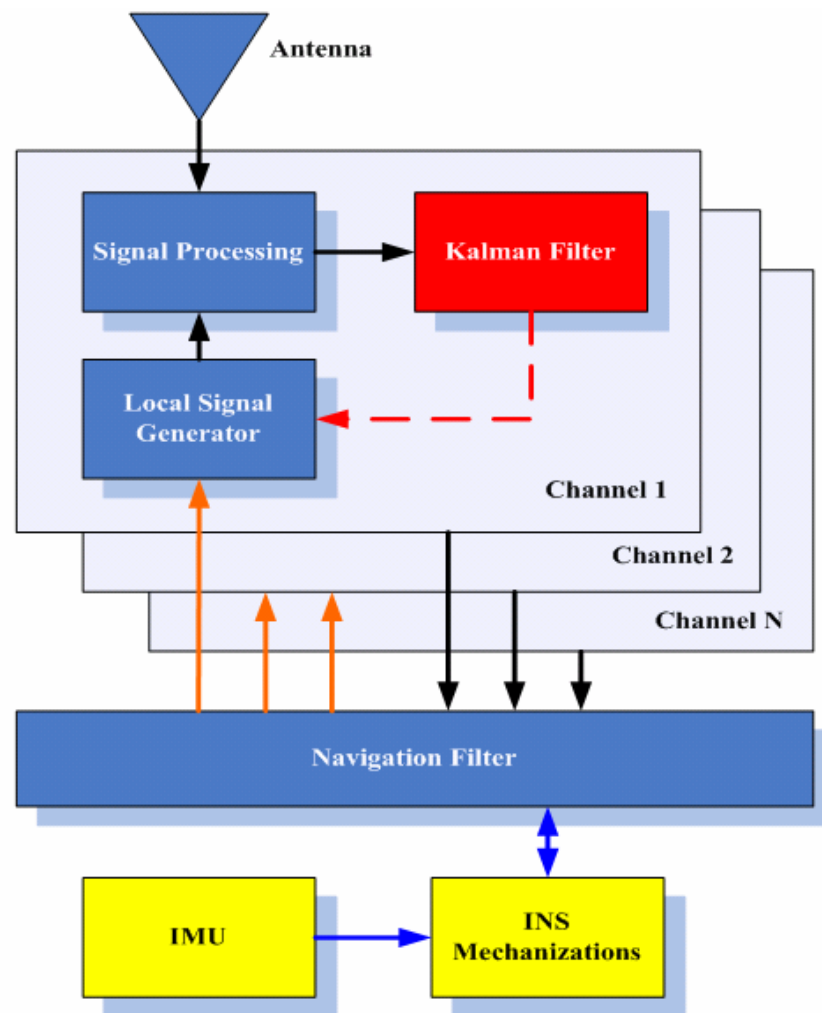


Figure 2.7: Ultra-Tight GPS receiver architecture

The drawbacks of the ultra-tight receiver are the same as those listed for the vector-based receiver. In terms of benefits however, the ultra-tight receiver has better performance compared to a vector-based receiver because the INS high measurement rate provides more precise information about the receiver dynamics between navigation filter updates whereas the vector receiver would have to predict the navigation solution forward using past estimates, thus introducing additional errors. This is particularly important when coherently integrating over longer time intervals where predicting the navigation solution may introduce additional attenuation (Petovello et al 2007, 2008).

It should be noted that the inertial sensors are only able to compensate for changes in the antenna-to-satellite geometry, including lever-arm effects between the IMU and GPS antenna and phase wind-up effects. In other words, it provides no benefit if the received signal varies because of “non-geometric” effects such as receiver clock errors, multipath or interference. Although this would seem to be a positive effect, care should be exercised since it has been observed that, in some instances, this can generate measurement biases in the carrier phase data (Petovello et al 2007, 2008).

### **CHAPTER THREE: ULTRA-TIGHTLY COUPLED GPS/INS INTEGRATION**

Having reviewed different GPS receiver architectures in the previous chapter, focus can now be directed to GPS and INS integration. To begin with, a general review of Inertial Navigation System (INS) is presented. Then, in Section 3.2 an overview of different GPS and INS integration strategies are provided. Section 3.3 gives explanations on ultra-tight integration in detail including the INS/GPS integration filter, the channel filter and the vector-based NCO updates, based on the work of Godha (2006), Petovello et al (2006, 2007, 2008) and Yang (2008).

#### **3.1 Overview of Inertial Navigation System**

An Inertial Navigation System (INS) is a navigation system that uses motion sensors (accelerometers) and rotation sensors (gyroscopes) to continuously calculate via dead reckoning the position, attitude, and velocity of a moving object without the need for external references. The INS is initially provided with its position and velocity from another source, and thereafter computes its updated position and velocity by integrating information received from the inertial sensors. The advantage of an INS is that it requires no external references in order to determine its position, orientation, or velocity once it has been initialized.

The inertial sensor or Inertial Measurement Unit (IMU) nominally consists of three accelerometers and three gyroscopes mounted on an orthogonal triad. Gyroscopes measure the angular velocity of the system in the inertial reference frame. By using the

original attitude of the system in the inertial reference frame as the initial condition and integrating the angular velocities, the system's current attitude can be computed at all times. Accelerometers measure the linear acceleration of the system in the inertial reference frame, but in directions that can only be measured relative to the object being positioned (since the accelerometers are fixed to the object and rotate with the object, but are not aware of their own orientation). Performing integration on the inertial accelerations using the correct kinematic equations yields the velocities of the system, and a second integration yields the position.

All inertial navigation systems suffer from biases and drifts: small errors in the measurement of acceleration and angular velocity are integrated into progressively larger errors in velocity, which translate into still greater errors in position. Since the new position is calculated from the previous calculated position, and the measured acceleration and angular velocity, these errors are cumulative and increase with time since the initial position was input. Therefore the INS must be periodically corrected by information from other navigation systems or sensors such as GPS, wheel speed sensors, etc.

### ***3.1.1 Coordinate frames and transformations***

Before discussing the INS mechanizations in detail, the following frames and the transformations that are used in this thesis should be defined.

**Inertial Frame (i-frame)**

Inertial frame is the frame in which Newton's first law of motion is valid. Since the ideal definition of inertial frame is not practical, a quasi-inertial frame which is non-rotating and non-accelerating is often used (Petovello 2003, Jekeli 2001). The inertial frame is defined as follows:

Origin : Earth's centre of mass

Z-Axis : Parallel to the spin axis of the Earth

X-Axis : Pointing towards the mean vernal equinox

Y-Axis : Orthogonal to X and Z completing a right-handed system

**Earth Centred Earth Fixed Frame (ECEF or e-frame)**

The Earth-fixed frame shown in Figure 3.1 is defined as follows:

Origin : Earth's centre of mass

Z-Axis : Parallel to the Earth's mean spin axis

X-Axis : Pointing towards the mean meridian of Greenwich

Y-Axis : Orthogonal to the X and Z axes to complete a right-handed frame

**Local Level Frame (LLF or l-frame)**

The Local level frame is a local geodetic frame (Figure 3.1) and is defined as follows:

Origin : Coinciding with sensor frame

Z-Axis : Orthogonal to reference ellipsoid pointing Up

X-Axis : Pointing towards geodetic East

Y-Axis : Pointing toward geodetic North

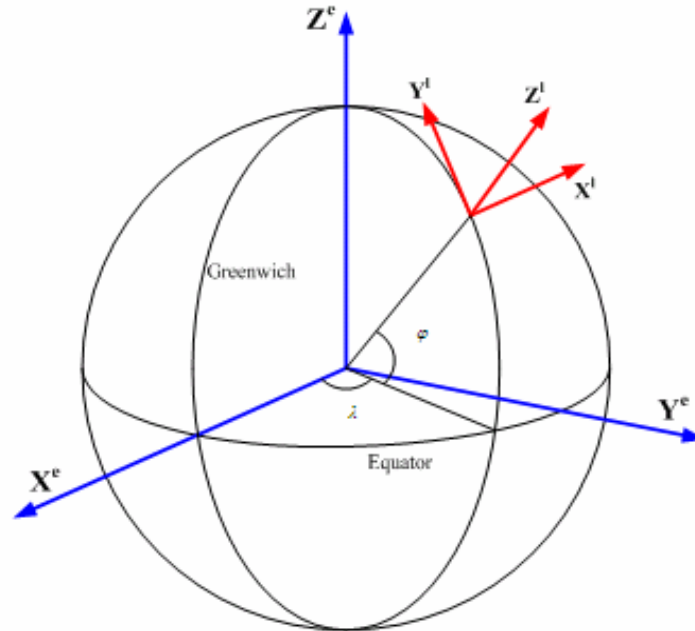


**Figure 3.1: Local level frame and ECEF frame**

### **Body Frame (b-frame)**

The body frame represents the orientation of the IMU axes. For strapdown inertial systems, as used here, the IMU is rigidly mounted to the platform. The body frame shown in Figure 3.2 is defined as follows:

Origin : Centre of IMU

X-Axis : Pointing towards the right of the platform

Y-Axis : Pointing towards the front of the platform

Z-Axis : Orthogonal to the X and Y axes to complete a right-handed frame

### **Vehicle Frame (v-frame)**

The vehicle frame (v-frame) is an orthogonal axis set that is aligned with the roll, pitch and heading axes of a vehicle. This frame is used because sometimes the IMU's body frame is not parallel to the v-frame. The frame shown in Figure 3.2 is defined as follows:

Origin : Mass centre of the vehicle

X-Axis : Pointing towards the right of the vehicle

Y-Axis : Pointing towards the front of the vehicle

Z-Axis : Orthogonal to the X and Y axes to complete a right-handed system

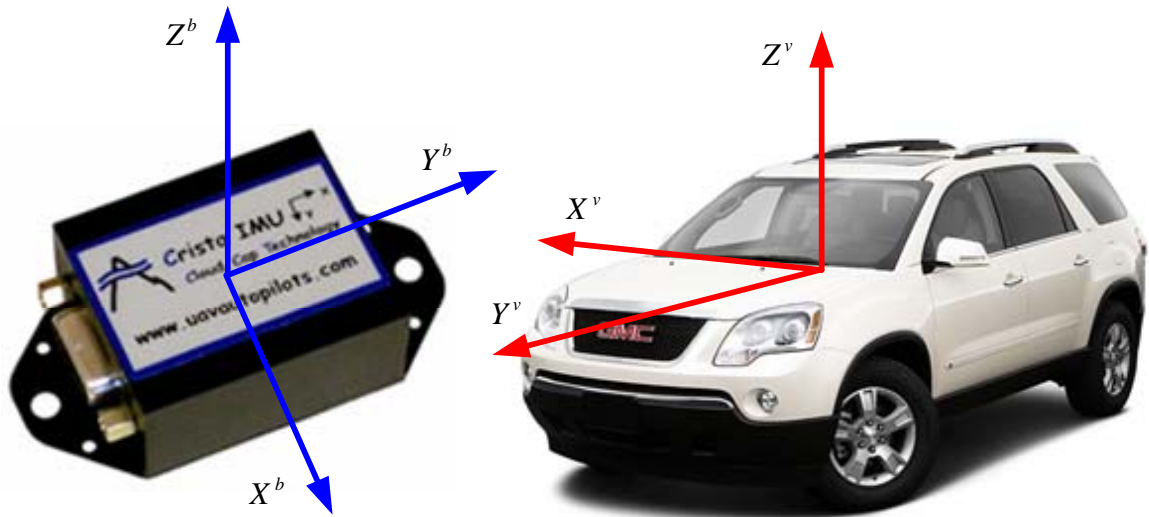


**Figure 3.2: Body frame and vehicle frame**

The transformation between e-frame and l-frame can be performed by two consecutive rotations around the X and Z axes of the ECEF frame, and is given by (Godha 2006)

$$R_e^l = R_1\left(\frac{\pi}{2} - \varphi\right)R_3\left(\frac{\pi}{2} + \lambda\right) \quad 3.1$$

where

$\varphi$  is the latitude;

$\lambda$  is the longitude;

$R_e^l$  is the rotation matrix from e-frame to l-frame;

$R_1$ ,  $R_3$  are the rotation matrixes about x and y axis respectively.

The transformation between b-frame and l-frame can be performed by three consecutive rotations around Y, X and Z axes, and is given by (Godha 2006)

$$R_b^l = R_3(\psi)R_1(-\theta)R_2(-\phi) \quad 3.2$$

where

$\psi$  is the azimuth angle;

$\theta$  is the pitch angle;

$\phi$  is the roll angle;

$R_b^l$  is the rotation matrix from the b-frame to the l-frame.

It is noted that, usually the body frame is aligned with the vehicle frame or it can be rotated to the vehicle frame. Thus the azimuth, pitch and roll angles at this time represent for the orientation of the vehicle.

The transformation between the b-frame and e-frame can be obtained by the consecutive rotation by

$$R_b^e = R_l^e R_b^l = (R_e^l)^T R_b^l \quad 3.3$$

### 3.1.2 Mechanization equations

Mechanization equations are the equations used to compute the useful position velocity and attitude information from the measurements of an IMU. Typically, the IMU measurements are the specific force and angular velocity. The INS mechanization equations can be developed in both e-frame and l-frame. In this thesis, the mechanization is implemented in the l-frame convenience.

There are mainly two steps to compute the navigation solution from the IMU's measurements. Given the initial attitude information obtained by the alignment (alignment will be introduced in the next section), the angular velocity is integrated to update the IMU's attitude. It is noted that the earth rotation and the changing l-frame should be compensated to compute the true angular velocity of the IMU. In the second step, the new attitude information is used to transform the accelerations sensed from the IMU into the navigation frame of interest. The sensed accelerations should be compensated for gravity to determine the true IMU accelerations. Then, the accelerations can be integrated to obtain the velocity; after the second integration, position can be calculated.

The above stated procedure in mathematical terms is given by (Jekeli 2001, Yang 2008):

$$\begin{bmatrix} \dot{\mathbf{r}} \\ \dot{\mathbf{v}} \\ \dot{\mathbf{R}}_b^l \end{bmatrix} = \begin{bmatrix} \mathbf{D}^{-1} \mathbf{v}^l \\ \mathbf{R}_b^l \mathbf{f}^b - (2\boldsymbol{\Omega}_{ie}^l + \boldsymbol{\Omega}_{el}^l) + \mathbf{g}^l \\ \mathbf{R}_b^l (\boldsymbol{\Omega}_{ib}^b + \boldsymbol{\Omega}_{il}^b) \end{bmatrix} \quad 3.4$$

In above equations

$$\mathbf{D}^{-1} = \begin{bmatrix} 0 & \frac{1}{M+h} & 0 \\ \frac{1}{(N+h)\cos\varphi} & 0 & 0 \\ 0 & 0 & 1 \end{bmatrix},$$

”over-dots” denote time derivatives, the superscript ‘l’ and ‘b’ represents the values in the l-frame and b-frame, where

$M$  is the meridian radius of the earth curvature;

$N$  is the prime vertical radius of the earth curvature;

$\mathbf{r}^l$  is the position vector,  $\mathbf{r}^l = [\varphi \quad \lambda \quad h]^T$ ;

$\mathbf{v}^l$  is the velocity vector in the l-frame. Given the definition of the l-frame, the velocity vector can be expressed by three components in the east, north and up direction, respectively.  $\mathbf{v}^l = [v^E \quad v^N \quad v^U]^T$ ;

$\mathbf{f}^b$  is the specific force vector from the IMU accelerometer triad. The vector represents for the specific force in the b-frame;

$\mathbf{g}^l$  is the earth’s local gravity vector.  $\mathbf{g}^l = [0 \quad 0 \quad -g]$ , where  $g$  is computed from a normal gravity model (Jekeli 2001);

$\mathbf{\Omega}_{bc}^a$  is a skew-symmetric matrix, which indicates the rotation rate of frame ‘c’, relative to frame ‘b’, expressed in frame ‘a’. If  $\boldsymbol{\omega} = [\omega_x \quad \omega_y \quad \omega_z]$ , then the corresponding skew-symmetric matrix is:

$$\mathbf{\Omega} = \begin{bmatrix} 0 & -\omega_z & \omega_y \\ \omega_z & 0 & -\omega_x \\ -\omega_y & \omega_x & 0 \end{bmatrix};$$

$\boldsymbol{\omega}_{ie}^l$  is the earth rotation rate projected into the l-frame, which is given by:

$$\boldsymbol{\omega}_{ie}^l = [0 \quad \omega_e \cos \varphi \quad \omega_e \sin \varphi];$$

$\boldsymbol{\omega}_{el}^l$  is the transport rate, which refers to the change of orientation of the l-frame with respect to the Earth due to motion of the object being positioned. Its expression is

$$\boldsymbol{\omega}_{el}^l = [-v^N / (M + h) \quad v^E / (N + h) \quad v^E \tan \varphi / (N + h)]$$

$\boldsymbol{\omega}_{ib}^b$  is the angular rate vector which is sensed by the gyroscope triad. It represents the rotation rate of b-frame relative to i-frame, expressed in the b-frame;

$\boldsymbol{\omega}_{il}^b$  is the sum of the  $\boldsymbol{\omega}_{ie}^b$  and  $\boldsymbol{\omega}_{el}^b$ . Thus,

$$\boldsymbol{\omega}_{il}^b = (\mathbf{R}_b^l)^T \boldsymbol{\omega}_{ie}^l + (\mathbf{R}_b^l)^T \boldsymbol{\omega}_{el}^l = (\mathbf{R}_b^l)^T \begin{bmatrix} -\frac{v^N}{M + h} \\ \frac{v^E}{N + h} + \omega_e \cos \varphi \\ \frac{v^E}{N + h} \tan \varphi + \omega_e \sin \varphi \end{bmatrix}$$

Equation (3.4) is presented in the continuous-time domain. Since the IMU operates in the discrete form, the discrete integration method is usually used to transform the measurements into the final position, velocity and attitude (Shin 2005, 2001; Savage 2000). It is noted that, instead of the measured accelerations and angular velocity, most IMUs will actually output velocity  $\Delta \tilde{v}_f^b$  and angular increments  $\Delta \tilde{\theta}_{ib}^b$  over the sample period. The symbol  $\tilde{\phantom{x}}$  denotes values corrupted by sensor errors. Therefore, the digitized implementation of the INS mechanizations consists of the following steps, each of which

is discussed in more detail below: sensor error compensation, attitude update, and finally velocity and position update.

### Sensor error compensation

The raw IMU outputs are often corrupted by sensor errors which typically include biases, scale factor errors and axis non-orthogonalities. These values can be calibrated in the laboratory or can be estimated during the navigation process. Once the sensor errors are obtained, the measurements can be corrected using the following equations for gyros and accelerometers, respectively:

$$\Delta\theta_{ib}^b = \frac{\Delta\tilde{\theta}_{ib}^b + b_g \Delta t}{1 + S_g} \quad 3.5$$

$$\Delta v_f^b = \frac{\Delta\tilde{v}_f^b + b_a \Delta t}{1 + S_a} \quad 3.6$$

where

$b_g$  is the gyro drift;

$b_a$  is the accelerometer bias;

$S_g$  is the scale factor of the gyro;

$S_a$  is the scale factor of the accelerometer;

$\Delta t$  is the sample period. And the sampling frequency is often denoted by  $f = 1/\Delta t$  Hz.

### Attitude update

The body angular increment with respect to the navigation frame are obtained by

$$\Delta \theta_{lb}^b = \Delta \theta_{ib}^b - R_l^b \omega_e \Delta t = [\Delta \theta_x \quad \Delta \theta_y \quad \Delta \theta_z]^T \quad 3.7$$

The updated rotation matrix can then be obtained to a first order approximation as

$$R_b^l(t_{k+1}) = R_b^l(t_k)(I + S^b) \quad 3.8$$

where  $t_{k+1} - t_k = \Delta t$ ,  $S^b$  is the skew-symmetric form of the angular increment vector in Equation (3.7). Also, the transformation matrix is often parameterized in terms of quaternions because of their robustness against singularities and their computational efficiency. Readers can refer to Savage (2000) and Jekeli (2001) for details about the quaternion update method. The attitude parameters can then be obtained using the following equations:

$$\phi = -\tan^{-1}\left(\frac{(R_b^l)_{3,1}}{(R_b^l)_{3,3}}\right) \quad 3.9$$

$$\theta = -\sin^{-1}\left((R_b^l)_{3,2}\right) \quad 3.10$$

$$\psi = \tan^{-1}\left(\frac{(R_b^l)_{1,2}}{(R_b^l)_{2,2}}\right) \quad 3.11$$

where  $(R_b^l)_{i,j}$  is the element at the i-th row and j-th column of the  $R_b^l$  matrix.

### Position and velocity update

The body frame velocity increment due to the specific force is transformed to the navigation frame through the following equation:

$$\Delta v_f^l = R_b^l(t_k) \left( I + \frac{1}{2} S^b \right) \Delta v^b \quad 3.12$$

Then, the velocity increment is obtained by applying the Coriolis and gravity correction (Savage 2000):

$$\Delta v^l = \Delta v_f^l - (2\omega_{ie}^l + \omega_{el}^l) \times v^l \Delta t + g^l \Delta t \quad 3.13$$

Once the velocity increment is computed, the updated velocity is given by

$$v_{k+1}^l = \Delta v^l + v_k^l \quad 3.14$$

The positions are integrated using the second order Runge-Kutta method (Jekeli 2001):

$$r_{k+1}^l = r_k^l + \frac{1}{2} D^{-1} (v_{k+1}^l + v_k^l) \quad 3.15$$

Figure 3.3 summarizes the overall l-frame INS mechanizations described in this section.

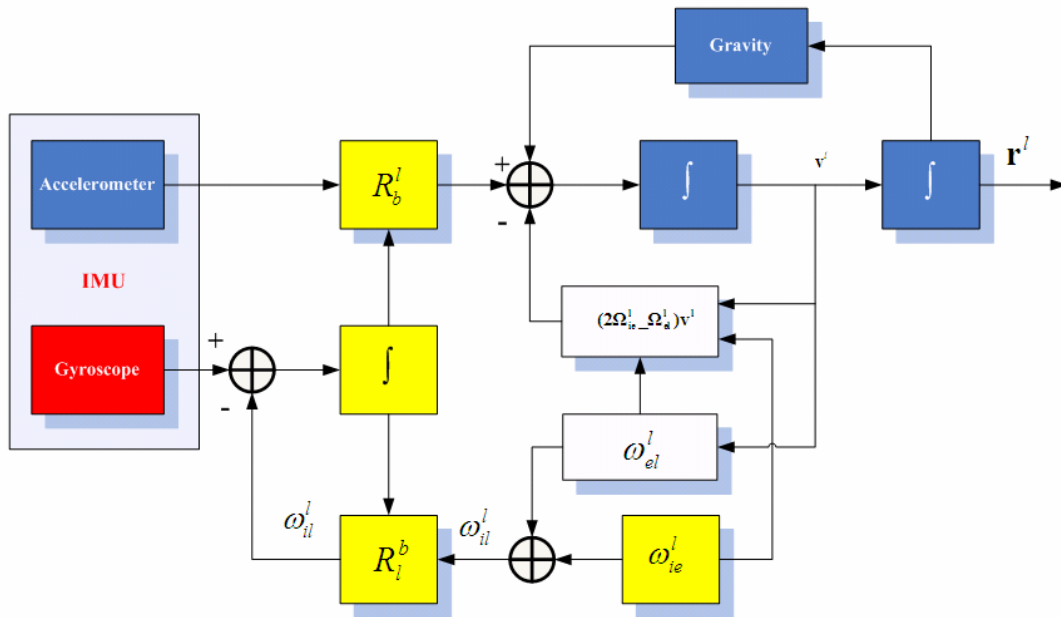


**Figure 3.3: Local level frame (l-frame) INS mechanizations**

### **3.2 Overview of INS/GPS Integration Strategies**

Integration of INS/GPS provides an enhanced navigation system that has superior performance in comparison with either stand-alone system. The integrated system has the features of both long-term and short-term accuracy, improved availability and better integrity (Jekeli 2001, Shin 2001). Typically, there are three strategies for the integration of GPS and INS, which are normally classified as loosely coupled, tightly coupled and ultra-tightly coupled. The ultra-tightly coupled integration has been introduced in Chapter 2, therefore, it is not included in this section. The implementation details of the ultra-tight integration will be described in Section 3.3.

#### ***3.2.1 Loosely coupled integration***

In this integration scheme, GPS and INS processing is carried out in two separate but interacting filters (Godha 2006). GPS measurements are processed independently in a GPS-only Kalman filter. Then the output of this filter is used to periodically update the integration filter. The integration filter uses the difference between the GPS-derived position and velocity estimates and the INS mechanization-derived position and velocities as measurements to compute the updated navigation solution. The block diagram of this integration strategy is shown in Figure 3.4. The term “closed loop” means that the compensation of sensor errors is within the calculation procedure of the INS mechanizations, using estimated errors from the integrated Kalman filter.

The benefits of the loose integration are the relative ease of implementation and robustness (Petovello 2003, Godha 2006). The robustness arises because the GPS and

INS operate independently. However, on the downside, the fact that the GPS measurements during the partial GPS outages can still update the integration filter is completely ignored because no position and velocity information is fed into the integrated filter from the GPS filter when the satellite observations are less than four. From the estimation point of view, Petovello (2003) identifies one specific problem with this implementation. Because the system has two independent filters, the processing noise has to be added to both of the filters. The extra processing noise in the GPS filter used to compensate the user's dynamics would have negative effect on the state estimation.

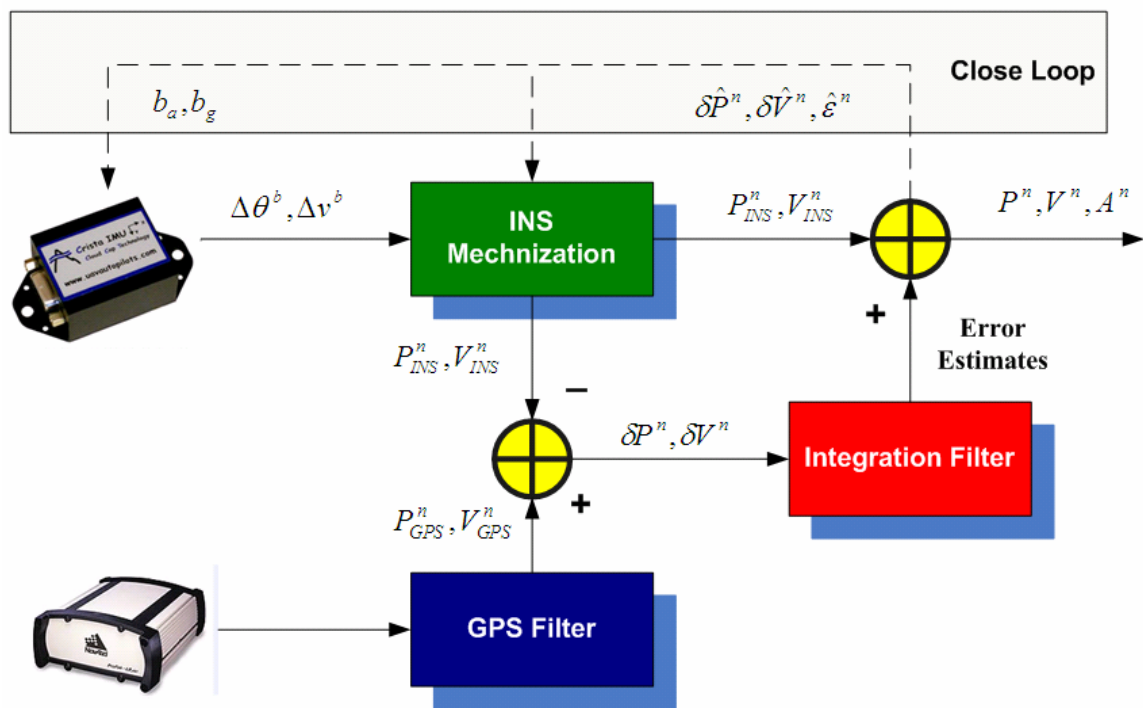


Figure 3.4: Block diagram of loosely coupled integration

### 3.2.2 Tightly coupled integration

In this integration scheme, a single/centralized integration filter is used to fuse the GPS and INS information. Therefore this integration strategy is also called “centralized integration scheme”. The integration strategy is shown graphically in Figure 3.5.

The integration filter uses the differences between the GPS generated pseudorange measurements and the INS predicted pseudorange and Doppler measurements to obtain the error estimates. These error estimates are then used to correct the INS derived position, velocity and attitude information. Similarly, a close loop correction method can be used to compensate for the sensor errors during the INS mechanization computations. Details about the system error model used in the tight integration are presented in Section 3.3.

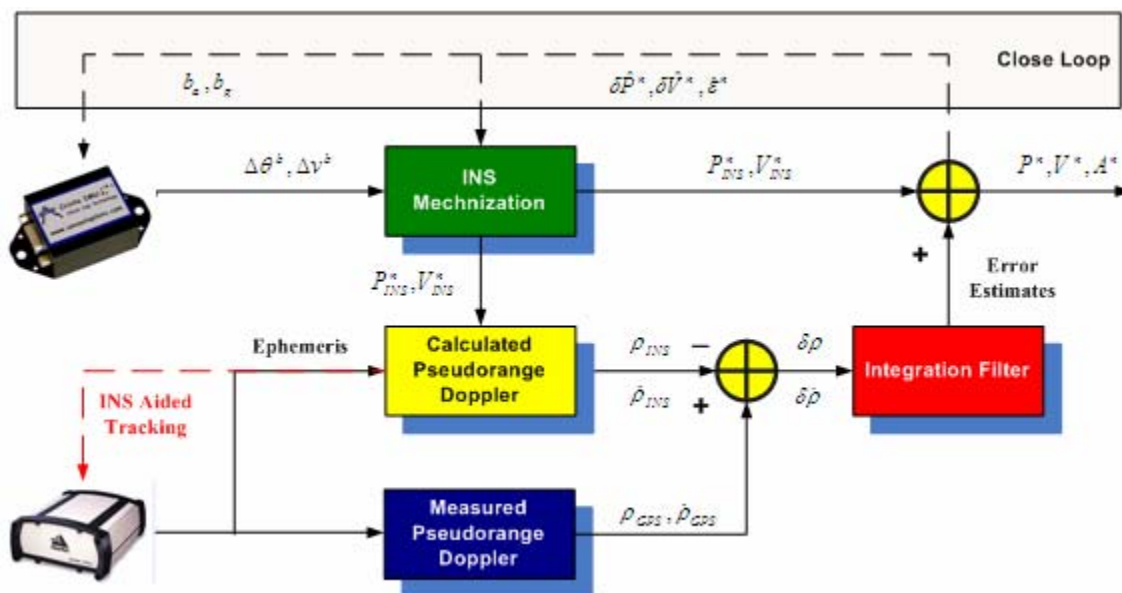


Figure 3.5: Block diagram of tightly coupled integration

The primary advantages of tight integration are (i) better state estimates because no additional processing noise is present in the single filter and the GPS measurements used to update the filter are more statistically independent compared with the position and velocity, (ii) improved GPS fault detection and exclusion (Petovello 2003) can be obtained, (iii) the carrier phase measurements also benefit from tight integration because integer ambiguities can be recovered and verified quickly. The major drawback of the tightly coupled approach compared with the loosely coupled approach is the increased size of the state vector, which leads to an increased computational burden (Petovello 2003, Gao 2007).

In some references, the INS derived Doppler is used to aid the carrier and code tracking loop as shown in Figure 3.5 with the red line. It can improve the performance in high dynamic situations (Gebre-Egziabher et al 2007, Alban et al 2003, Gao 2007). This method can be classified as tight integration with Doppler aided tracking.

### **3.3 Ultra-tight GPS/INS Integration**

As discussed in Chapter 2, the ultra-tight GPS receiver used in this thesis includes two filters: the GPS/INS integration filter and the channel filter. Because of the nonlinear properties of the INS and GPS signal tracking loops, an Extend Kalman Filter (EKF) is used in both cases. The GPS/INS integration filter of the ultra-tight approach is similar to that of the tight-integration except that the INS derived code phase and Doppler information is fed into the code and carrier NCOs.

The ultra-tight GPS receiver implemented in this thesis is operated in the standard GPS receiver mode before a stable navigation solution is obtained. Then the receiver is transformed to the ultra-tight mode. During the transition process, the current position and velocity generated from the navigation solution is sent to the INS as initial conditions. At the same time, the initial attitude information can be obtained by the alignment procedure. It is noted that, for land vehicle navigation, a two or three minute static alignment is sufficient to obtain the initial attitude without losing too much accuracy if a higher grade IMU is used such as HG1700 (Godha 2006). However, for MEMS-grade IMUs such as the Crista or vehicle sensors, a static alignment is no longer feasible because gyro biases (turn-on bias and drifts) and noise typically exceeds the earth rotation rate (Farrell & Barth 2001). In this case, the initial attitude can be obtained by either in-motion alignment or additional sensors such as magnetometers, electronic compass, etc (Godha 2006, Shin 2005, Shin & El-Sheimy 2008). After the INS is initialized, the GPS measurements (pseudorange and Doppler) and IMU measurements can be integrated to generate the navigation solution. Once the ultra-tight integration is established, the vector-DLL is used instead of the conventional DLL. The code NCO at this time is controlled by the code phase from the integrated GPS/INS filter. Also, the Doppler calculated by the integration filter is fed into the carrier tracking loop. It is noted that when operated in the ultra-tight mode the local NCO is also updated between the navigation filter updates using the INS derived code phase and Doppler information. Therefore the update rate for code and Doppler is similar to the IMU output rate. Besides, the channel filter always updates the phase loops and the update rate depends on the integration time used in the receiver. The typical update rate before the bit synchronization is accomplished is 1 ms and, after that,

is 20 ms. The implementation details are presented in the following sections. Section 3.3.1 introduces the theory of the EKF used for the navigation filter and the channel filter. Then the system measurement models of the navigation filter are described in Section 3.3.2, 3.3.3 and 3.3.4. The channel filters are discussed in 3.3.5. Finally the vector-based local NCO updates are discussed.

### ***3.3.1 Extended Kalman filter (EKF)***

The Kalman filter is a linear optimal estimator which addresses the problem of estimating the states of a dynamic system perturbed by Gaussian white noise. It is based on a recursive algorithm that uses a series of prediction and measurement update steps to obtain an optimal estimate of the state vector that has a minimum variance. Details about the Kalman filter can be found in Gelb (1974), Brown & Hwang (1992), and Grewal & Andrews (2001). The basic Kalman filter is limited to a linear assumption. However, most non-trivial systems are non-linear such as INS and GPS. The non-linearity can be associated either with the system model or with the measurement model or with both. In this case, Kalman filter theory can be extended to such non-linear systems by linearization around the a priori state estimates. If a Kalman filter uses the predicted states from the last epoch as the linearization point, it is called an Extended Kalman Kilter (EKF). Although the linearization procedure makes the EKF a suboptimal estimator (Brown & Hwang 1992), as long as the linearization effect is negligible, the EKF can result in nearly optimum solution for the non-linear state estimates.

A non-linear system can be described as

$$\dot{x}(t) = f(x(t), t) + G(t)w(t) \quad 3.16$$

where  $f(x(t), t)$  is a non-linear function representing the temporal behaviour of the system states. For linearization, a nominal trajectory  $x(t)$  is selected such that

$$x(t) = x^*(t) + \delta x(t) \quad 3.17$$

where  $\delta x(t)$  is a perturbation from the nominal trajectory. It is noted that “trajectory” in this context represents the time-series of any type of parameter, and is not restricted to the trajectory of a vehicle. After the first-order Taylor series expansion of Equation (3.16) about the nominal trajectory, a linearized continuous-time dynamic system is given by

$$\delta \dot{\mathbf{x}}(t) = \mathbf{F}(t)\delta \mathbf{x}(t) + \mathbf{G}(t)\mathbf{w}(t) \quad 3.18$$

where

$\mathbf{F}(t)$  is the system dynamics matrix;

$\delta \mathbf{x}(t)$  is the error state vector;

$\mathbf{G}(t)$  is the shaping matrix;

$\mathbf{w}(t)$  is a noise vector, assumed to be zero-mean white noise with a Gaussian distribution. Its covariance matrix is  $\mathbf{E}[\mathbf{w}(t)\mathbf{w}(t)] = \mathbf{Q}(t)\delta(t)$ , where  $\mathbf{Q}(t)$  is the spectral density matrix of  $\mathbf{w}(t)$  and the operator  $\delta(t)$  denotes the Dirac delta function.

After linearization about the nominal trajectory, the Kalman filter actually estimates the perturbations. The standard linear Kalman filter can be applied if the nominal trajectory is

known. A practical procedure is to use the last Kalman filter estimates as the linearization point. This method is used in the implementation of EKF.

Because both of the INS and GPS receiver are usually implemented with high-rate sampled data, the continuous-time system equations are to be transformed to their corresponding discrete-time form (Brown & Hwang 1992):

$$\delta \mathbf{x}_k = \Phi(t_k, t_{k-1}) \delta \mathbf{x}(t_{k-1}) + \int_{t_{k-1}}^{t_k} \Phi(t_k, \tau) \mathbf{G}(\tau) \mathbf{w}(\tau) d\tau \quad 3.19$$

or in abbreviated notation:

$$\delta \mathbf{x}_k = \Phi_{k,k-1} \delta \mathbf{x}_{k-1} + \mathbf{G}_{k-1} \mathbf{w}_{k-1} \quad 3.20$$

where  $\Phi_{k,k-1}$  is the state transition matrix,  $\delta \mathbf{x}_k$  is the system state (error) vector at  $t_k$ ,  $\mathbf{w}_{k-1}$  is the driving noise during  $\Delta t_k = t_k - t_{k-1}$  (Brown & Hwang 1992).

If  $\Delta t_k$  is very small or  $\mathbf{F}(t)$  is approximately constant over  $\Delta t_k$ , the following numerical approximation can be applied to calculate the transition matrix:

$$\Phi_{k,k-1} = e^{\mathbf{F}(t_{k-1})\Delta t_k} \approx \mathbf{I} + \mathbf{F}(t_{k-1})\Delta t_k + \frac{1}{2!} \mathbf{F}^2(t_{k-1})\Delta t_k^2 + \dots \quad 3.21$$

Because a white sequence is a sequence of zero-mean random variables that are uncorrelated in time, the covariance matrix associated with  $\mathbf{w}_k$  is given by (Brown & Hwang 1992)

$$E\{\mathbf{w}_k\} = 0$$

$$E\{\mathbf{w}_k \mathbf{w}_i^T\} = \begin{cases} \mathbf{Q}_k & i = k \\ \mathbf{0} & i \neq k \end{cases} \quad 3.22$$

$\mathbf{Q}_k$  can be expressed as

$$\begin{aligned} \mathbf{Q}_k &= E\{\mathbf{w}_k \mathbf{w}_k^T\} \\ &= E\left\{ \left[ \int_{t_k}^{t_{k+1}} \Phi(t_{k+1}, \xi) \mathbf{G}(\xi) d\xi \right] \left[ \int_{t_k}^{t_{k+1}} \Phi(t_{k+1}, \eta) \mathbf{G}(\eta) d\eta \right]^T \right\} \\ &= \int_{t_k}^{t_{k+1}} \int_{t_k}^{t_{k+1}} \Phi(t_{k+1}, \xi) \mathbf{G}(\xi) E\{\mathbf{w}(\xi) \mathbf{w}(\eta) \mathbf{G}^T(\eta) \Phi^T(t_{k+1}, \xi)\} d\xi d\eta \end{aligned} \quad 3.23$$

A trapezoidal integration of the above equation yields (Shin 2005)

$$\mathbf{Q}_k \approx \frac{1}{2} \left[ \Phi_{k+1,k} \mathbf{G}(t_k) \mathbf{Q}(t_k) \mathbf{G}(t_k)^T \Phi_{k+1,k}^T + \mathbf{G}(t_{k+1}) \mathbf{Q}(t_{k+1}) \mathbf{G}(t_{k+1})^T \right] \Delta t_{k+1} \quad 3.24$$

If  $\mathbf{G}(t) \mathbf{Q}(t) \mathbf{G}(t)^T$  can be treated as a constant for the time interval  $\Delta t_k = t_k - t_{k-1}$ , an approximate solution can be obtained by substituting Equation (3.21) into the above equation as

$$\mathbf{Q}_k \approx \frac{1}{2} \left[ \Phi_{k+1,k} \mathbf{G}(t_k) \mathbf{Q}(t_k) \mathbf{G}(t_k)^T + \mathbf{G}(t_k) \mathbf{Q}(t_k) \mathbf{G}(t_k)^T \Phi_{k+1,k}^T \right] \Delta t_{k+1} \quad 3.25$$

Similarly, the linearized measurement equation about the nominal trajectory is described by the following discrete-time equation:

$$\delta \mathbf{Z}_k = \mathbf{H}_k \delta \mathbf{x}_k + \mathbf{v}_k \quad 3.26$$

where

$\delta \mathbf{Z}_k$  is the measurement error vector;

$\mathbf{H}_k$  is the design matrix, which is defined by  $\mathbf{H}_k = \left. \frac{\partial \mathbf{h}[\mathbf{x}]}{\partial \mathbf{x}} \right|_{\mathbf{x}=\hat{\mathbf{x}}_{k,k-1}}$ ,  $\mathbf{h}[\mathbf{x}]$  is the nonlinear vector measurement function of the error states.

$\mathbf{v}_k$  is the measurement noise.

The measurement covariance matrix is written as

$$E\{\mathbf{v}_k\} = 0$$

$$E\{\mathbf{v}_k \mathbf{v}_i^T\} = \begin{cases} \mathbf{R}_k & i = k \\ \mathbf{0} & i \neq k \end{cases} \quad 3.27$$

The system and measurement noise ( $\mathbf{w}_k$  and  $\mathbf{v}_k$ ) are assumed to be uncorrelated, in which case  $E\{\mathbf{w}_k \mathbf{v}_j^T\} = 0$  for all  $i, k$ . The covariance matrix of the error state vector is defined as:  $E\{(\delta \tilde{\mathbf{x}}_k - \delta \mathbf{x}_k)(\delta \tilde{\mathbf{x}}_k - \delta \mathbf{x}_k)^T\} = \mathbf{P}_k$ .

With the above equations, the EKF can be realized by the prediction and update steps which are clearly indicated in Figure 3.6. The computation procedure can be summarized as follows (Brown & Hwang 1992, Grewal & Andrews 2001):

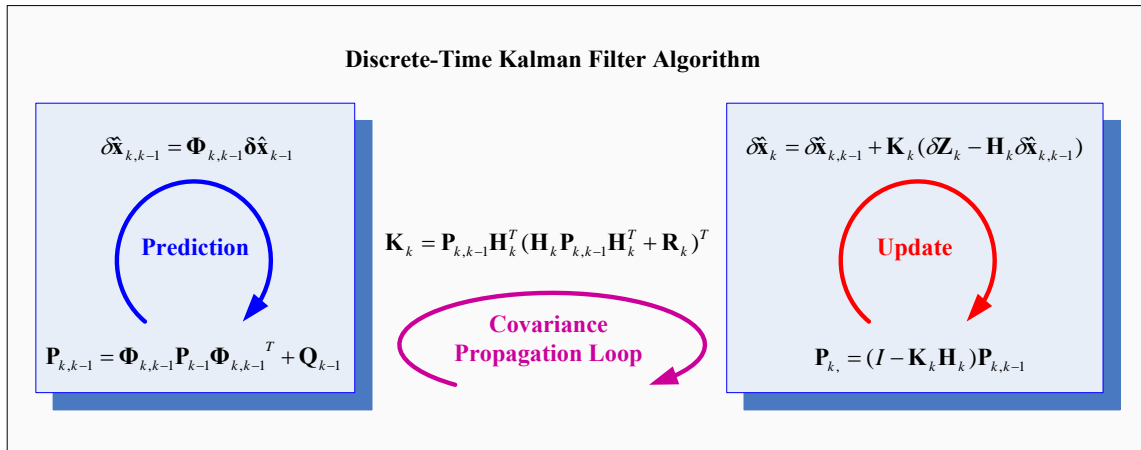


**Figure 3.6: EKF computation procedure**

### Prediction

The *a priori* state estimates  $\tilde{\delta\mathbf{x}}_{k,k-1}$  at time  $t_k$  are first computed using  $\Phi_{k,k-1}$ , and  $\delta\hat{\mathbf{x}}_{k-1}$  as

$$\tilde{\delta\mathbf{x}}_{k,k-1} = \Phi_{k,k-1} \delta\hat{\mathbf{x}}_{k-1}. \quad 3.28$$

The *a priori* covariance matrix  $\mathbf{P}_{k,k-1}$  at time  $t_k$ , which is the error covariance matrix before the measurement updates, is then computed using  $\mathbf{P}_{k-1}$ ,  $\Phi_{k,k-1}$ , and  $\mathbf{Q}_{k-1}$ .  $\mathbf{P}_{k-1}$  is the *posteriori* matrix at time  $t_{k-1}$  and the error covariance matrix after the measurement update at  $t_{k-1}$  is given as follows:

$$\mathbf{P}_{k,k-1} = \Phi_{k,k-1} \mathbf{P}_{k-1} \Phi_{k,k-1}^T + \mathbf{Q}_{k-1} \quad 3.29$$

### Update

In the measurement update, the Kalman gain matrix  $\mathbf{K}_k$  is computed as

$$\mathbf{K}_k = \mathbf{P}_{k,k-1} \mathbf{H}_k^T (\mathbf{H}_k \mathbf{P}_{k,k-1} \mathbf{H}_k^T + \mathbf{R}_k)^{-1} . \quad 3.30$$

The *posteriori* estimate  $\delta\hat{\mathbf{x}}_k$  is derived using  $\mathbf{K}_k$ , the priori state vector  $\delta\hat{\mathbf{x}}_{k,k-1}$ , and the input  $\delta\mathbf{Z}_k$ :

$$\delta\hat{\mathbf{x}}_k = \delta\hat{\mathbf{x}}_{k,k-1} + \mathbf{K}_k (\delta\mathbf{Z}_k - \mathbf{H}_k \delta\hat{\mathbf{x}}_{k,k-1}) \quad 3.31$$

The *posteriori* matrix  $\mathbf{P}_k$ , at time  $t_k$  is then calculated by

$$\mathbf{P}_k = (\mathbf{I} - \mathbf{K}_k \mathbf{H}_k) \mathbf{P}_{k,k-1} \quad 3.32$$

### 3.3.2 INS error models

The GPS/INS integrated filter for the ultra-tight integration is based on tight integration. Therefore the integrated filter has the combination of the INS error states and GPS error states. In this section, the INS error equations are described in detail.

After perturbations of the INS mechanization equations, i.e. Equation (3.4), the error model is represented by a series of differential equations as follows.

The position error equations are related to the position and velocity (Yang 2008, El-Sheimy 2008, Jekeli 2001, Shin 2001), thus

$$\delta\ddot{\mathbf{r}}^l = \mathbf{F}_{rr} \delta\dot{\mathbf{r}}^l + \mathbf{F}_{rv} \delta\mathbf{v}^l \quad 3.33$$

where

$$\mathbf{F}_{rr} = \begin{bmatrix} 0 & \frac{v^E}{M+h} \tan \varphi & -\frac{v^E}{N+h} \\ 0 & 0 & -\frac{v^N}{M+h} \\ 0 & 0 & 0 \end{bmatrix}$$

$$\mathbf{F}_{rv} = \begin{bmatrix} 1 & 0 & 0 \\ 0 & 1 & 0 \\ 0 & 0 & 1 \end{bmatrix}$$

$$\delta \mathbf{r}^l \text{ is the position error vector } \delta \mathbf{r}^l = [\delta r^E \quad \delta r^N \quad \delta r^U]$$

The velocity error equations can be expressed as (Yong 2008, El-Sheimy 2008, Jekeli 2001, Shin 2001)

$$\delta \dot{\mathbf{v}}^l = \mathbf{F}_{vr} \delta \mathbf{r}^l + \mathbf{F}_{vv} \delta \mathbf{v}^l + \mathbf{F}_{va} \delta \mathbf{e}^l + \mathbf{R}_b^l \delta \mathbf{f}_{ib}^b \quad 3.34$$

where

$$\mathbf{F}_{vr} = \begin{bmatrix} 0 & \frac{2\omega_e(v^U \sin \varphi + v^N \cos \varphi) + v^N \dot{\lambda} / \cos \varphi}{M+h} & \frac{(v^U \cos \varphi - v^N \sin \varphi) \dot{\lambda}}{N+h} \\ 0 & -\frac{2\omega_e v^E \cos \varphi + v^E \dot{\lambda} / \cos \varphi}{N+h} & \frac{v^U \dot{\varphi}}{M+h} + \frac{v^E \dot{\lambda}}{N+h} \\ 0 & -\frac{2\omega_e v^E \sin \varphi}{M+h} & \frac{2\gamma}{R+h} \end{bmatrix}$$

$\dot{\varphi}$  and  $\dot{\lambda}$  are the latitude and longitude rates,  $\gamma$  is the normal gravity that varies

with the altitude, and which can be approximated by  $\gamma = \gamma_0 \left( \frac{R}{R+h} \right)^2$ .  $\gamma_0$  is the

normal gravity at the surface of the earth.  $R = \sqrt{MN}$ .

$$\mathbf{F}_{vv} = \begin{bmatrix} \frac{-v^U + v^N \tan \varphi}{N+h} & (2\omega_e + \dot{\lambda}) \sin \varphi & -(2\omega_e + \dot{\lambda}) \cos \varphi \\ -(2\omega_e + \dot{\lambda}) \sin \varphi & -\frac{v^U}{M+h} & -\dot{\varphi} \\ (2\omega_e + \dot{\lambda}) \cos \varphi & 2\dot{\varphi} & 0 \end{bmatrix}$$

$$\mathbf{F}_{v\varepsilon} = \begin{bmatrix} 0 & f^U & -f^N \\ -f^U & 0 & f^E \\ f^N & -f^E & 0 \end{bmatrix}, \quad f^E, f^N, f^U \text{ are specific force expressed in the local}$$

level frame.

$\delta \mathbf{r}_{ib}^b$  is the accelerometer sensor error.

The attitude error equations can be expressed as (Yang 2008, El-Sheimy 2008, Jekeli 2001, Shin 2001)

$$\delta \dot{\boldsymbol{\varepsilon}}^l = \mathbf{F}_{\varepsilon r} \delta \mathbf{r}^l + \mathbf{F}_{\varepsilon v} \delta \mathbf{v}^l + \mathbf{F}_{\varepsilon \varepsilon} \delta \boldsymbol{\varepsilon}^l + \mathbf{R}_b^l \delta \boldsymbol{\omega}_{ib}^b \quad 3.35$$

where

$$\mathbf{F}_{\varepsilon r} = \begin{bmatrix} 0 & 0 & -\frac{\dot{\varphi}}{M+h} \\ \frac{\omega_e \sin \varphi}{M+h} & 0 & \frac{\dot{\lambda} \cos \varphi}{N+h} \\ -\frac{\omega_e \cos \varphi + \dot{\lambda} / \cos \varphi}{M+h} & 0 & \frac{\dot{\lambda} \sin \varphi}{N+h} \end{bmatrix}$$

$$\mathbf{F}_{\varepsilon v} = \begin{bmatrix} 0 & \frac{1}{M+h} & 0 \\ -\frac{1}{N+h} & 0 & 0 \\ -\frac{\tan \varphi}{N+h} & 0 & 0 \end{bmatrix}$$

$$\mathbf{F}_{ee} = \begin{bmatrix} 0 & (\omega_e + \dot{\lambda}) \sin \varphi & -(\omega_e + \dot{\lambda}) \cos \varphi \\ -(\omega_e + \dot{\lambda}) \sin \varphi & 0 & -\dot{\varphi} \\ (\omega_e + \dot{\lambda}) \cos \varphi & \dot{\varphi} & 0 \end{bmatrix}$$

$\delta\boldsymbol{\omega}_{ib}^b$  is the gyroscope sensor noise.

The sensor errors  $\delta\mathbf{f}_{ib}^b, \delta\boldsymbol{\omega}_{ib}^b$  are commonly modeled by the combination of correlated sensor bias and the driving noise. Such a model is given as (El-Sheimy 2008, Godha 2006, Petovello 2003)

$$\delta\mathbf{f}_{ib}^b = \mathbf{b} + \mathbf{w}_f \quad 3.36$$

$$\delta\boldsymbol{\omega}_{ib}^b = \mathbf{d} + \mathbf{w}_\omega \quad 3.37$$

where

$\mathbf{b}$  is the accelerometer bias;

$\mathbf{d}$  is the gyroscope bias;

$\mathbf{w}_f$  is the wideband noise of the accelerometer, and

$\mathbf{w}_\omega$  is the wideband noise of the gyroscope.

The sensor bias is often modeled as a first order Gauss-Markov process, which can be represented by (El-Sheimy 2008, Godha 2006, Petovello 2003)

$$\begin{bmatrix} \dot{\mathbf{b}} \\ \dot{\mathbf{d}} \end{bmatrix} = \begin{bmatrix} -\frac{1}{\tau_b} & 0_{3 \times 3} \\ 0_{3 \times 3} & -\frac{1}{\tau_d} \end{bmatrix} \begin{bmatrix} \mathbf{b} \\ \mathbf{d} \end{bmatrix} + \begin{bmatrix} \boldsymbol{\eta}_b \\ \boldsymbol{\eta}_d \end{bmatrix} \quad 3.38$$

where  $\tau_b, \tau_d$  are the correlation time for the accelerometer and gyro respectively.  $\boldsymbol{\eta}_b$  and  $\boldsymbol{\eta}_d$  are the driving noise of the Gauss-Markov process with the spectral density

$\mathbf{q}_b, \mathbf{q}_d$ . The spectral density  $\mathbf{q}_i$  can be determined by the variance  $\sigma_i$  of the Gauss-Markov process as

$$\mathbf{q}_i = \sqrt{\frac{2\sigma_i}{\tau_i}} \quad 3.39$$

Further information about IMUs with different qualities and the sensor noise parameterization methods will be introduced in Chapter 4.

### 3.3.3 GPS error models

As mentioned in Section 3.2.2, the ultra-tight integration filter also combines with the GPS error states. Typically, two error states are used to model the GPS receiver at the pseudorange and Doppler level (Kaplan 1996, Godha 2006). The two states are the receiver clock bias and the clock drift, both of which are modeled as a random walk process. The clock error states are defined in the units of metres and metres per second. Therefore, the GPS error model can be written as (Brown & Hwang 1992)

$$\begin{bmatrix} ct \\ cdt \end{bmatrix} = \begin{bmatrix} 0 & 1 \\ 0 & 0 \end{bmatrix} \begin{bmatrix} ct \\ cdt \end{bmatrix} + \begin{bmatrix} \eta_t \\ \eta_{\delta} \end{bmatrix} \quad 3.40$$

where

$ct$  is the receive clock bias state;

$cdt$  is the receiver clock drift state;

$\eta_t$  is the driving noise of clock bias with spectral density  $q_t$ ;

$\eta_{\delta}$  is the driving noise of clock drift with spectral density  $q_{\delta}$ .

For computing the clock error spectral densities, a standard clock stability model is used where the spectral densities are computed as (Brown & Hwang 1992)

$$\begin{aligned} q_t &= h_0 \\ q_{\delta t} &= 8\pi^2 h_2 \end{aligned} \tag{3.41}$$

where  $h_0$  and  $h_2$  are Allan variance parameters that describe clock stability. Details about the Allan variance will be presented in Chapter 4.

### 3.3.4 GPS/INS integration filter

The ultra-tight integration filter includes the INS error states and the GPS error states.

Therefore the integration filter includes 17 states, which are given by

$$\delta \mathbf{x} = [\delta \mathbf{r}^l \quad ct \quad \delta \mathbf{v}^l \quad c\delta t \quad \delta \boldsymbol{\epsilon}^l \quad \mathbf{b} \quad \mathbf{d}] \tag{3.42}$$

Therefore, the system model of the integration filter is

$$\delta \dot{\mathbf{x}} = \mathbf{F} \delta \mathbf{x} + \mathbf{G} \mathbf{w}$$

where, the dynamic matrix  $\mathbf{F}$ , shaping matrix  $\mathbf{G}$  and processing noise matrix  $\mathbf{w}$  have been described in the previous two sections.

The differences between GPS measured pseudoranges and pseudorange rates and INS derived pseudoranges and pseudorange rates are used as the observation vector  $\delta \mathbf{Z}$  in the integration filter. It is noted that the relationship between pseudorange rate and Doppler is as follows:

$$f = \frac{\dot{\rho}}{\lambda_{L1}} \quad 3.43$$

where  $f$  is the Doppler and  $\dot{\rho}$  is the corresponding range rate.

Assume there are  $n$  satellites in-view, the measurement misclosures can be written as:

$$\delta \mathbf{Z} = \begin{bmatrix} \delta \mathbf{Z}_\rho \\ \delta \mathbf{Z}_{\dot{\rho}} \end{bmatrix} = \begin{bmatrix} \boldsymbol{\rho}_{GPS} \\ \dot{\boldsymbol{\rho}}_{GPS} \end{bmatrix}_{2n \times 1} - \begin{bmatrix} \boldsymbol{\rho}_{INS} \\ \dot{\boldsymbol{\rho}}_{INS} \end{bmatrix}_{2n \times 1} \quad 3.44$$

where,  $\delta \mathbf{Z}_\rho$  and  $\delta \mathbf{Z}_{\dot{\rho}}$  represent the range and range rate misclosures;  $\boldsymbol{\rho}_{GPS}$  and  $\dot{\boldsymbol{\rho}}_{GPS}$  are the GPS pseudorange and pseudorange rate measurements;  $\boldsymbol{\rho}_{INS}$  and  $\dot{\boldsymbol{\rho}}_{INS}$  are the INS estimated pseudorange and pseudorange rate measurements. The  $i$ -th elements of  $\boldsymbol{\rho}_{INS}$  and  $\dot{\boldsymbol{\rho}}_{INS}$  are the INS derived pseudorange  $\rho_{INS}^i$  and pseudorange rate  $\dot{\rho}_{INS}^i$  for the  $i$ -th satellite respectively, which can be computed as

$$\rho_{INS}^i = \sqrt{(r_{s,x}^i - \hat{r}_x^e)^2 + (r_{s,y}^i - \hat{r}_y^e)^2 + (r_{s,z}^i - \hat{r}_z^e)^2} + c\hat{t} \quad 3.45$$

$$\dot{\rho}_{INS}^i = -\hat{e}_x^i (v_{s,x}^i - \hat{v}_x^e) + \hat{e}_y^i (v_{s,y}^i - \hat{v}_y^e) + \hat{e}_z^i (v_{s,z}^i - \hat{v}_z^e) + c\hat{d}\hat{t} \quad 3.46$$

where

$\lambda_{L1}$  is the L1 carrier wavelength,

$[r_{s,x}^i \ r_{s,y}^i \ r_{s,z}^i]^T$  is the position vector of the  $i$ -th satellite in e-frame;

$[v_{s,x}^i \ v_{s,y}^i \ v_{s,z}^i]^T$  is the velocity vector of the  $i$ -th satellite in e-frame;

$[\hat{r}_x^e \ \hat{r}_y^e \ \hat{r}_z^e]^T$  is the position vector of the INS transformed into e-frame;

$[\hat{v}_x^e \ \hat{v}_y^e \ \hat{v}_z^e]^T$  is the velocity vector of the INS transformed into e-frame;

$[\hat{e}_x^i \ \hat{e}_y^i \ \hat{e}_z^i]^T$  is the unit vector along the line of sight from the INS to GPS

expressed in e-frame;

$\hat{c}t$ ,  $\hat{c}d\hat{t}$  are the estimated receiver clock bias and drift.

The line of sight vector can be written as

$$\mathbf{e}^i = [\hat{e}_x^i \ \hat{e}_y^i \ \hat{e}_z^i]^T = \left[ \frac{r_{s,x}^i - \hat{r}_x^e}{\|\mathbf{r}_s^i - \hat{\mathbf{r}}^e\|} \quad \frac{r_{s,y}^i - \hat{r}_y^e}{\|\mathbf{r}_s^i - \hat{\mathbf{r}}^e\|} \quad \frac{r_{s,z}^i - \hat{r}_z^e}{\|\mathbf{r}_s^i - \hat{\mathbf{r}}^e\|} \right]^T \quad 3.47$$

where,  $\|\mathbf{r}_s^i - \hat{\mathbf{r}}^e\|$  denotes the distance between the satellite position and the INS estimated position.

The GPS pseudorange measurement on the  $i$ -th satellite after compensation for the tropospheric and ionospheric delays, satellite orbit and clock errors can be written as (Kaplan 1996, Lachapelle 2007)

$$\rho_{GPS}^i = \|\mathbf{r}_s^i - \mathbf{r}^e\| + ct + v_\rho^i. \quad 3.48$$

Similarly, the pseudorange rate measurement on the  $i$ -th satellite is given by

$$\dot{\rho}_{GPS}^i = -e_x^i(v_{s,x}^i - v_x^e) + e_y^i(v_{s,y}^i - v_y^e) + e_z^i(v_{s,z}^i - v_z^e) + \hat{c}d\hat{t} + v_{\dot{\rho}}^i \quad 3.49$$

where,  $\mathbf{r}^e$ ,  $\mathbf{v}^e$ ,  $\mathbf{e}^i$  are the true position, velocity and line of sight vectors;  $ct$  and  $\hat{c}d\hat{t}$  are the true receiver clock bias and drift.  $v_\rho^i$  and  $v_{\dot{\rho}}^i$  are the noise of the pseudorange and pseudorange rate respectively.

Combining Equation (3.45) and Equation (3.48) yields the range misclosure for the  $i$ -th satellite (Kaplan 1996, Lachapelle 2007):

$$\delta \mathbf{Z}_{\rho}^i = \rho_{GPS}^i - \rho_{INS}^i = \begin{bmatrix} e_x^i & e_y^i & e_z^i \end{bmatrix} \begin{bmatrix} \delta r_x^e \\ \delta r_y^e \\ \delta r_z^e \end{bmatrix}^T + c \delta t + v_{\rho}^i \quad 3.50$$

where  $\begin{bmatrix} \delta r_x^e & \delta r_y^e & \delta r_z^e \end{bmatrix}$  is the estimated position error from the integration filter expressed in the e-frame and  $c \delta t$  is the receiver clock bias error. Since the position error state in the integration filter is derived in the l-frame, the above equation can be rewritten as (Farrell 2008)

$$\delta \mathbf{Z}_{\rho}^i = \rho_{GPS}^i - \rho_{INS}^i = H_{\rho,1 \times 3}^i \begin{bmatrix} \delta r^E \\ \delta r^N \\ \delta r^U \end{bmatrix}^T + c \delta t + v_{\rho}^i \quad 3.51$$

where  $H_{\rho,1 \times 3}^i = \begin{bmatrix} -\cos(E) \sin(A) & -\cos(E) \cos(A) & -\sin(E) \end{bmatrix}$ , and  $A$  and  $E$  are the satellite elevation angle and azimuth respectively.

Similarly, when combining Equation (3.46) and Equation (3.49), the range rate misclosure for the  $i$ -th satellite is given as

$$\delta \mathbf{Z}_{\dot{\rho}}^i = \dot{\rho}_{GPS}^i - \dot{\rho}_{INS}^i = H_{\dot{\rho},1 \times 3}^i \begin{bmatrix} \delta v^E \\ \delta v^N \\ \delta v^U \end{bmatrix}^T + c \delta dt + v_{\dot{\rho}}^i \quad 3.52$$

where  $H_{\dot{\rho},1 \times 3}^i = \begin{bmatrix} -\cos(E) \sin(A) & -\cos(E) \cos(A) & -\sin(E) \end{bmatrix}$ .

Finally, the measurement model for the ultra-tight integration filter can be written as

$$\delta \mathbf{Z} = \begin{bmatrix} \delta \mathbf{Z}_\rho \\ \delta \mathbf{Z}_{\dot{\rho}} \end{bmatrix}_{2 \times n, 1} = \mathbf{H} \delta \mathbf{x} + \mathbf{v} \quad 3.53$$

where  $n$  is the number of satellites in view and the design matrix  $\mathbf{H}$  is given by

$$\mathbf{H} = \begin{bmatrix} \mathbf{H}_{\rho, n \times 3} & \mathbf{1}_{n \times 1} & \mathbf{0}_{n \times 3} & \mathbf{0}_{n \times 1} & \mathbf{0}_{n \times 9} \\ \mathbf{0}_{n \times 3} & \mathbf{0}_{n \times 1} & \mathbf{H}_{\dot{\rho}, n \times 3} & \mathbf{1}_{n \times 1} & \mathbf{0}_{n \times 9} \end{bmatrix} \quad 3.54$$

### 3.3.5 Channel filter

As discussed in Chapter 2, the ultra-tight GPS receiver implemented in this thesis employs a cascaded filter scheme. In this case, an EKF is used to generate the carrier Doppler, carrier phase and code phase estimates for individual tracking loops. Herein, the filter is called a channel filter. And the approach whereby tracking errors are estimated by a Kalman filter is called estimator-based tracking. Before operating in the ultra-tight mode, the receiver should be initialized with estimator-based tracking until stable position and velocity estimates are obtained to setup the INS initial states. At this time, the code and carrier NCO are directly controlled by the channel filter. When the receiver is switched to the ultra-tight model, direct feedback from the channel filter to the local signal generator is used for the carrier phase only, since the navigation solution accuracy from the integration filter is insufficient for carrier phase tracking. However, the code tracking loops are operated in vector-based mode at this time.

The major difference between the standard tracking and the EKF based tracking is that both PLL and DLL discriminators and loop filters are replaced by an EKF. Therefore both

code and carrier NCOs are updated by the EKF (before ultra-tight mode is initialized).

The structure of an EKF based tracking loop is shown in Figure 3.7

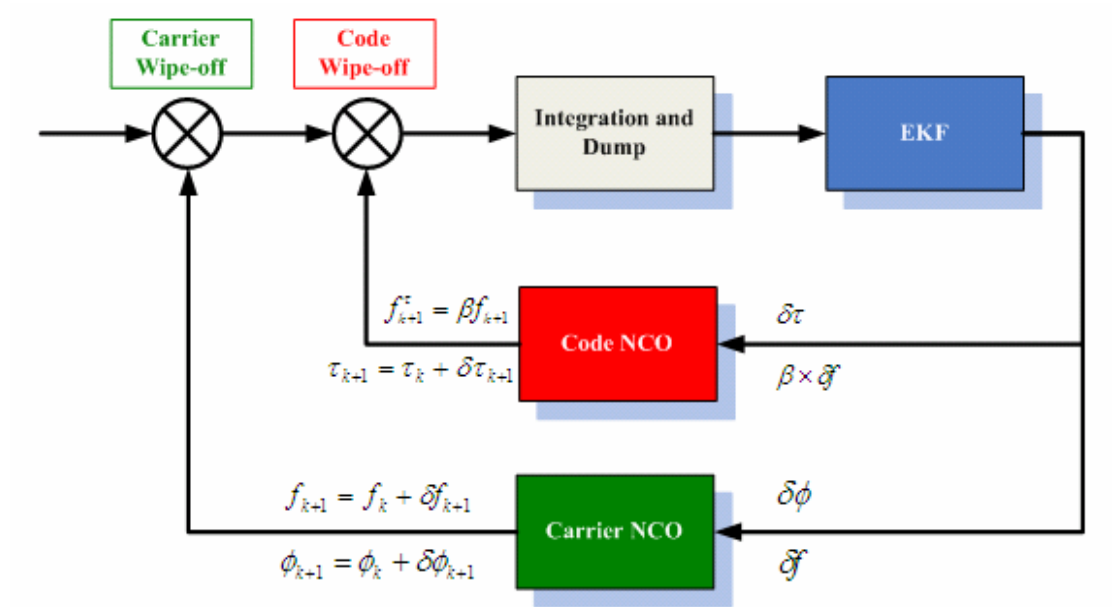


**Figure 3.7: Structure of EKF based tracking loop**

The incoming sampled IF signal is first mixed with the local carrier to complete the carrier wipe-off. After the carrier wipe-off, the signal is correlated with the local code. The local code and carrier is generated by the code and carrier NCOs respectively. Integration and dumping is performed after the IF signal is converted to a baseband signal after the carrier and code stripping process but prior to being passed to the EKF. The resulting in-phase and quadra-phase components are then sent to the Kalman filter to generate the tracking error estimates. For carrier tracking, both the estimated carrier phase and carrier Doppler ( $f_{k+1}$  and  $\phi_{k+1}$ ) are used to update the carrier NCO. The mathematical representation of the carrier NCO update is as follows

$$\begin{aligned} f_{k+1} &= f_k + \delta f_{k+1} \\ \phi_{k+1} &= \phi_k + \delta \phi_{k+1} \end{aligned} \quad 3.55$$

where  $\delta f_{k+1}, \delta \phi_{k+1}$  are the current Doppler and phase error estimates.  $f_k$  and  $\phi_k$  are the Doppler and phase at the previous epoch.

Similarly, the code Doppler  $f_{k+1}^\tau$  in units of chips per second, and the code phase  $\tau_{k+1}$  in units of chips, which control the code NCO, are given by

$$\begin{aligned} f_{k+1}^\tau &= \beta f_{k+1} \\ \tau_{k+1} &= \tau_k + \delta \tau_{k+1} \end{aligned} \quad 3.56$$

where  $\beta$  is the scale factor that converts units of Hertz to radians per second.  $\delta \tau_{k+1}$  is the code phase error estimate and  $\tau_k$  is the code phase at the previous epoch.

As described above, the EKF based channel filter plays an important role in the ultra-tight receiver. It estimates the tracking errors of each individual channel and these error estimates are used to correct the measurements for the integration filter and drive the NCOs. It is noted that when the receiver is operated in ultra-tight mode, the channel filter only updates the carrier phase. . The channel filter state vector is (Petovello & Lachapelle 2006)

$$\delta \mathbf{x} = [A \quad \delta \tau \quad \delta \phi \quad \delta f \quad \delta a]^T \quad 3.57$$

where  $A$  is the signal amplitude,  $\delta \tau$  is the code phase tracking error in units of chips,  $\delta \phi$  is the phase tracking error in units of rad,  $\delta f$  is the frequency tracking error in units

of rad/s, and  $\delta a$  is the frequency rate error of the NCO in units of rad/s<sup>2</sup>. It is noted that when the receiver is operated in the ultra-tight mode, the latter term models the residual INS acceleration error and not the full level of line-of-sight acceleration.

The system model for the filter, taken from Petovello & Lachapelle (2006), is given by

$$\begin{bmatrix} \dot{A} \\ \delta\dot{\tau} \\ \delta\dot{\phi} \\ \delta\dot{f} \\ \delta\dot{a} \end{bmatrix} = \begin{bmatrix} 0 & 0 & 0 & 0 & 0 \\ 0 & 0 & 0 & \beta & 0 \\ 0 & 0 & 0 & 1 & 0 \\ 0 & 0 & 0 & 0 & 1 \\ 0 & 0 & 0 & 0 & 0 \end{bmatrix} \begin{bmatrix} A \\ \delta\tau \\ \delta\phi \\ \delta f \\ \delta a \end{bmatrix} + \begin{bmatrix} 1 & 0 & 0 & 0 & 0 \\ 0 & 1 & \beta \cdot 2\pi f & 0 & 0 \\ 0 & 0 & 2\pi f & 0 & 0 \\ 0 & 0 & 0 & 2\pi f & 0 \\ 0 & 0 & 0 & 0 & 2\pi f / \lambda_{L1} \end{bmatrix} \begin{bmatrix} w_A \\ w_{\delta\tau} \\ w_{\delta\phi} \\ w_{\delta f} \\ w_{\delta a} \end{bmatrix} \quad 3.58$$

where

$f$  is the carrier frequency;

$\lambda_{L1}$  is the wavelength of GPS L1 signal;

$w_A$  is the driving noise of the amplitude;

$w_{\delta\tau}$  is the driving noise of the code tracking error that is included to account for code-carrier divergence due to the ionosphere;

$w_{\delta\phi}$  is the driving noise for the clock bias;

$w_{\delta f}$  is the driving noise for the clock drift;

$w_{\delta a}$  is the driving noise to account for line-of-sight acceleration. (e.g., Van Dierendonck et al 1984, Brown & Hwang 1992).

The discrete system model then can be written as:

$$\delta \mathbf{x}_{k+1} = \mathbf{\Phi} \delta \mathbf{x}_k + \mathbf{w}_k \quad 3.59$$

where the transition matrix can be derived from Equation (3.58) as

$$\mathbf{\Phi} = \begin{bmatrix} 1 & 0 & 0 & 0 & 0 \\ 0 & 1 & 0 & \beta \Delta T & \frac{1}{2} \beta \Delta T^2 \\ 0 & 0 & 1 & \Delta T & \frac{1}{2} \Delta T^2 \\ 0 & 0 & 0 & 1 & \Delta T \\ 0 & 0 & 0 & 0 & 1 \end{bmatrix} \quad 3.60$$

where  $\Delta T$  is the integration interval or the filter update interval.

The process noise model used herein is adapted from Psiaki & Jung (2002). The clock model is as described in Brown & Hwang (1992), while  $w_A$ ,  $w_{\delta\tau}$  and  $w_{\delta\tau}$  are modeled as white noise.

The observations are formed from the six in-phase and quadra-phase prompt, early, and late correlator outputs as

$$\mathbf{Z}_k = [I_E \quad I_P \quad I_L \quad Q_E \quad Q_P \quad Q_L]^T. \quad 3.61$$

The correlation outputs are given by:

$$I = A \cdot N \cdot R(\delta\tau - \Delta) \frac{\sin(\pi \cdot \delta f \cdot \Delta T)}{\pi \cdot \delta f \cdot \Delta T} \cos(\overline{\delta\phi}) \quad 3.62$$

$$Q = A \cdot N \cdot R(\delta\tau - \Delta) \frac{\sin(\pi \cdot \delta f \cdot \Delta T)}{\pi \cdot \delta f \cdot \Delta T} \sin(\overline{\delta\phi}) \quad 3.63$$

where  $R$  is the auto-correlation function of the code and  $\overline{\delta\phi}$  is the average carrier phase error over the integration interval, which can be written as (Psiaki 2002, Petovello 2006, 2008):

$$\overline{\delta\phi} = \delta\hat{\phi} - \frac{1}{2}\delta\hat{f}\Delta T + \frac{1}{6}\delta\hat{a}\Delta T^2 \quad 3.64$$

where  $\delta\hat{\phi}$ ,  $\delta\hat{f}$  and  $\delta\hat{a}$  are the estimated carrier phase, frequency and frequency rate errors at the end of the integration interval. Therefore, the design matrix can be obtained by taking the partial derivatives of the in-phase observation with respect to the EKF states as follows:

$$\begin{aligned} \frac{\partial I}{\partial A} &= \hat{N}R(\delta\hat{\tau} - \Delta) \cos(\overline{\delta\phi}) \\ \frac{\partial I}{\partial \delta\tau} &= \hat{N}\hat{A}\dot{R}(\delta\hat{\tau} - \Delta) \cos(\overline{\delta\phi}) \\ \frac{\partial I}{\partial \delta\phi} &= -\hat{N}\hat{A}R(\delta\hat{\tau} - \Delta) \sin(\overline{\delta\phi}) \\ \frac{\partial I}{\partial \delta f} &= -\frac{1}{2}\Delta T \cdot \hat{N} \cdot \hat{A}R(\delta\hat{\tau} - \Delta) \sin(\overline{\delta\phi}) \\ \frac{\partial I}{\partial \delta a} &= -\frac{1}{6}\Delta T^2 \cdot \hat{N} \cdot \hat{A}R(\delta\hat{\tau} - \Delta) \sin(\overline{\delta\phi}) \end{aligned} \quad 3.65$$

where  $\hat{A}$  and  $\delta\hat{\tau}$  are the estimated amplitude and code phase errors. It is noted that the ideal autocorrelation function  $R(t)$  is not differentiable. When the input RF signal has passed through a band-pass filter in the GPS front-end, the shape of the correlation peak also changes. A practical autocorrelation function can be written as polynomial approximation of  $R$ . Also, the data bit sign estimation is obtained using a hard decision (as opposed to a soft decision) when the signal power strength is relatively high (Izadpanah 2008):

$$\hat{N} = \begin{cases} 1 & I_p > 0 \\ -1 & I_p < 0 \end{cases} \quad 3.66$$

A similar approach can be applied to the quadra-phase observations as

$$\begin{aligned} \frac{\partial Q}{\partial A} &= \hat{N}R(\delta\hat{\tau} - \Delta)\sin(\overline{\delta\phi}) \\ \frac{\partial Q}{\partial \delta\tau} &= \hat{N}\hat{A}\dot{R}(\delta\hat{\tau} - \Delta)\sin(\overline{\delta\phi}) \\ \frac{\partial Q}{\partial \delta\phi} &= \hat{N}\hat{A}R(\delta\hat{\tau} - \Delta)\cos(\overline{\delta\phi}) \\ \frac{\partial Q}{\partial \delta f} &= \frac{1}{2}\Delta T \cdot \hat{N} \cdot \hat{A}R(\delta\hat{\tau} - \Delta)\cos(\overline{\delta\phi}) \\ \frac{\partial Q}{\partial \delta a} &= \frac{1}{6}\Delta T^2 \cdot \hat{N} \cdot \hat{A}R(\delta\hat{\tau} - \Delta)\cos(\overline{\delta\phi}) \end{aligned} \quad 3.67$$

The noise power of the measurements is given by (Petovello et al 2008)

$$\sigma_{n_i}^2 = \sigma_{n_i}^2 = \frac{N_0}{2\Delta T} \quad 3.68$$

where  $N_0$  is th power spectral density of the noise in units of W/Hz

### 3.3.6 Vector-based NCO updates

Having reviewed the ultra-tight integration filter and the channel filter, the vector-based NCO updates are discussed in this section.

When the receiver is operated in the ultra-tight mode, the position and velocity estimated from the integration filter are used to control the local NCOs. The update rate of NCOs mainly depends on the IMU output rate since the GPS measurement update rate is usually lower than the IMU output rate. Between the GPS measurement updates, the INS derived

Doppler and pseudorange measurements are used to compute the Doppler and code phase which are sent to update the NCOs. Because the transmitted signal is corrupted by a variety of errors such as the satellite clock error, ionospheric error and tropospheric error, the received signal's code phase and Doppler are affected. In addition, the phase wind-up effect changes the received carrier Doppler (Kouba & Héroux 2001, Petovello et al 2008). Since the INS derived pseudorange and Doppler are computed based on the true range and Doppler, those errors should be compensated before they are applied to the NCOs.

Therefore the INS derived code phase, which is used to update the code NCO for the  $i$ -th satellite is given as (Lashley 2006)

$$\tau_{INS}^i = \text{mod}\left(t_{receiver} \cdot f_c - \frac{f_c(\rho_{INS}^i + ct - ct_s + \Delta d_{tr} + c\Delta d_g)}{c}, 1023\right) \quad 3.69$$

where the function  $\text{mod}(A, B)$  computes the remainder of  $A/B$ ,

$t_{receiver}$  is the receiver time;

$f_c$  is the code chipping rate;

$\rho_{INS}^i$  is the INS derived range before error compensation;

$ct$  is the receiver clock bias in metres;

$ct_s$  is the satellite clock bias in metres;

$\Delta d_{tr}$  is the tropospheric delay in metres;

$c\Delta d_g$  is the group delay in metres.

Similarly, the INS derived Doppler, which is used to update the carrier NCO for the  $i$ -th satellite is given as (Lashley & Bevely 2006, Yang 2008)

$$f_{INS}^i = \frac{\dot{\rho}_{INS}^i + cdt - cdt_s}{\lambda_{L1}} + \omega_{ib}^{b,z} \quad 3.70$$

where

$\dot{\rho}_{INS}^i$  is the INS derived range rate before error compensation;

$cdt$  is the receiver clock drift;

$cdt_s$  is the satellite clock drift;

$\omega_{ib}^{b,z}$  is the antenna's rotation rate around the vertical axis which is used to compensate for the phase wind-up effect.

## **CHAPTER FOUR: ULTRA-TIGHTLY COUPLED GPS /VEHICLE SENSOR INTEGRATION**

Having discussed the ultra-tight integration of GPS and INS in the previous chapter, this chapter focuses on the ultra-tightly coupled GPS and vehicle sensor integration. The chapter begins with an overview of vehicle sensors with emphasis on modelling the low cost MEMS inertial sensor errors. In order to identify and characterize the random noise of the inertial sensors available in land vehicles, the Allan variance is applied and discussed in Section 4.2. Then details about the approach to deal with integration of reduced MEMS IMU are presented in Section 4.3. Finally, the use of wheel speed sensors to enhance the integrated system is described in Section 4.4.

### **4.1 Overview of Vehicle Sensors**

Modern vehicles are often equipped with various sensors and a central control unit for improved safety and operational stability. A typical vehicle sensor setup is illustrated in Figure 4.1. Wheel speed sensors are located at each of the four wheel of the vehicle to provide the wheel rotation velocity. The inertial sensors as introduced in the previous chapter offer angular velocity and acceleration information. The steering angle sensor located on the front wheel axis is used to measure the front tire turning angle respect to the neutral position. The outputs of these sensors are connected to the central control unit by Controller–area network bus (CAN-bus) which is a vehicle bus standard designed to allow microcontrollers and devices to communicate with each other within a vehicle without a host computer. The central control unit improves the safety of a vehicle's stability by detecting and minimizing skids (Gillespie & Thomas 1992, Wang 1993).

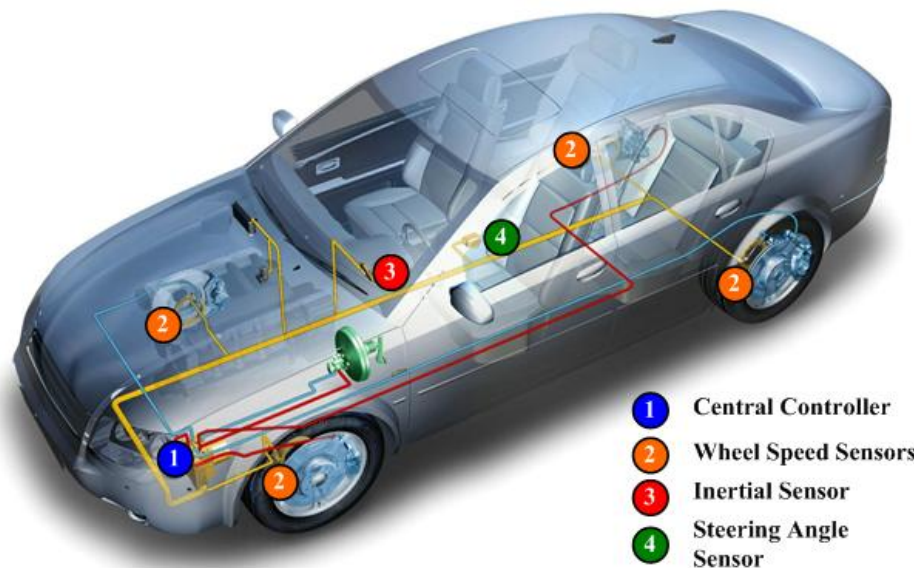


**Figure 4.1: Typical vehicle sensor configurations (Modified Bosch 2009)**

During normal driving, the central controller works in the background, continuously monitoring steering and vehicle direction. It compares the driver's intended direction by measuring steering angle via the steering angle sensor to the vehicle's actual direction by measuring accelerations, angular velocities, and individual road wheel speeds via inertial sensors and wheel speed sensors. The central control unit only intervenes when it detects loss of steering control, i.e. when the vehicle is not going where the driver is steering. At this time, it automatically applies the brakes to help "steer" the vehicle where the driver intends to go. Braking is automatically applied to individual wheels, such as the outer front wheel to counter oversteer, or the inner rear wheel to counter understeer (Rajamani 2008, Liebmenn et al 2004, Gillespie & Thomas 1992, Wong 1993).

For vehicle navigation applications, these vehicle sensors originally designed for the safety and stability control can be integrated with GPS to provide more accurate and

reliable navigation solutions (Gao 2007). GPS/INS integration strategies have been comprehensively discussed in the previous chapter. However, because of the cost-sensitive nature of vehicular applications, low cost MEMS sensors are often used. In addition, for purposes of stability control, only the yaw rate and horizontal acceleration information are of interest (Rajamani 2008, Gillespie & Thomas 1992). Therefore full IMUs with six degrees of freedom are often simplified to a reduced configuration (“reduced IMU”) such as with two horizontal accelerometers and one vertical gyroscope to further decrease the production cost (as will be considered herein). In order to integrate GPS with reduced MEMS IMU, the INS error model described in the previous chapter should be modified accordingly (Yang 2008, Sun 2008, Niu 2007b). Specifically, the pseudo signal approach is used in this thesis to replace the omitted sensor outputs. The concept of pseudo signals will be discussed in more detail in Section 4.3. In addition to inertial sensors, wheel speed sensors that provide the longitudinal velocity in the vehicle frame can also be used to update the integrated navigation filter. Details about integration with wheel speed sensor are presented in Section 4.4.

#### ***4.1.1 MEMS IMU***

With advances in MEMS technology in recent decades, MEMS-based inertial sensors are widely used in the applications which were not previously feasible with conventional INS. due to the cost and size limits. The immediate start-up time, low power consumption, weight and cost of these sensors, which benefits from high volume manufacturing techniques and flexible rugged packaging options, satisfies the requirements for commercial applications such as vehicle navigation and control (Titterton & Weston

2004). Therefore, current on-board vehicle sensors usually exploit MEMS IMUs (full or reduced). However, due to the relative lack of maturity of this technology, the performance of these sensors is limited (Shin et al 2005), which causes the navigation solution to degrade rapidly in the absence of an aiding source. Table 4.1 shows the error characteristics of a tactical grade IMU and two consumer grade MEMS IMUs to facilitate direct performance comparison.

**Table 4.1: Specifications of different IMUs**

Sensor	HG1700	Crista	Production
	<b>Accelerometer</b>		
<b>In run bias (mg)</b>	<b>1</b>	<b>2.5</b>	<b>0.5</b>
<b>Turn on bias (mg)</b>	<b>N/A</b>	<b>30</b>	<b>30</b>
<b>Scale factor (PPM)</b>	<b>300</b>	<b>10000</b>	<b>N/A</b>
<b>VRW (deg/h/<math>\sqrt{Hz}</math>)</b>	<b>2.16e-6</b>	<b>300e-6</b>	<b>100e-6</b>
	<b>Gyroscope</b>		
<b>In run bias (deg/h)</b>	<b>1</b>	<b>1000</b>	<b>140</b>
<b>Turn on bias (deg/h)</b>	<b>N/A</b>	<b>5000</b>	<b>1000</b>
<b>Scale factor (PPM)</b>	<b>150</b>	<b>10000</b>	<b>N/A</b>
<b>ARW(deg/h/<math>\sqrt{Hz}</math>)</b>	<b>5.5</b>	<b>220</b>	<b>140</b>

The two MEMS IMU used in this thesis are the Crista IMU from Cloud Cap Technology Inc. and the production IMU from BEI Systron Donner Inertial, the parameters of which are shown in Table 4.1. The production IMU used this study is the reduced IMU which is equipped in the GM vehicle used for testing. The tactical grade IMU used as comparison

is the Honeywell HG1700 IMU (Godha 2006, Petovello 2003). The quality of an IMU is often differentiated by the quality of the gyros (El-Sheimy 2004, Petovello 2003) and as can be seen, the MEMS IMUs have much larger gyro noise than the HG1700. As shown in the table, the turn-on gyro bias of Crista and the production IMUs are over 1000 °/h, which are much larger than those in higher grade IMUs. Also, the MEMS IMU exhibits much larger in-run bias drift compared to 1 °/h for a tactical grade system.

#### ***4.1.2 Wheel speed sensor***

A wheel speed sensor (WSS) or vehicle speed sensor (VSS) is a type of tachometer. It is a device used for reading the speed of a vehicle's wheel rotation rate which can be used to calculate the wheel speed. It usually consists of a toothed ring and pickup (Curtis 2005, Christopher 2003). Figure 4.2 shows a schematic of the operational principles of a wheel speed sensor. The wheel speed sensor produces a current related to the change in reluctance due to the rotation of a steel gear attached to the wheels. Thus, the current is an alternating signal whose frequency and amplitude are both proportional to the speed of rotation. Then, the signal condition circuit uses this varying current to detect both the rising and falling edge of the gear teeth. These edges are counted and a running count is passed to the single board computer at every sample time (Christopher 2003, Gao 2007).

Therefore the wheel speed  $v_{WSS}^V$  expressed in v-frame can be given by

$$v_{WSS}^V = 2\pi R \frac{N_k - N_{k-1}}{\Delta T \cdot K} \quad 4.1$$

where

$R$  is the radius of the tire;

$K$  is the resolution of the wheel speed sensor (pulse per revolution);

$\Delta T$  is the sampling period;

$N_k, N_{k-1}$  are two consecutive recorded wheel pulses.

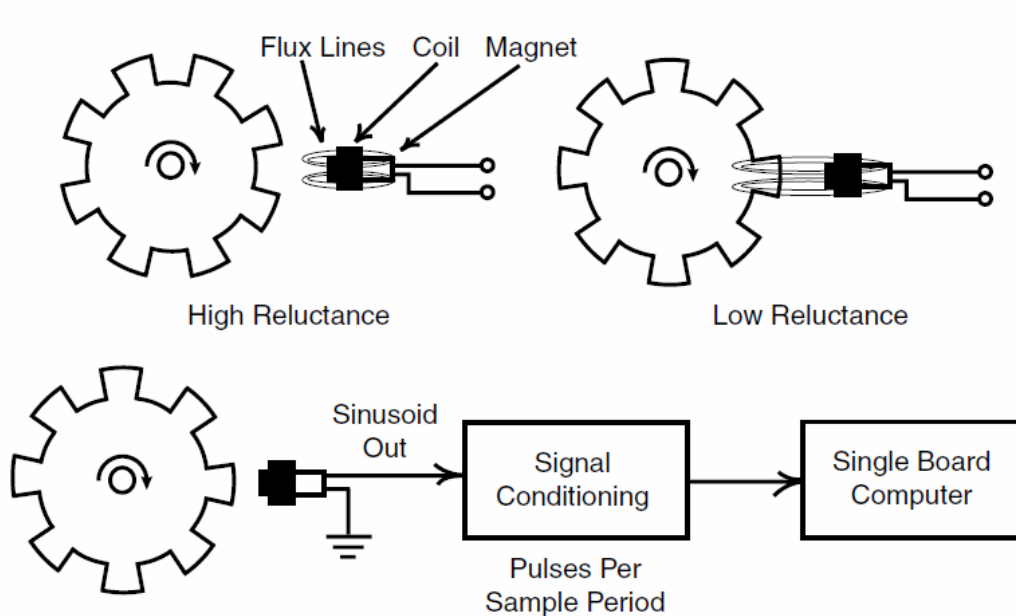


**Figure 4.2: Operation principles of wheel speed sensor**

It is important to point out that such sensors have advantages and disadvantages that should be considered before using them for specific applications. The advantages are their flexibility, small size and low cost, which make them suitable for land vehicle navigation and control. However, on the downside, they suffer heavily from undesirable signals or interference (Hernández 2003). Furthermore, high accurate wheel speed outputs are only obtained when the vehicle is running at a relatively high speed (e.g. above 5 km/h ). On balance, despite these disadvantages, wheel speed sensors are the most suitable choice to measure the rotation speed of wheels in today's automobiles and are the most commonly used in land vehicle (Hernández 2003, Christopher 2003).

## 4.2 IMU Noise Characterization

Before using the inertial sensors, the various sensor errors should be identified and the noise characteristics should be determined in order to use them in the integration Kalman filter.

### 4.2.1 Sensor model

The outputs of an IMU can be written as (Godha 2006, Petovello 2003)

$$\tilde{\mathbf{f}}_{ib}^b = \mathbf{f}_{ib}^b + \mathbf{b} + \mathbf{S}_f \mathbf{f}_{ib}^b + \mathbf{b}_{to} + \mathbf{w}_f \quad 4.2$$

$$\tilde{\boldsymbol{\omega}}_{ib}^b = \boldsymbol{\omega}_{ib}^b + \mathbf{d} + \mathbf{S}_\omega \boldsymbol{\omega}_{ib}^b + \mathbf{d}_{to} + \mathbf{w}_\omega \quad 4.3$$

where

$\tilde{\mathbf{f}}_{ib}^b$ ,  $\tilde{\boldsymbol{\omega}}_{ib}^b$  are measured acceleration and angular velocity;

$\mathbf{f}_{ib}^b$ ,  $\boldsymbol{\omega}_{ib}^b$  are the true acceleration and angular velocity;

$\mathbf{b}$ ,  $\mathbf{d}$  are the in-run bias;

$\mathbf{b}_{to}$ ,  $\mathbf{d}_{to}$  are the turn-on bias;

$\mathbf{S}_f$ ,  $\mathbf{S}_\omega$  are the scale factors;

$\mathbf{w}_f$ ,  $\mathbf{w}_\omega$  are the wide-band noise.

Typically, for land vehicle navigation applications the sensor turn-on biases and scale factor errors of high-end IMUs (HG1700) can be neglected without losing too much accuracy (Godha 2006). For these IMUs the measurements are considered to have just the in-run bias and wide-band noise for ease of implementation (Petovello 2003) as illustrated

in the previous chapter. However, in case of MEMS IMUs, the sensor scale factor errors and the turn-on biases are higher than those of tactical IMUs, as shown in Table 4.1. Although the two kinds of errors are deterministic in nature, they typically vary from one turn-on to another. Therefore, it is not feasible to calibrate them every time the sensor is turned on. Thus  $\mathbf{b}_{to}$  and  $\mathbf{d}_{to}$  are modeled as random constants.  $\mathbf{S}_f$  and  $\mathbf{S}_\omega$  can be modeled as first-order Gauss-Markov processes. They can be represented mathematically by

$$\begin{aligned}\dot{\mathbf{b}}_{to} &= 0 \\ \dot{\mathbf{d}}_{to} &= 0\end{aligned}\tag{4.4}$$

$$\begin{bmatrix} \dot{\mathbf{S}}_f \\ \dot{\mathbf{S}}_\omega \end{bmatrix} = \begin{bmatrix} -\frac{1}{\tau_{sf}} & \mathbf{0}_{3 \times 3} \\ \mathbf{0}_{3 \times 3} & -\frac{1}{\tau_{s\omega}} \end{bmatrix} \begin{bmatrix} \mathbf{S}_f \\ \mathbf{S}_\omega \end{bmatrix} + \begin{bmatrix} \boldsymbol{\eta}_{sf} \\ \boldsymbol{\eta}_{s\omega} \end{bmatrix}\tag{4.5}$$

where  $\tau_{sf}$  and  $\tau_{s\omega}$  are the correlation time of accelerometers and gyros respectively;  $\boldsymbol{\eta}_{sf}$  and  $\boldsymbol{\eta}_{s\omega}$  are the driving noise.

However, compared with the errors induced from turn-on bias, in-run bias and wide-band noise, the contribution of scale factors is relatively small for MEMS IMUs. Therefore, in the implementation of the integration filter, the scale factor states are not included, in order to reduce the computation burden of the integration algorithm.

### 4.2.2 Allan variance

The stochastic parameters in Equation (3.36) and Equation (3.37) can be estimated using various identification techniques. Such techniques include the Allan variance and autocorrelation functions.

The Allan variance was first introduced in Allan (1966) as a means to quantify the precision of atomic oscillators. It is a time domain analysis technique originally developed to study the frequency stability of oscillators. Because of the close analogies to inertial sensors, the method has been adapted to random noise characterization of a variety of errors (IEEE Std952-1997). The Allan variance quantifies the various stochastically-driven error sources present in inertial sensor output and is best represented on a log-log plot.

### Methodology

Assume there are  $N$  consecutive data points of sampled IMU measurements, each having a sample period of  $\Delta t$  and forming a cluster of  $n$  consecutive data points (with  $n < N/2$ ) as shown in Figure 4.3.

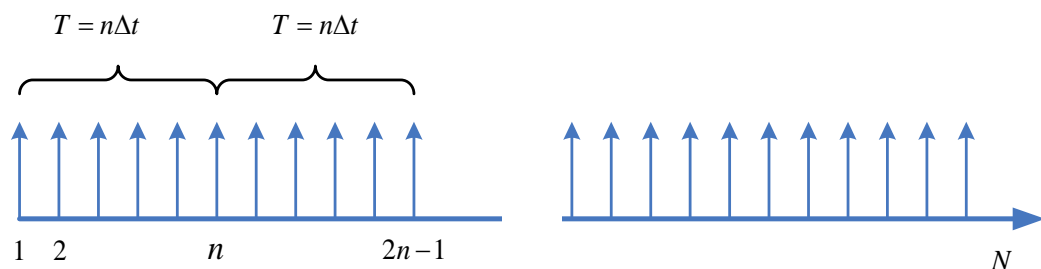


**Figure 4.3: Clusters used for Allan variance computation**

Associated with each cluster is a time  $T$ , which is equal to  $T = n\Delta t$ . If the outputs of IMUs are angular velocities or accelerations denoted by  $\Omega(t)$ , the cluster average is defined as (IEEE Std952-1997):

$$\bar{\Omega}_k(T) = \frac{1}{T} \int_{t_k}^{t_k+T} \Omega(t) dt \quad 4.6$$

where  $\bar{\Omega}_k(t)$  represents the cluster average of the output rate for a cluster which starts from the  $k$ -th data point and contains  $n$  samples. The cluster average for the next cluster is given by:

$$\bar{\Omega}_{k+1}(T) = \frac{1}{T} \int_{t_{k+1}}^{t_{k+1}+T} \Omega(t) dt \quad 4.7$$

where  $t_{k+1} = t_k + T$ .

Using the above two values, the Allan variance of length  $T$  is defined as

$$\sigma^2(T) = \frac{1}{2} \left\langle \left[ \bar{\Omega}_{k+1}(T) - \bar{\Omega}_k(T) \right]^2 \right\rangle \quad 4.8$$

where the triangle brackets denote the averaging operation over the ensemble of clusters.

Thus the above equation can be rewritten as (IEEE Std952-1997)

$$\sigma^2(T) = \frac{1}{2(N-2n)} \sum_{k=1}^{N-2n} \left[ \bar{\Omega}_{k+1}(T) - \bar{\Omega}_k(T) \right]^2. \quad 4.9$$

Clearly, for any finite number of data points ( $N$ ), a finite number of clusters of a fixed length ( $T$ ) can be determined. Hence, Equation (4.9) represents an estimation of the

quantity  $\sigma^2(T)$  whose quality of estimate depends on the number of independent clusters of a fixed length. The Allan variance can also be developed when the outputs of IMUs are angle increments or velocity increments as

$$\theta(t) = \int^t \Omega(t) dt . \quad 4.10$$

The lower integration limit is not specified, as only angle or velocity increments are employed in the definitions. Angle or velocity increment measurements are made at discrete times given by  $t = k\Delta t$ . Accordingly, the notation is simplified by writing  $\theta(k\Delta t) = \theta_k$ . Equations (4.6) and (4.7) can be rewritten as

$$\overline{\Omega}_k(T) = \frac{\theta_{k+n} - \theta_k}{T} \quad 4.11$$

$$\overline{\Omega}_{k+1}(T) = \frac{\theta_{k+2n} - \theta_{k+n}}{T} . \quad 4.12$$

Therefore, Equation (4.9) can be rewritten as (IEEE Std952-1997)

$$\sigma^2(T) = \frac{1}{2T^2(N-2n)} \sum_{k=1}^{N-2n} (\theta_{k+2n} - \theta_{k+n} + \theta_k)^2 . \quad 4.13$$

### Noise identification

The Allan variance is a measure of the stability of a sensor output. As such it must be related to the statistical properties of the intrinsic random processes, which in turn affects the sensor performance.

There is a unique relationship that exists between  $\sigma^2(T)$  and the power spectral density of the intrinsic random process. This relationship is (IEEE Std 952-1997)

$$\sigma^2(T) = 4 \int_0^{\infty} df \cdot S_{\Omega}(f) \frac{\sin^4(\pi f T)}{(\pi f T)^2} \quad 4.14$$

where  $S_{\Omega}(f)$  is the power spectral density of the intrinsic random process.

According to the log-log plot of Allan standard deviation versus cluster length, different noise terms can be identified and extracted. The different slopes seen on such a log-log plot indicate unique regions dominated by specific error sources. The relationships of various noise sources and Allan standard deviation are summarized in Table 4.2 (IEEE Std 952-1997):

**Table 4.2: Relationship between Allan variance and different errors**

Error Type	$\log(\sigma)$ vs $\log(T)$	Curve Slope	Coefficient Value
Quantization Noise	$\log(\sigma) = -\log(T) + \log(\sqrt{3}Q)$	-1	$Q = \sigma(\sqrt{3})$
Angle Random Walk	$\log(\sigma) = -\frac{1}{2}\log(T) + \log(N)$	$-\frac{1}{2}$	$N = \sigma(1)$
Rate Random Walk	$\log(\sigma) = \frac{1}{2}\log(T) + \log(K/\sqrt{3})$	$+\frac{1}{2}$	$K = \sigma(3)$
Correlated Noise	$\log(\sigma) = -\frac{1}{2}\log(T) + \log(q_c T_c)$ $\log(\sigma) = \frac{1}{2}\log(T) + \log(q_c / \sqrt{3})$	$\pm \frac{1}{2}$	$q_c T_c = \sigma(1)$ $q_c = \sigma(3)$

### 4.3 Ultra-tight Integration of GPS/Reduced IMU

As mentioned earlier, vehicles usually employ reduced IMUs to reduce cost. Therefore, the main objective for reduced IMU/GPS integration is to remove the reliance on the sensors that contribute less to the navigation solution, thereby enabling the same functionality with the reduced IMU. However, in order to do this, it is important to understand the contributions of each sensor within a full IMU.

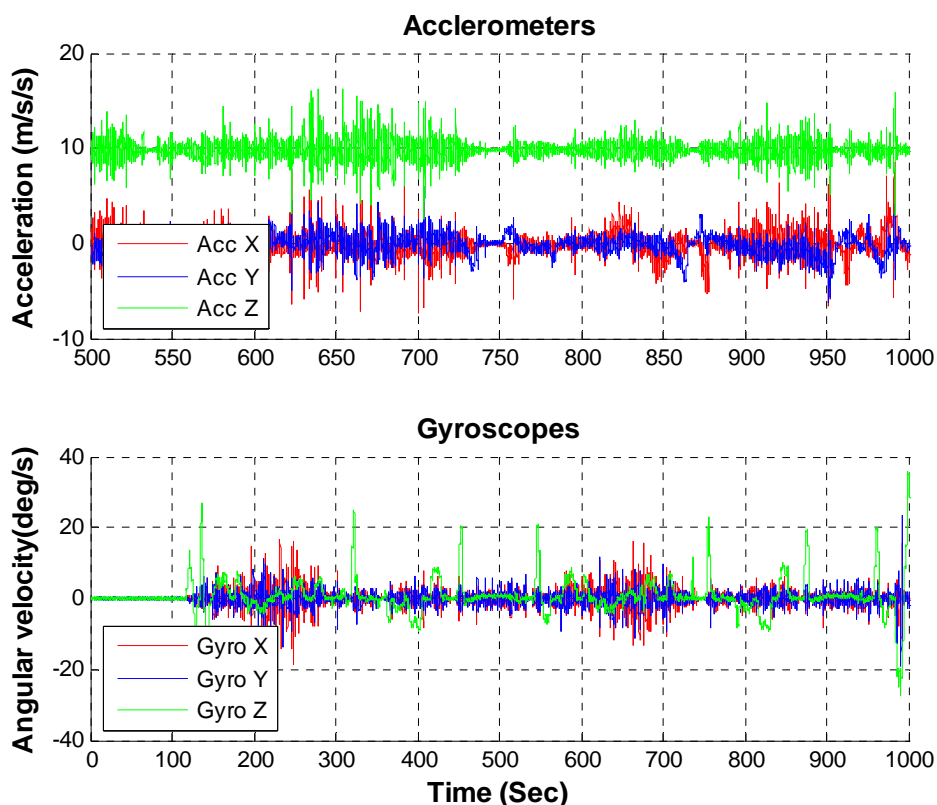


**Figure 4.4: Outputs of full IMU during typical vehicle dynamics**

Figure 4.4 shows the full IMU outputs during a typical land vehicle field test. Since land vehicles mainly run on relatively flat roads with pitch and roll typically less than five degrees, the output of the vertical accelerometer is composed mainly of the local gravity,

the road vibrations and vehicle suspension vibrations (Niu 2007b). Therefore the z-axis accelerometer outputs are considered as the sum of gravity and white noise. The accelerometer histogram is shown in Figure 4.5.

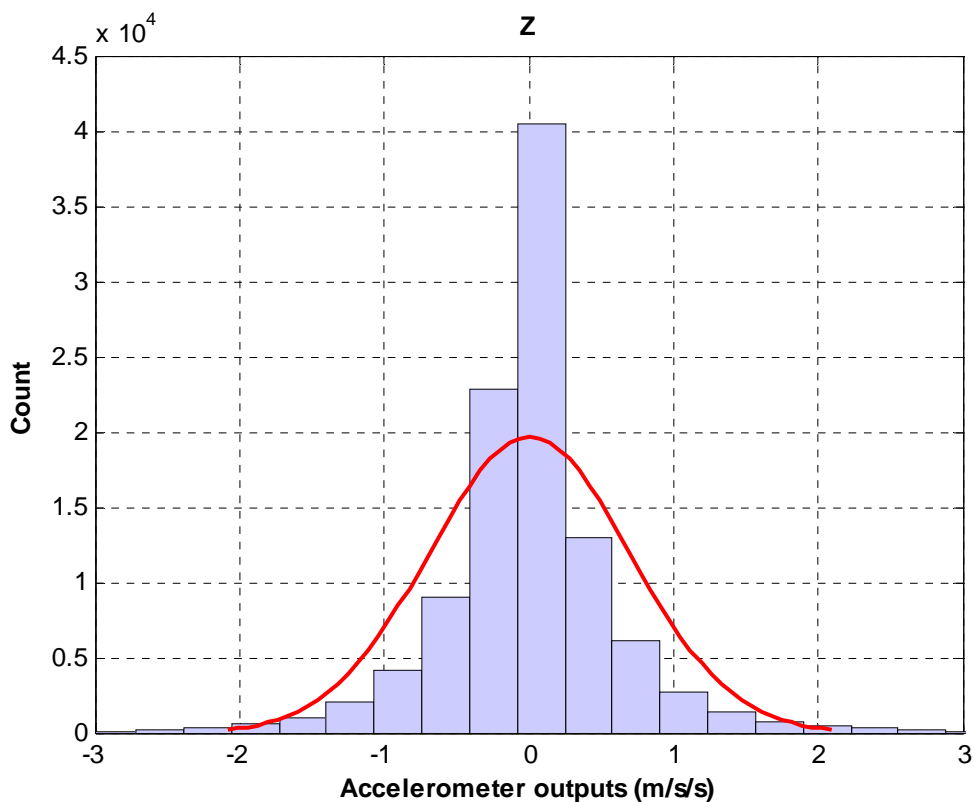


**Figure 4.5: Histogram plot of Z-acceleration outputs**

Similar analyses can be applied to the two horizontal gyros. The outputs of horizontal gyros are mainly related to pitch and roll dynamics which are relatively small compared to azimuth dynamics. Therefore, from the bottom plot of Figure 4.4, the outputs of the two horizontal gyros can be regarded as zero mean white noise. The corresponding histogram plot of the x and y-axis gyro outputs are shown in Figure 4.6. This verifies the underlying assumptions of the x and y axis gyros being mostly influenced by noise.

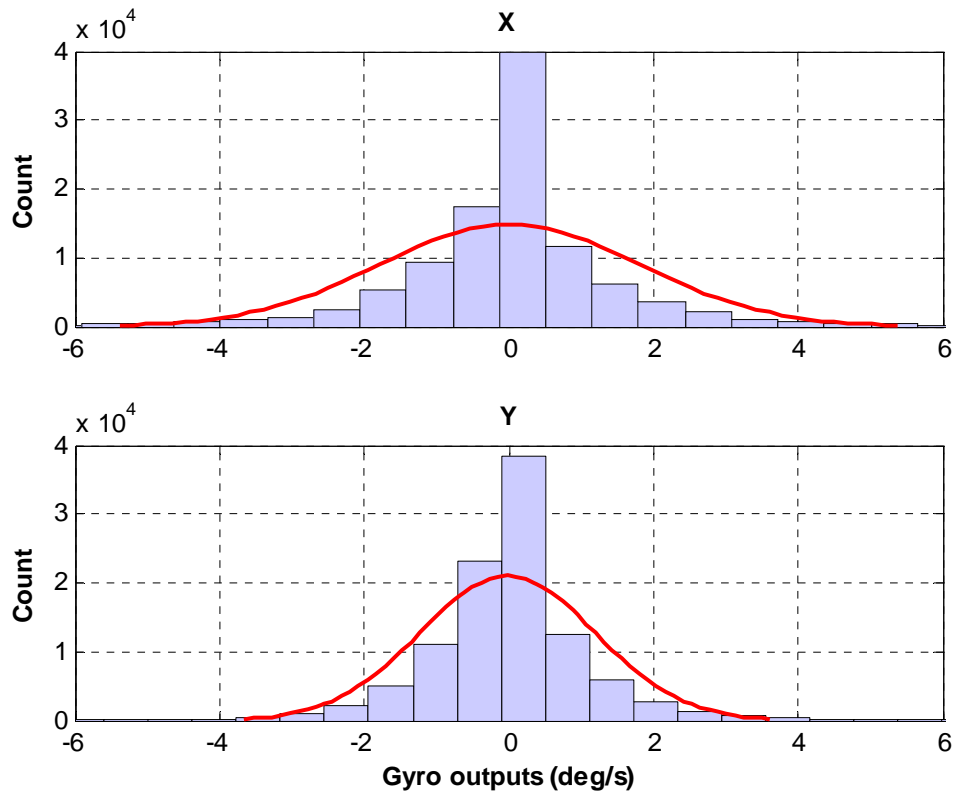


**Figure 4.6: Histogram plot of horizontal gyro outputs**

It is noted that the magnitude of the variation of sensor outputs is highly related to the vehicle dynamics. When the vehicle is static, the sensor outputs remains near zero as clearly shown in Figure 4.4.

Given these findings, the pseudo-signal approach proposed by Niu (2007b) is employed herein for the reduced IMU/GPS integration. The main concept of the pseudo-signal approach is to replace the unavailable sensors of the reduced IMU (i.e., the vertical accelerometer and horizontal gyros) by pseudo signals that have constant values. The

pseudo sensor noise is modeled as white noise. For horizontal gyros, zero outputs are assumed as pseudo signals. Similarly, the assumed vertical accelerometer outputs are local gravity. Then these pseudo signals together with real signals are used to calculate the position, velocity and attitude via the standard INS mechanizations. Finally, the obtained position, velocity and attitude are fed into the integration filter to obtain the final navigation solution. The block diagram of this method is shown in Figure 4.7:

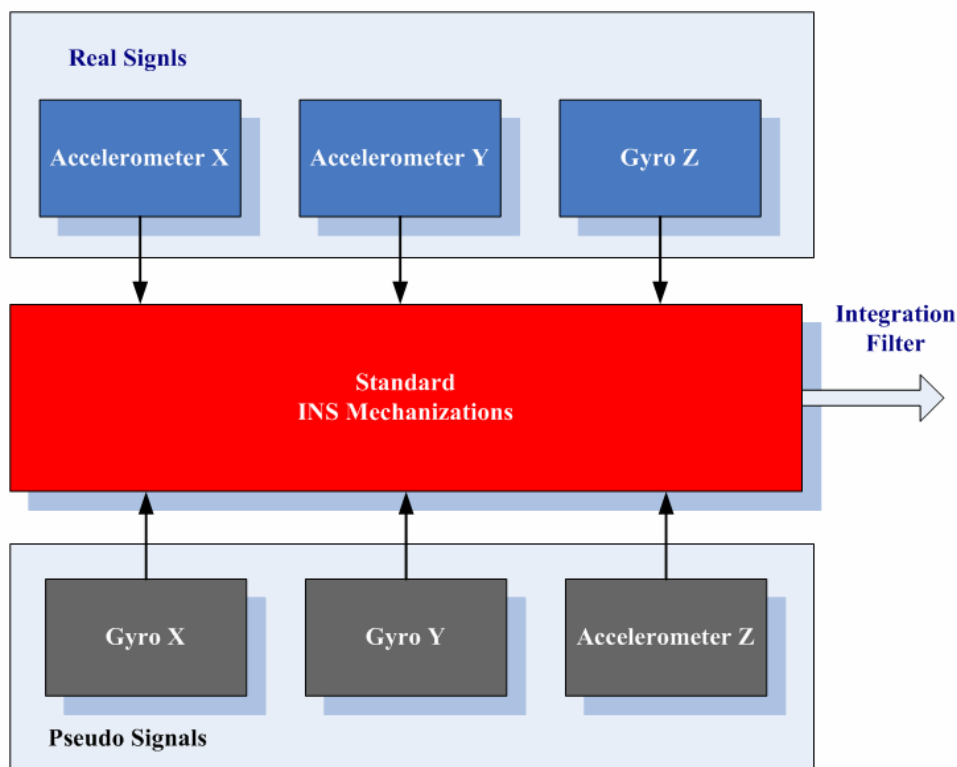


**Figure 4.7: Pseudo-signal approach for reduced IMU**

This approach offers a flexible solution to the reduced IMU/GPS integration problem without modifying the core integration algorithm. It can be easily applied to other IMU configurations such as three accelerometers and one vertical gyro as well. It reduces the

software and hardware development time and can be applied to existing GPS/INS integration systems.

The positioning accuracy of the reduced INS mainly depends on vehicle dynamics and local terrain. It has a relatively better navigation solution when the variations of the vehicle dynamics and local terrain are small during the measurement updates (Sun et al 2008). Field test results in the next chapter are used to analyze the performance of the reduced IMU/GPS system.

#### **4.4 Ultra-tight Integration of Wheel Speed Sensor**

In order to limit the errors induced by the reduced IMU/GPS integrated system, the wheel speed sensor and non-holonomic constraints are applied in this work. The three-dimensional velocity updates derived from the wheel speed and non-holonomic constraints are feed into the integration filter to improve the navigation solution. Since the code and carrier NCOs are controlled by the navigation solution when the receiver is operated in ultra-tight mode, the tracking loops will also benefits from the improved position and velocity estimates.

##### ***4.4.1 Non-holonomic constraints***

The vehicle velocity constraints are derived assuming that the vehicle does not slip in the cross track direction of the vehicle's body, which is a reasonable assumption for travel in a constant direction. A second assumption is that the vehicle stays on the ground, i.e. it does not jump off of the ground. If both assumptions are true, then the velocity of the

vehicle in the direction perpendicular to the movement of the vehicle can be regarded as zero (Dissanayake 2000, Niu et al 2007a, Shin 2001, Gao 2007). Since the two assumptions are valid under most normal driving conditions, the additional description of the vehicle dynamics provided by the constraints improves navigation performance.

If the b-frame is aligned with the v-frame by the rotation matrix from the b-frame to the v-frame, the non-holonomic constraints can be written as

$$\begin{aligned} v_x^{b(v)} &\approx 0 \\ v_z^{b(v)} &\approx 0 \end{aligned} \quad 4.15$$

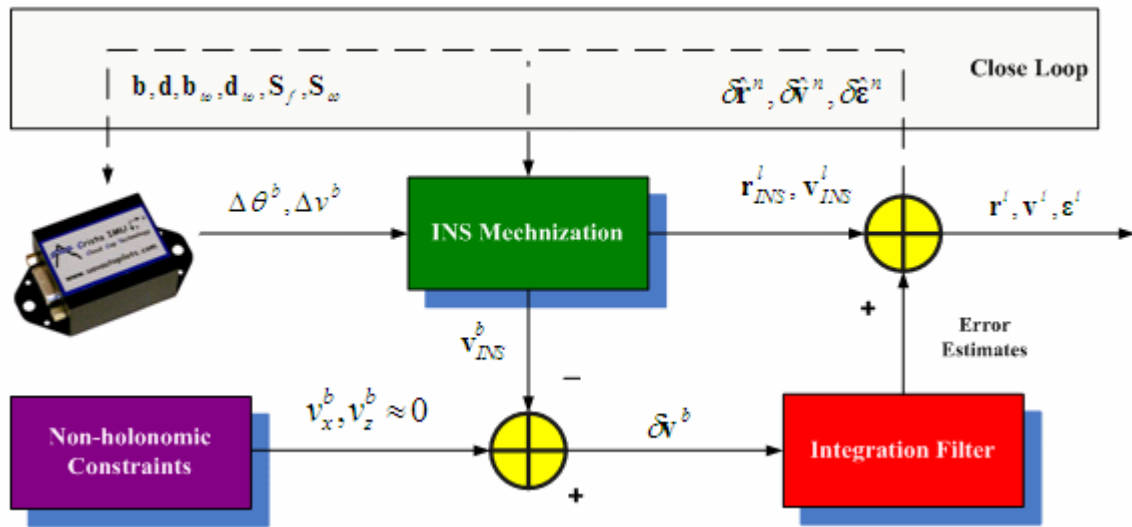


**Figure 4.8: Block diagram of filter updates using non-holonomic constraints**

The corresponding block diagram of the integration filter updates is illustrated in Figure 4.8. The difference between the INS derived body frame velocity and the assumed non-holonomic constraints are fed into the integration filter. The error correction



Since the tire radius is slowly changing due to variations in the road conditions and tire pressure (Kubo 1999, Gao 2007), the longitudinal velocity obtained from a wheel speed sensor can be represented as

$$\hat{v}_{WSS} = (R + \delta R)\omega_{WSS} + n_{WSS} \quad 4.16$$

where  $R$  is the radius of the tire,  $\omega_{WSS}$  is the angular velocity of the wheel revolution and  $n_{WSS}$  is the measurement noise. If the true velocity is defined as  $v_{WSS} = R\omega_{WSS}$  and

the scale factor  $S_{WSS} = \frac{\delta R}{R}$ , Equation (4.16) can be rewritten as

$$\hat{v}_{WSS} = (1 + S_{WSS})v_{WSS} + n_{WSS}. \quad 4.17$$

The measurement model for the 3D velocity updates can be obtained by a perturbation of the b-frame velocity as

$$\hat{\mathbf{v}}_{INS}^b = \mathbf{v}^b + \delta \mathbf{v}^b = \left[ (I + E^l) R_b^l \right]^T (\mathbf{v}^l + \delta \mathbf{v}^l) \quad 4.18$$

$$\delta \mathbf{v}^b = R_l^b (\delta \mathbf{v}^l + E^l \delta \mathbf{v}^l) \quad 4.19$$

where,  $E^l$  is the skew-symmetric matrix of the attitude error states. Finally, the measurement equations for the 3D velocity updates can be represented as follows:

$$\delta \mathbf{Z}_{3D} = \mathbf{v}_{3D} - \hat{\mathbf{v}}_{INS}^b = \begin{bmatrix} \mathbf{0}_{cons} \\ \hat{v}_{WSS} \\ \mathbf{0}_{cons} \end{bmatrix} - \begin{bmatrix} \hat{v}_x^b \\ \hat{v}_y^b \\ \hat{v}_z^b \end{bmatrix} = \mathbf{H}_{3D} \delta \mathbf{x} + \mathbf{n}_{3D} \quad 4.20$$

where  $\delta \mathbf{Z}_{3D}$  is the measurement misclosure of 3D velocity updates,  $v_{3D}$  is the 3D velocity constraints,  $\mathbf{0}_{cons}$  indicates the assumed zero velocity according to the

non-holonomic constraints,  $\hat{v}_{WSS}$  is the velocity provided by the wheel speed sensor,  $\hat{v}_x^b$ ,  $\hat{v}_y^b$  and  $\hat{v}_z^b$  are the estimated velocities in the b-frame from the INS;  $\mathbf{H}_{3D}$  is the design matrix and  $\mathbf{n}_{3D}$  is the measurement noise. The state vector of the integration filter in this case has 24 states:

$$\delta\mathbf{x} = \left[ \delta\mathbf{r}^l \quad ct \quad \delta\mathbf{v}^l \quad c\delta t \quad \delta\boldsymbol{\epsilon}^l \quad \mathbf{b} \quad \mathbf{d} \quad \mathbf{b}_{to} \quad \mathbf{d}_{to} \quad \mathbf{S}_{WSS} \right]^T \quad 4.21$$

where  $\mathbf{S}_{WSS}$  is the scale factor of the wheel speed sensor. The design matrix  $H_{3D}$  from Equation (4.20) can be written as follows:

$$H_{3D} = \begin{bmatrix} \mathbf{0}_{3 \times 4} & R_l^b & \mathbf{0}_{3 \times 1} & R_l^b E^l & \mathbf{0}_{3 \times 12} & v_{WSS} \end{bmatrix} \quad 4.22$$

The measurement noise for the non-holonomic constraints is computed based on a projection of the longitudinal velocity in the lateral and up directions due to the attitude error angles (Shin 2001, Godha 2006). Typically, the maximum velocity of a vehicle in the longitudinal direction is 35 m/s which is the equivalent to 126 km/h. Assuming a two degree attitude error in each direction, the projected velocity is around 1 m/s. Therefore the standard deviation of the measurement noise for the non-holonomic constraints can be set to 1 m/s. Although the noise of the two constraints is correlated, it is difficult to derive the relationship of the two noise components mathematically because the correlation is varying with vehicle dynamics. Therefore, they are assumed to be independent.

It is also noted that the contribution of the lever arm between the mass centre of the vehicle and the IMU to the non-holonomic constraint updates becomes significant when a

vehicle turns. This can be explained by Figure 4.10. This figure illustrates a simplified 2D vehicle model. It is also known as the bicycle model which has been extensively used for the representation of a ground vehicle (Ryu & Gerdes 2004; Bevly et al 2000, 2001; Shraim et al 2008; Ouladsine et al 2007; Anderson & Bevly 2004). The lever arm between the IMU and center of gravity (CG) of the vehicle is denoted as  $L_{CG}^{IMU}$ . If the non-holonomic constraints are held to be true at the CG point, the lateral velocity of INS  $v_{IMU}^x$  is still not zero and can be given by

$$v_{IMU}^y = \dot{\psi} L_{CG}^{IMU} . \quad 4.23$$

Therefore, when the vehicle turns, the lateral velocity should be compensated before non-holonomic constraints are used.

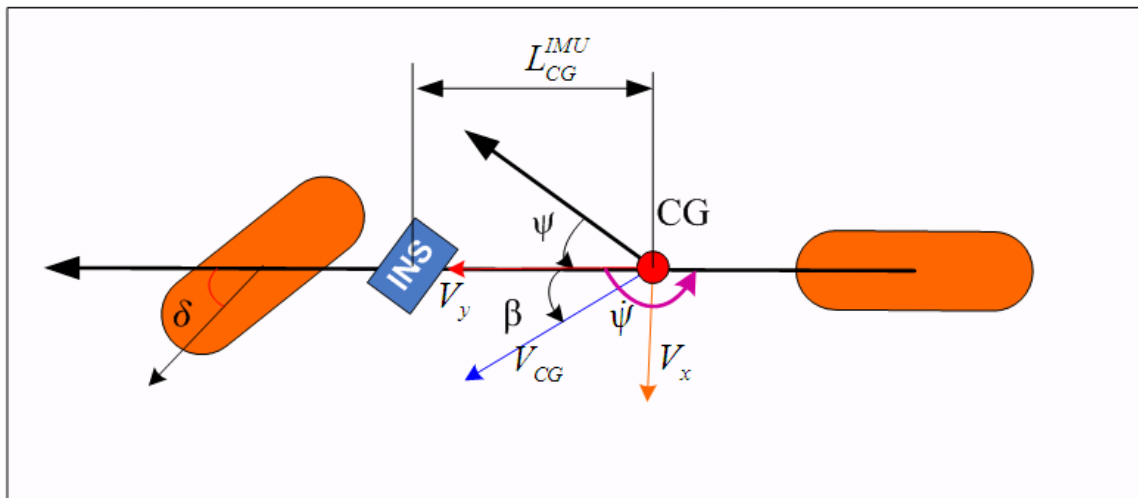


**Figure 4.10: Simplified vehicle model**

In order to analyze the contribution of the 3D velocity updates to the navigation solution, Equation (4.20) can be rewritten as follows:

$$\delta Z_{3D} = R_l^b \delta v^l + \begin{bmatrix} 0 & -v_z^b & v_y^b \\ v_z^b & 0 & -v_x^b \\ -v_y^b & v_x^b & 0 \end{bmatrix} \begin{bmatrix} \delta\theta \\ \delta\phi \\ \delta\psi \end{bmatrix}. \quad 4.24$$

From this, it can be shown that when a lateral velocity constraint is used the roll and azimuth estimates can be improved because the first row of the second term of the above equation has only two components. The two components  $-v_z^b$  and  $v_y^b$  are only correlated with roll and azimuth error states. However, the magnitude of  $v_y^b$  is usually much larger than that of  $v_z^b$ , thus the azimuth improvement should be larger than roll improvement in theory.

A similar analysis can be applied to the vertical constraint. The vertical velocity updates are correlated with pitch and roll estimates via  $-v_y^b$  and  $v_x^b$ . Since magnitude of  $v_y^b$  is usually much larger than  $v_x^b$ , the pitch error estimate has a higher correlation with vertical constraints. Therefore, the pitch has a larger improvement than roll in this case.

When it comes to the wheel speed sensor, its contribution to the improvement of the velocity estimates of the navigation solution is relatively small when the receiver is in an open sky environment (Li et al 2009). This can be explained by the principles of Kalman filter. Specifically, in the open sky scenario, the GPS Doppler derived velocity has a relatively higher accuracy than the wheel speed sensor derived velocity; therefore, the integration filter weighs more on GPS measurements. However, in a degraded signal

environment, the integration filter would give larger weight to the wheel speed sensor derived velocity since the quality of Doppler measurements in this case is much worse than that of the open sky case. Field test results are presented in the next chapter to verify this phenomenon.

It is also noted that when the vehicle is static, the wheel speed sensor outputs are exactly zero. In this case, Zero Velocity Updates (ZUPT) can be employed to update the integration filter instead of the 3D velocity updates. The measurement equation for the ZUPT is as follows:

$$\delta \mathbf{Z}_{ZUPT} = \begin{bmatrix} \mathbf{0}_{ZUPT} \\ \mathbf{0}_{ZUPT} \\ \mathbf{0}_{ZUPT} \end{bmatrix} - \begin{bmatrix} \hat{v}_x^l \\ \hat{v}_y^l \\ \hat{v}_z^l \end{bmatrix} = \mathbf{H}_{ZUPT} \delta \mathbf{x} + \mathbf{n}_{ZUPT} \quad 4.25$$

where  $\delta \mathbf{Z}_{ZUPT}$  is the measurement misclosure of ZUPT updates.  $\mathbf{0}_{ZUPT}$  indicates the zero velocity when the vehicle is static, which can be detected by checking the wheel speed sensor outputs.  $\hat{v}_x^l$ ,  $\hat{v}_y^l$  and  $\hat{v}_z^l$  are the estimated velocities in the l-frame from the INS.  $\mathbf{H}_{ZUPT}$  is the design matrix and  $\mathbf{n}_{ZUPT}$  is the measurement noise. The design matrix  $\mathbf{H}_{ZUPT}$  from Equation (4.26) can be written as follows:

$$\mathbf{H}_{ZUPT} = \begin{bmatrix} \mathbf{0}_{3 \times 4} & \mathbf{I}_{3 \times 3} & \mathbf{0}_{3 \times 17} \end{bmatrix} \quad 4.26$$

## **CHAPTER FIVE: FIELD TEST RESULTS AND PERFORMANCE ANALYSIS**

Having explained the operational principles of the ultra-tight GPS receiver, this chapter uses field test results to verify the feasibility of the previously mentioned algorithms. The field test was conducted under two scenarios: open sky and foliage. The chapter begins with the field test description in Section 5.1. Then the data processing procedure is described in Section 5.2. After that, the data analysis strategies are introduced in Section 5.3. Finally the open sky and foliage test results and analysis are presented in Section 5.4 and Section 5.5, respectively.

### **5.1 Field Test Description**

The field test was conducted in Calgary, Alberta. The main objective of the test was to collect GPS and IMU measurements in different environments. Different qualities of the IMUs (in-vehicle production IMU, HG1700, external production IMU, Crista MEMS IMU) are included to allow for an assessment of their relative performance. GPS data was logged in the form of measurements (pseudorange, Doppler, carrier phase, etc.) and IF samples.

#### ***5.1.1 Equipment setup***

A schematic of the test setup is shown in Figure 5.1. A NovAtel 702 antenna was used to receive the GPS L1 signal which was then split into three branches. The first branch was fed to a National Instruments (NI)-based front-end; the second one was connected with a NovAtel SPAN™ system. The third one was connected to the NavBox developed at the University of Calgary (details below). The front-end down-converted the signal to an

intermediate frequency (IF) of 0.42 MHz and sampled it at 5 MHz (complex) with 16 bit quantization level. Also noted is that a relatively high quality oscillator was used in the front-end. The samples were recorded to disk for post-processing. The SPAN™ system consists of a NovAtel OEM4 receiver and an IMU, in this case a Honeywell HG1700AG11 IMU (“HG1700”). The HG1700 is a tactical-grade IMU with a turn-on gyro bias of 1 deg/h which is synchronized by the NovAtel OEM4 receiver. Raw GPS pseudorange and range rate measurements were logged from the SPAN™ system at 1 Hz and raw IMU data (i.e., velocity and angular increments) from HG1700 was logged at 100 Hz into a Compact Flash (CF) card. The NavBox was used to collect Crista IMU data. The Crista IMU was synchronized by a NovAtel receiver inside the NavBox. The raw IMU measurements were logged into a Secure Digital (SD) card at 50 Hz. The single antenna was powered by the NovAtel OEM4 receiver. Therefore DC blocks were used at the other two branches after the signal splitter in order to isolate the power from the NavBox and the front-end into the antenna.

Apart from the HG1700 and the Crista IMU, data from the onboard vehicle sensors, including one lateral accelerometer, one vertical gyro, four wheel speed sensors and one steering angle sensor, were received by the CAN-Bus receiver (“CANcaseXL”) (the steering angle sensor data is not used in the thesis). The laptop was used to record the data from CANcaseXL and to time tag (in a relative sense) each received data record. The relative time between records is used to determine the sampling rate of each vehicle sensor. The absolute time of the measurements in the GPS time scale is then established through a post-mission comparison of the data with the HG1700 data.

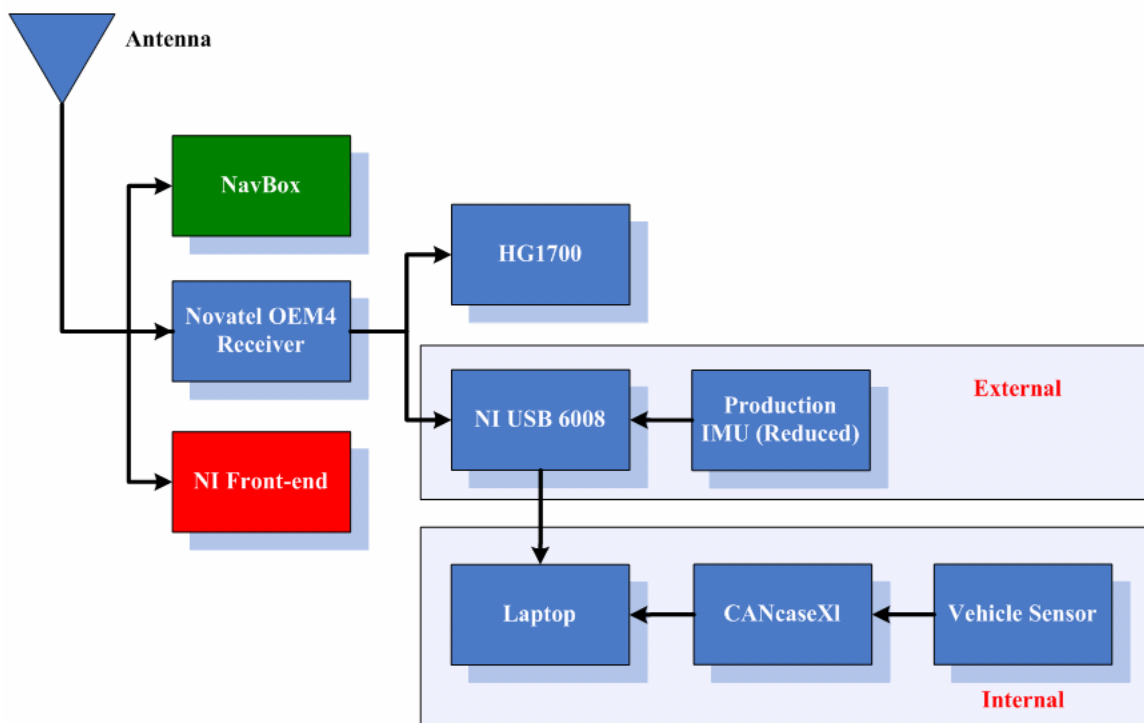


**Figure 5.1: Schematic of vehicle equipment setup**

In addition to the internal 2009 GMC Acadia vehicle sensor described above, an external production sensor (“external Production IMU”) containing two lateral accelerometers and one gyro (of the same quality as that inside the vehicle) was also included in the test. Data from the external production IMU was time tagged by the PPS signal from the NovAtel OEM4 receiver and collected by an NI data acquisition device, namely a NI USB 6008 data acquisition board. The received data from this device was also recorded by the laptop. The sampling rate of the external production IMU is 100 Hz.

It is noted that except for the internal production IMU, the other IMUs including the HG1700, Crista and external production sensor were rigidly mounted on the floor of the Acadia 2009. The NovAtel antenna was mounted on the top of the vehicle. All the

equipment was powered by either the vehicle itself or additional batteries. The picture of the test setup inside and outside the vehicle is shown in Figure 5.2. The NI front-end was powered by three batteries and the NovAtel SPAN™ system by the vehicle.



**Figure 5.2: Equipment setup**

In order to generate a reference solution using DGPS/INS integration, a NovAtel OEM4 receiver was setup on a building roof at the University of Calgary to act as the base station for DGPS operation. The raw pseudorange and Doppler measurement rate for this receiver was also 1 Hz.

### ***5.1.2 Test environments***

The field test was performed in two different environments, namely under open sky and under foliage. For each scenario, the test was initialized with a two minute static alignment to allow the inertial system to determine initial attitude with sufficient accuracy (for the tactical grade unit).

The open sky test was conducted in the Hamptons neighborhood of Northwest Calgary. This area has a relatively clear view of the sky and thus provides good GPS satellite visibility as shown in Figure 5.3. The test lasted about 20 minutes and a maximum of nine satellites were in view. Figure 5.4 and Figure 5.5 show the sky plot and trajectory of the test, respectively. The test route was selected to include enough local terrain variations to evaluate the worst-case positioning and attitude accuracy of the reduced IMU system for land vehicle navigation applications. The trajectory was traversed twice for repeatability.



**Figure 5.3: Open sky test environment**



The foliage test, was conducted in the Brentwood neighborhood of Calgary. Data from foliage scenario is used to analyze the performance of ultra-tight integration of GPS/vehicle sensors in degraded signal environments. The test route included areas with heavy foliage as shown in Figure 5.6. As can be seen, in some areas, the sky is only partially obscured by trees while in other areas the foliage is quite dense and covers nearly the entire sky. The trajectory is shown in Figure 5.7. Four loops were traversed in this test. The test lasted about ten minutes and a maximum of eight satellites were in view, as shown in Figure 5.8.



**Figure 5.6: Foliage test environment**



## **5.2 Data Processing**

Having explained the field test, the collected data were processed for performance analysis. The data processing procedure is described in the following sections.

### ***5.2.1 Reference solution***

To order to evaluate the performance of the ultra-tight integration of GPS/vehicle sensors, a reference navigation solution is required. The reference solution was generated using a loosely coupled DGPS and HG1700 data. The DGPS solution was obtained using the C<sup>3</sup>NAV<sup>2</sup>™ software package developed by PLAN group of the University of Calgary. The noise parameters of the HG1700 can be obtained in Petovello (2003). From previous data collections, the root mean square (RMS) errors of the reference solution (per axis) is decimetre-level for position and centimetre per second-level for velocity. The attitude solution is accurate to about 0.03 degrees for pitch and roll, and 0.17 degrees for azimuth (Godha 2006).

### ***5.2.2 Noise identification of the production IMU***

The Allan Variance method is adapted to random noise characterization of a variety of inertial sensor errors in this work. The noise parameters of the Crista are presented in Godha (2006). Using the technique introduced in Chapter 4, 24 hours of static data from the external production IMU was collected to generate the Allan Variance plot. The Allan standard deviation plots of the production IMU are shown in Figure 5.9 and Figure 5.10, respectively.

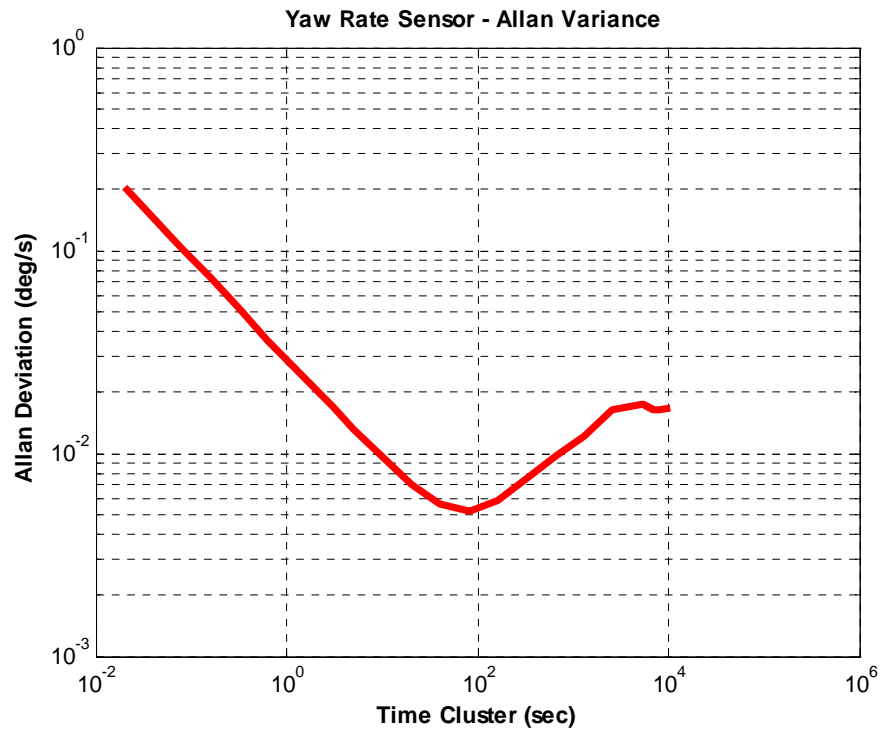


**Figure 5.9: Allan deviation plot of the production gyro**

As shown in Figure 5.9, the initial downward slope indicates the sensor's primary error source is angular random walk, or white noise, where for higher averaging times, the variance increases with a convex down shape, indicating the dominant error source is exponentially correlated noise, otherwise known as a Gauss-Markov process. It is noted that the shape of the curve is related to how long the dataset is used for the Allan variance computation. In addition, the longer the dataset, the more accurately the noise parameter is identified. (Brown & Hwang 1992). Therefore, the figure verifies the previously defined (Chapter 3) inertial sensor error model, which is a combination of white noise and Gauss-Markov noise. A similar analysis can be applied to accelerometers of the production sensor. The longitudinal and lateral accelerometers have similar noise characteristics as shown in Figure 5.10.

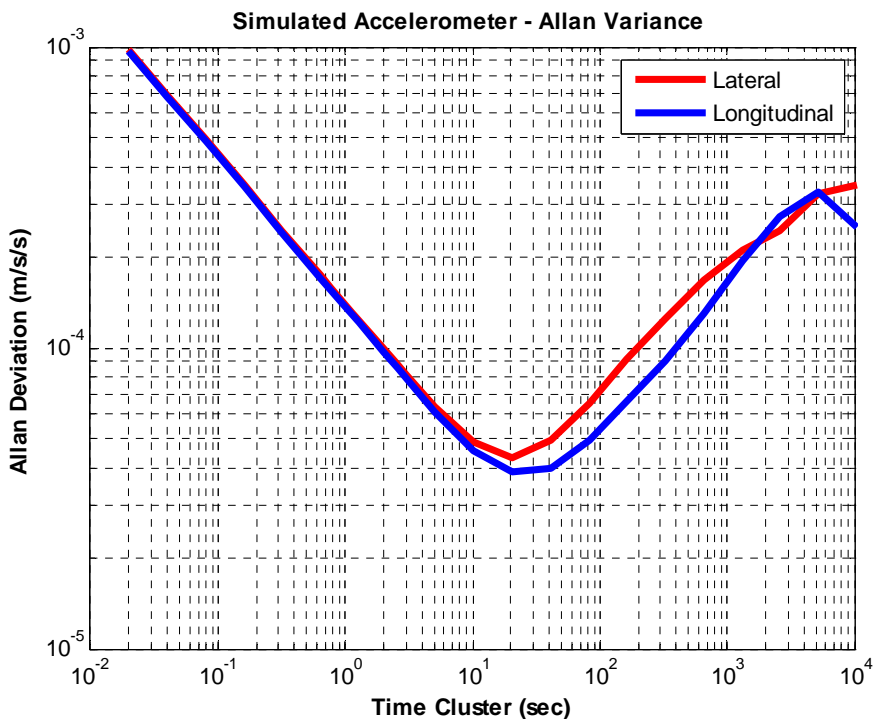


Figure 5.10: Allan deviation plot of the production accelerometers

Finally, the summarized noise parameters are presented in Table 5.1.

Table 5.1: Identified noise parameters using Allan variance

Sensor	Random Walk	Gauss-Markov	
	Noise PSD	Gauss-Markov Noise STD	Correlation Time
Lateral Accel.	$1.39e-4 \text{ m/s}^2 / \sqrt{\text{Hz}}$	$5.39e-4 \text{ m/s}^2$	4073 s
Longitudinal Accel.	$1.36e-4 \text{ m/s}^2 / \sqrt{\text{Hz}}$	$4.79e-4 \text{ m/s}^2$	3852 s
Vertical Gyro.	$140.04 \text{ deg/h} / \sqrt{\text{Hz}}$	$300 \text{ deg/h}$	2900 s

### 5.2.3 Filtering raw wheel speed sensor outputs

As discussed in the previous chapter, the wheel speed information is actually not measured directly. Instead, the wheel sensors actually accumulate the number of detected “counts” as the wheels rotate. For the vehicle used here, there are approximately 50 counts per revolution. The wheel speed is obtained by differentiating consecutive accumulated wheel counts. The free rolling radius of tire can be computed from the tire parameters. The 2009 GMC Acadia has P255/65 R18 tires, hence the free rolling radius is (Jazar 2008):

$$R = 255 \times 0.65 + 18 \times 25.4 / 2 = 394 \text{ mm} \quad 5.1$$

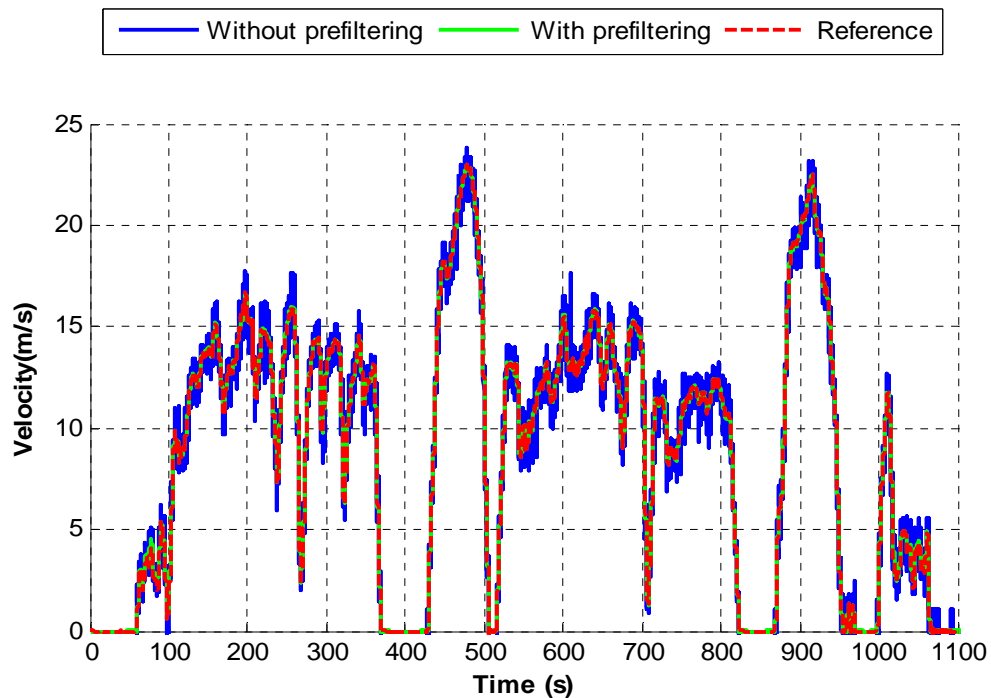
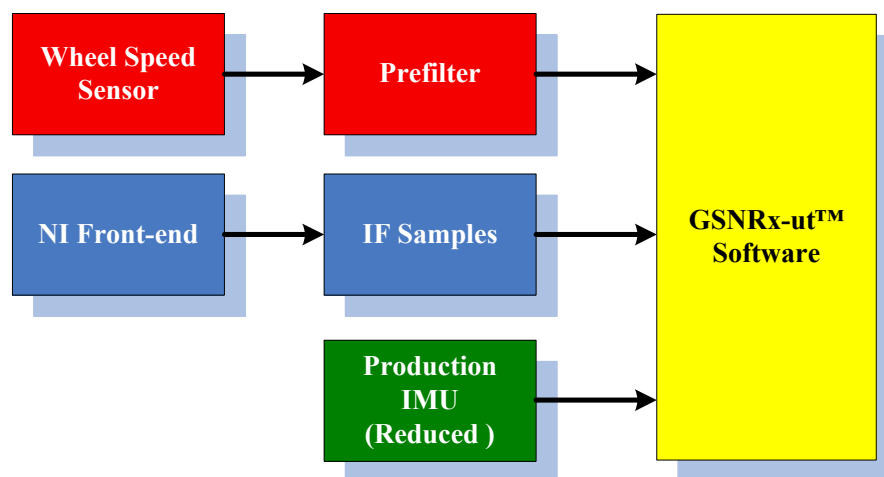


Figure 5.11: Filtered velocity from wheel speed sensor

Because the outputs of a wheel speed sensor are often corrupted by slips and noise, unrealistic wheel speed estimates must be removed. To this end, an initial threshold of 1000 counts/sec (equivalent to 178 km/h) was used. The computed wheel velocity was then filtered by a second-order Butterworth low pass filter to limit the noise effect. The cut-off frequency for this filter was 2.5 Hz. The filtered wheel speed is shown in Figure 5.11. The red line in this figure represents the longitudinal velocity in the body frame generated by the reference solution. Without pre-filtering, there are many spikes as shown with the blue line. These spikes mainly result from the longitudinal slips and the inaccurate relative time recorded between two consecutive samples. It is also noted that small differences also exist between the reference solution and the filtered wheel speed due to the tire radius variations during the test.

#### *5.2.4 Data processing summary*

The post mission processing procedure of ultra-tight integration of GPS and vehicle sensor is summarized in Figure 5.12.



**Figure 5.12: Block diagram of data processing**

The production IMU measurements, IF samples from the NI front-end and the filtered velocity from the wheel speed sensor are used as inputs into a modified version of the GSNRx-ut™ ultra-tight software GNSS receiver. The modifications were necessary to include a reduced IMU instead of a full IMU and to use the wheel speed data. Details about the algorithm implementation were introduced in Chapter 4.

### **5.3 Data Analysis Strategies**

The analysis of the processed results is performed in both the tracking domain and navigation domain. In the tracking domain, the Phase Lock Indicator (PLI) is used to evaluate the receiver's carrier phase tracking ability. In the navigation domain, the RMS position, velocity and attitude error are used to assess the performance of the navigation solution. Those performance parameters are compared between different receiver architectures including the standard GPS receiver (without attitude information) and the ultra-tightly coupled GPS receiver. Besides, the performance of the integrated system with different grades of IMUs and with full and reduced IMU configurations is analyzed. Finally, the contribution of the wheel speed sensor and non-holonomic constraints is assessed.

#### **Tracking Domain Analysis**

The PLI is a metric of carrier phase tracking performance generated internal to the software receiver. The phase lock indicator (PLI) is calculated as described by Van Dierendonck (1996), and provides an approximate measure of the quality of the phase lock. A value of +1 indicates perfect phase lock, while a value of -1 indicates worse-case

performance. To compare the performance of the various receiver architectures at the tracking level, the values of the phase lock indicators as a function of measured carrier to noise-density ratio ( $C/N_0$ ) are used. In addition, the tracked Doppler of the incoming signals is used to illustrate the line of sight dynamics of different satellites. Comparison between the Doppler and PLI would give an idea of the impact of dynamics on the carrier phase tracking. The estimated  $C/N_0$  that indicates the received signal quality is used for performance comparison between different operational environments and different IMUs. It is also noted that since a relatively high quality oscillator was used the impact of the oscillator on the carrier tracking performance was ignored in this thesis.

### **Navigation Domain Analysis**

For the navigation level analysis, the position, velocity and attitude accuracy are compared using different receiver architectures with different sensor configurations. In order to evaluate the benefits of non-holonomic constraints and wheel speed sensor derived velocity updates, the integrated navigation filter was updated using the following:

- wheel speed sensor velocity,
- lateral velocity constraint,
- vertical constraint,
- 2D velocity constraints (i.e., non-holonomic constraints), and
- 3D velocity updates (i.e., non-holonomic constraints and wheel speed sensor velocity).

## 5.4 Open sky test results

In this section, the results of the open sky test are summarized and analyzed in both the tracking and navigation domain.

### 5.4.1 Tracking domain

First analyzed is the tracking performance with different receiver architectures. The Doppler, PLI and obtained  $CN_0$  will be compared with high elevation and low elevation satellites.

#### Standard GPS receiver Vs Ultra-tight GPS/Full IMU

To begin the analysis, the tracking performance of a high elevation angle satellite is used. The elevation angle of PRN 20 is about 60 deg meaning the vehicle dynamics will have relatively low influence on the received Doppler frequency. As such, the Doppler variation for this satellite is relatively small, as shown in Figure 5.13 (top plot). The middle plot in the figure also clearly illustrates the advantages of ultra-tight integration of GPS and full HG1700 and Crista IMU (denoted as “UT-Full HG1700” and “UT-Full Crista”) relative to a standard receiver for carrier phase tracking. The reduced value of PLI during the periods 100 to 200 s and 550 to 550 s indicates signal degradation due to trees. It is noted that for the Crista IMU the receiver was initialized by the standard tracking mode for about 150 s. The initial drop of PLI values expressed by the blue curve shows the effect of this procedure. After initialization, the performance of the system with the Crista IMU is similar to that of the HG1700, which is consistent with results presented in Petovello et al (2008) and O’Driscoll et al (2008). The mean and standard deviation

of PLI as a function of  $C/N_0$  is shown in Figure 5.14 with different receiver architectures and inertial sensors. It is clear that the ultra-tight GPS receiver outperforms the standard receiver even when the Crista MEMS IMU is used. It is emphasized that the carrier phase tracking performance is not significantly influenced when low quality MEMS sensors are used. This is consistent with the results shown in Petovello et al (2008) and O’Driscoll et al (2008). The reason may be that the accuracy of the computed Doppler and code phase used to update the NCOs does not degrade noticeably when the Crista IMU is used. Furthermore, the line of sight dynamics induced by the MEMS IMU system error contributes little to the channel filter performance.

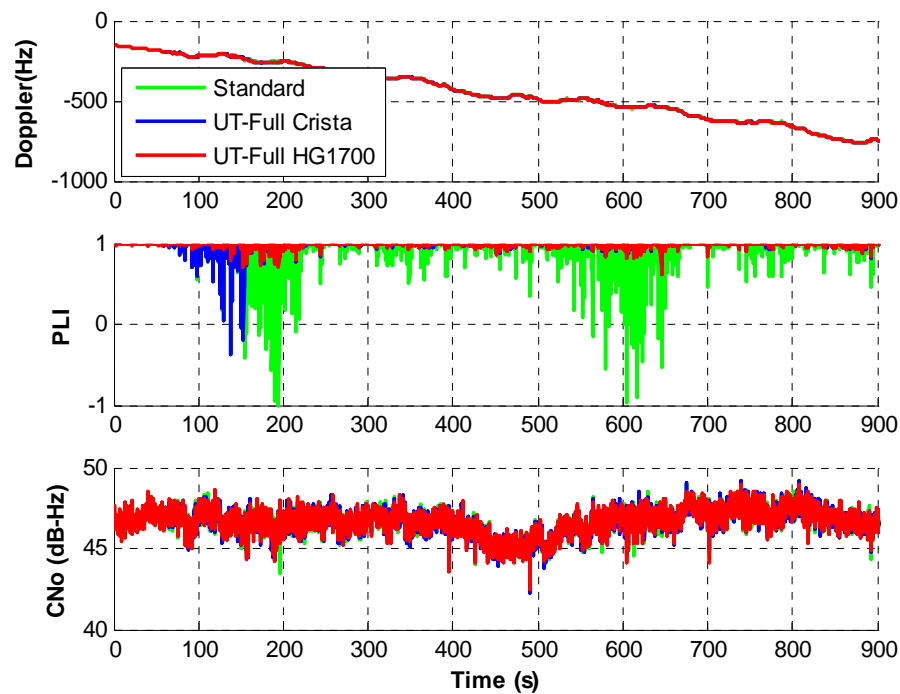


**Figure 5.13: PRN 20 Tracking results**

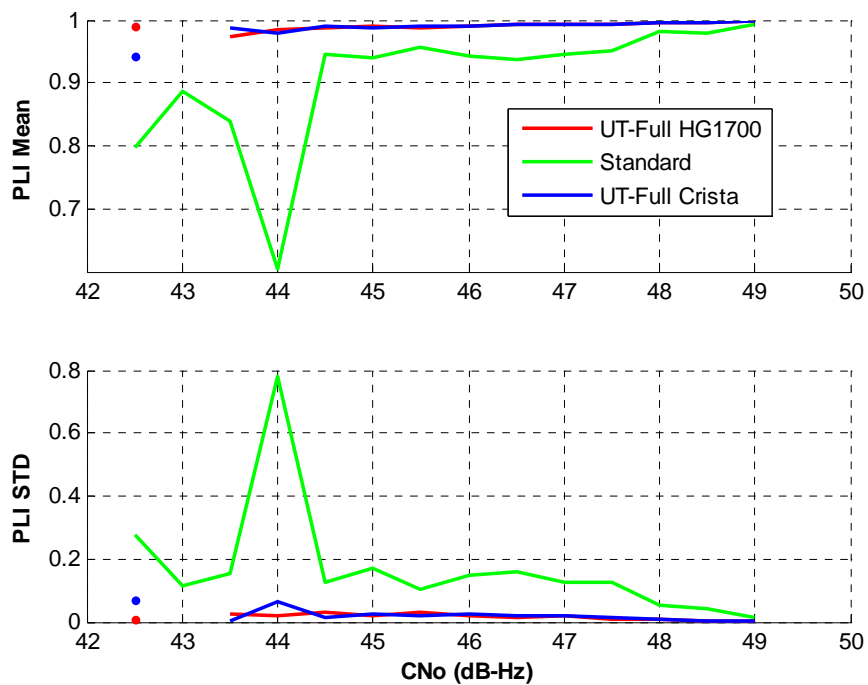


Figure 5.14: Mean and standard deviation of PLI as a function of  $C/N_0$  for PRN 20

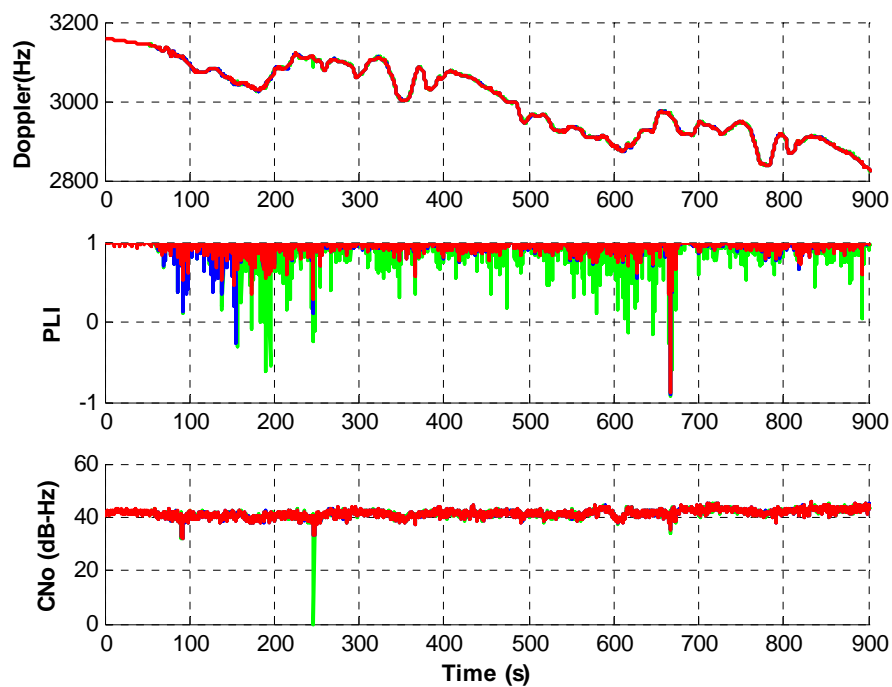


Figure 5.15: PRN 16 Tracking results

For comparison with the above, results for PRN 16 (elevation angle about 15 degrees) are shown in Figure 5.15. Because of the lower satellite elevation, the user motion induces larger Doppler variations than for PRN 20 (Figure 5.13). Nevertheless, the mean and standard deviations of the PLI values yield the same conclusions as for PRN 20. Figure 5.16 shows the PLI values as a function of  $C/N_0$  for PRN 16. Again, both ultra-tight configurations show improved performance, if only minimal in this environment. Also, the tracking performance using Crista IMU is similar to that when using the HG1700, as explained above.

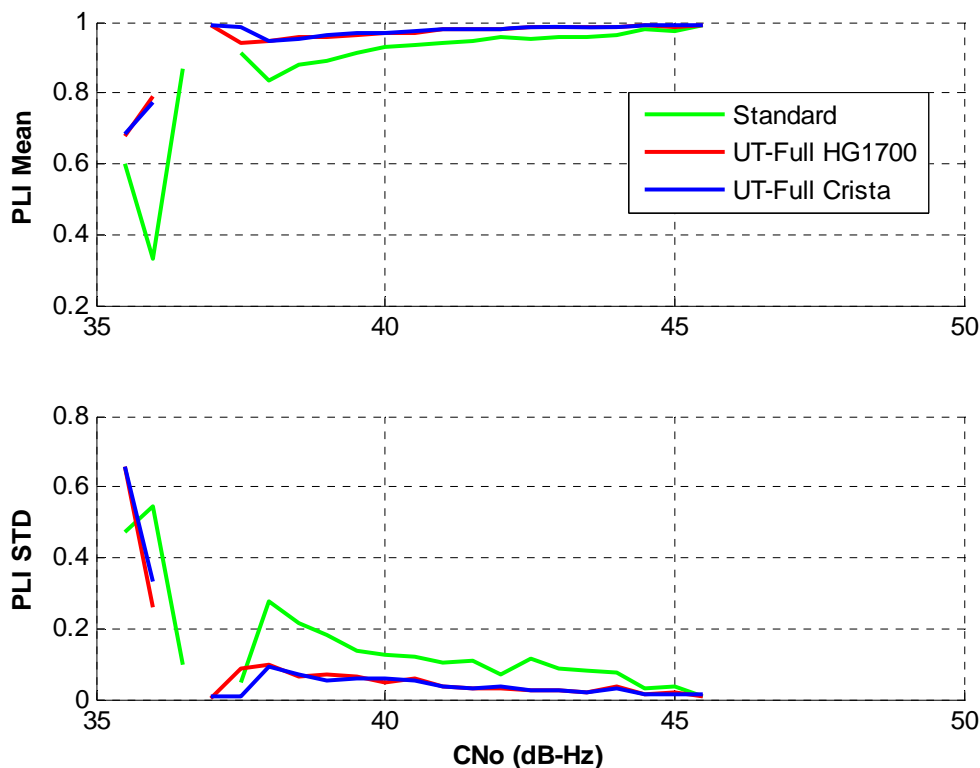


Figure 5.16: Mean and standard deviation of PLI as a function of  $C/N_0$  for PRN 16

### Ultra-tight GPS/Full IMUs Vs Ultra-tight GPS/Reduced IMUs

Having assessed the performance of the ultra-tight integration with full IMUs, focus is now on the integration with the reduced IMU. Figure 5.17 and Figure 5.18 show the mean and standard deviation of PLI values as a function of  $C/N_0$  for different receiver architectures and with different inertial sensors. Similar to the full IMU case, the ultra-tight GPS receiver has better carrier tracking performance compared with the standard receiver even when reduced MEMS sensors are used. Besides, there is no noticeable carrier tracking performance degradation when using reduced sensor sets. The reason is similar to full MEMS IMU case explained previously. Furthermore, it is noted that the value of line of sight residual acceleration process noise using reduced IMUs should be relatively larger to reflect the error induced by the reduced inertial system. However, it is noted that the impact of the error resulting from the reduced system on the tracking loops is still very small.

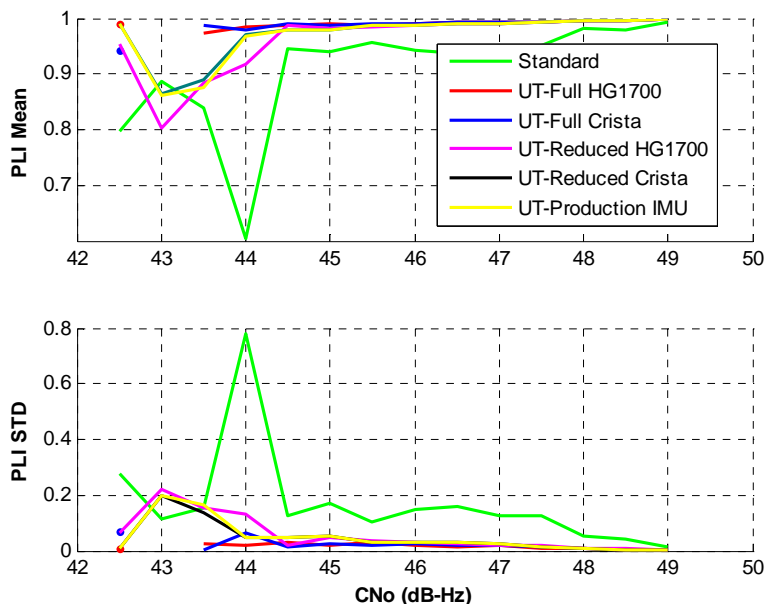
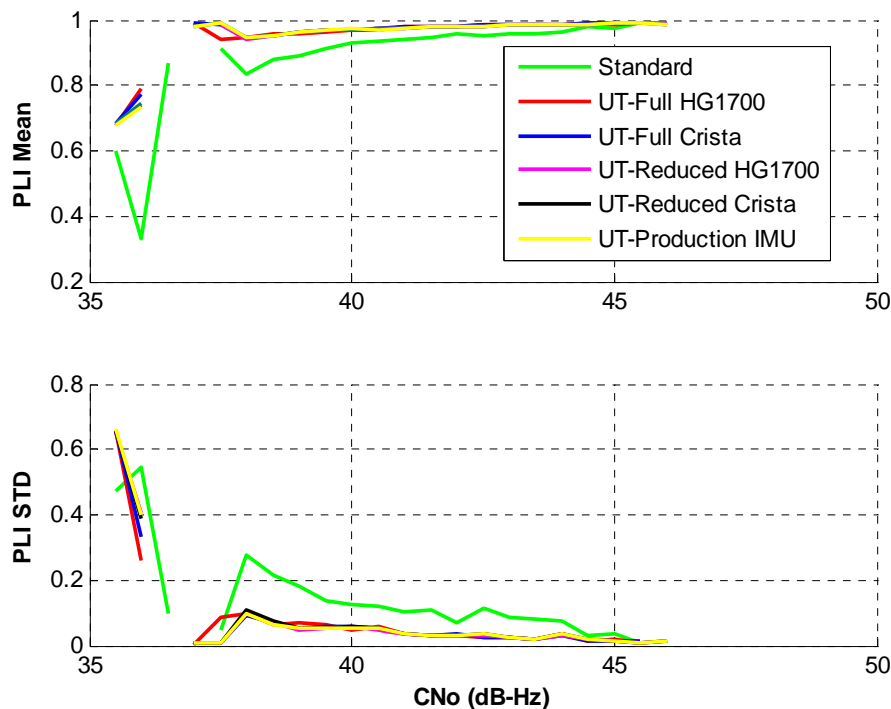


Figure 5.17: Mean and standard deviation of PLI as a function of  $C/N_0$  for PRN 20



**Figure 5.18: Mean and standard deviation of PLI as a function of  $C/N_0$  for PRN 16**

### Ultra-tight GPS/Reduced IMUs with Three-Dimensional Velocity Updates

Finally, the performance of the ultra-tight integration of reduced IMUs when three-dimensional velocity updates are used is analyzed. Figure 5.19 and Figure 5.20 show the mean and standard deviation of PLI values as a function of  $C/N_0$  with and without 3D velocity update (denoted as “3D”). The two figures clearly indicate that the contribution of the 3D velocity updates to the carrier phase tracking performance improvement is minimal. The three different reduced IMU systems with different sensor qualities have nearly the same performance. Therefore, for the data analyzed here the quality and sensor configurations play a minor roll in the tracking performance for the ultra-tight receiver. However, in the navigation domain, different sensors indeed perform differently as shown below.

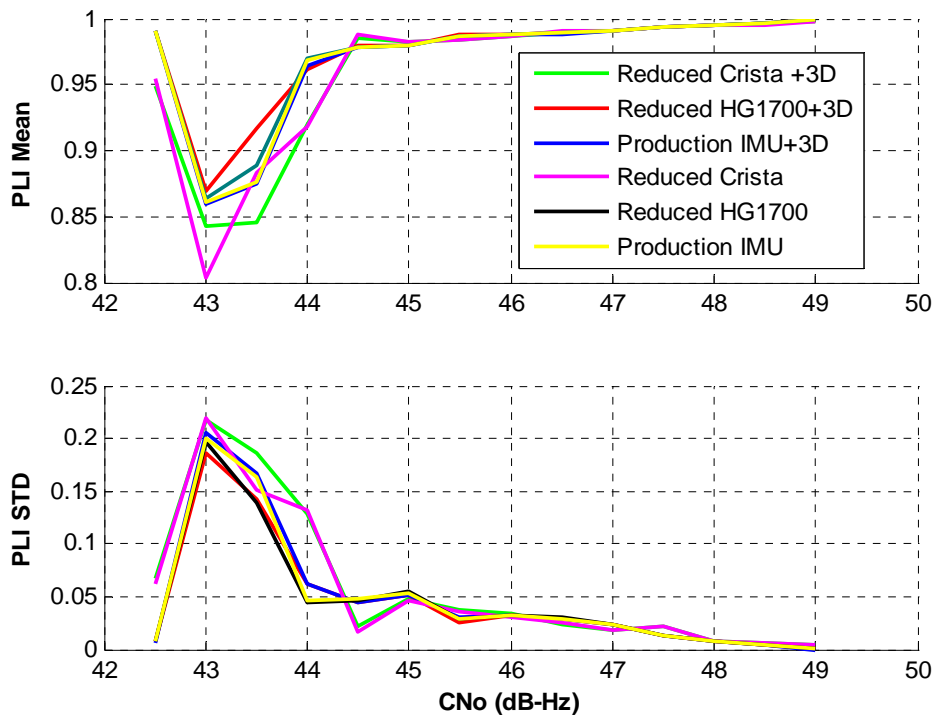


Figure 5.19: Mean and standard deviation of PLI as a function of  $C/N_0$  for PRN 20

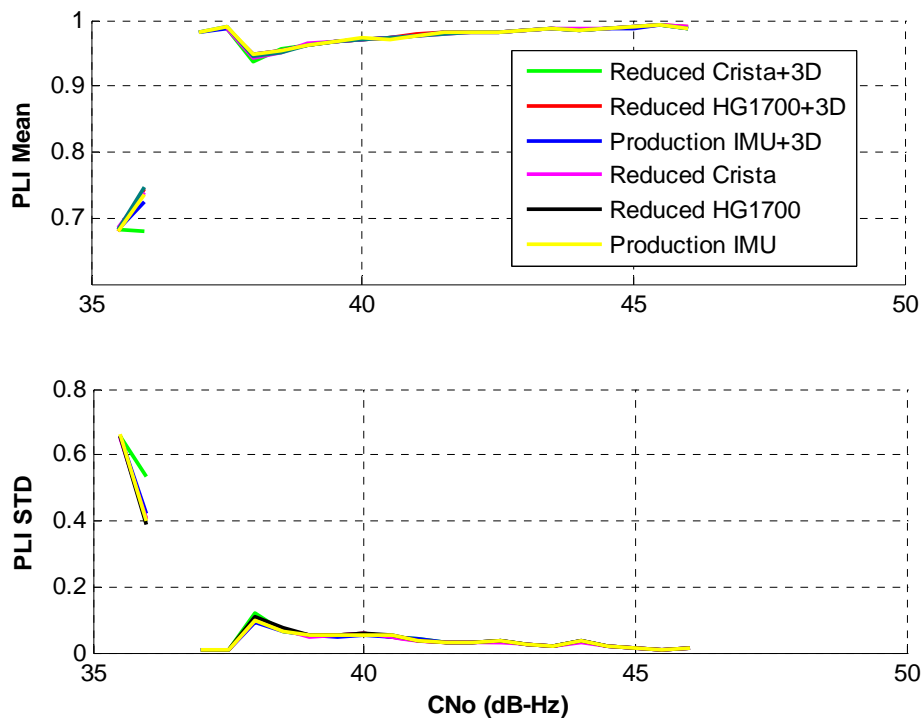


Figure 5.20: Mean and standard deviation of PLI as a function of  $C/N_0$  for PRN 16

### 5.4.2 Navigation domain

In the navigation domain, the analysis focused on the position, velocity and attitude accuracy of the ultra-tight GPS receiver with different sensor configurations. The reference solution is generated from the DGPS/INS loose integration.

#### Reference solution

The velocity and attitude plots are shown in Figure 5.21 and Figure 5.22. The maximum velocity is round 20 m/s and the vehicle's pitch and roll were within five degrees. Figure 5.23 illustrates the PDOP and satellite number during the computation of the reference solution. It is noted that there is still some foliage between 200 to 400 seconds.

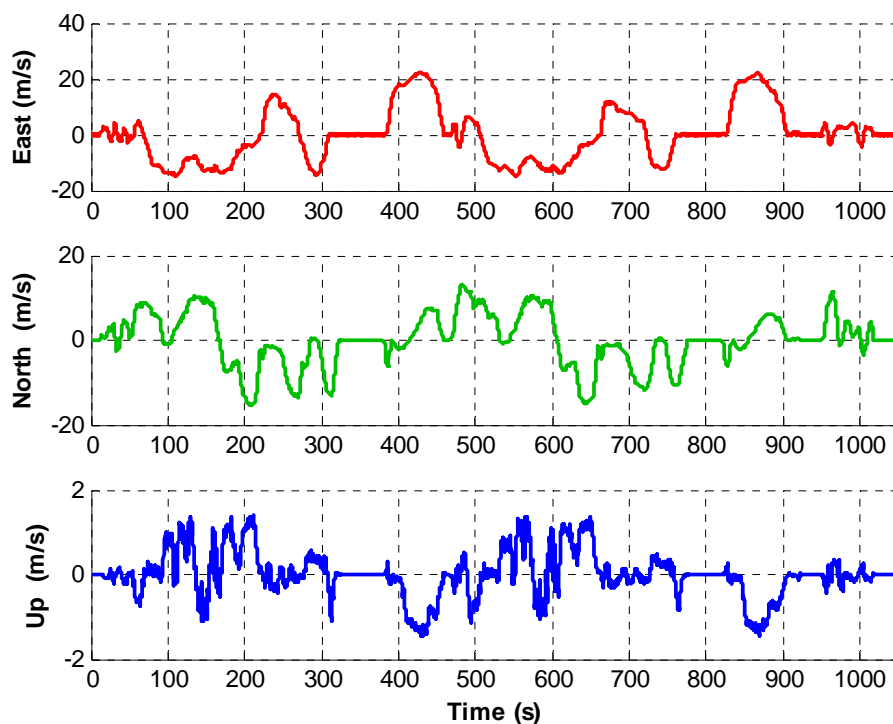


Figure 5.21: Reference velocity plots of the open sky test

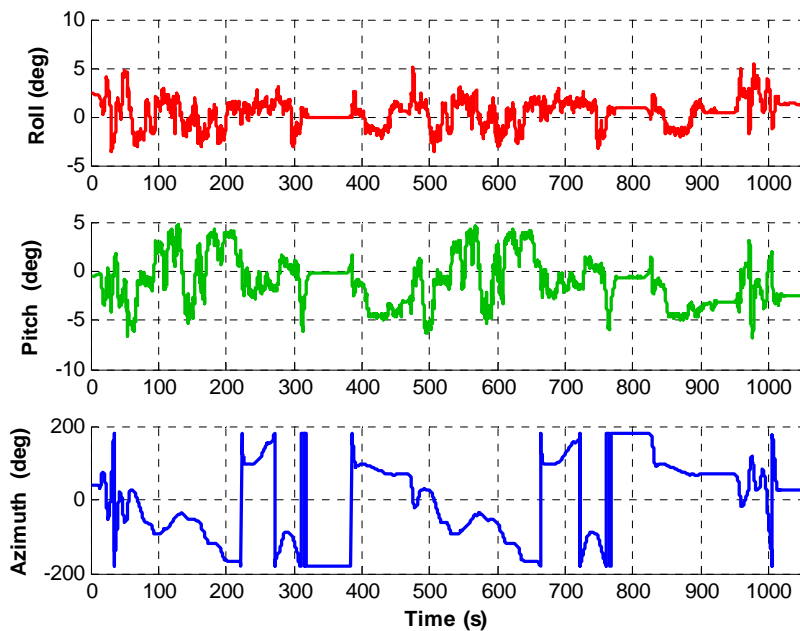


Figure 5.22: Reference attitude plots of the open sky test

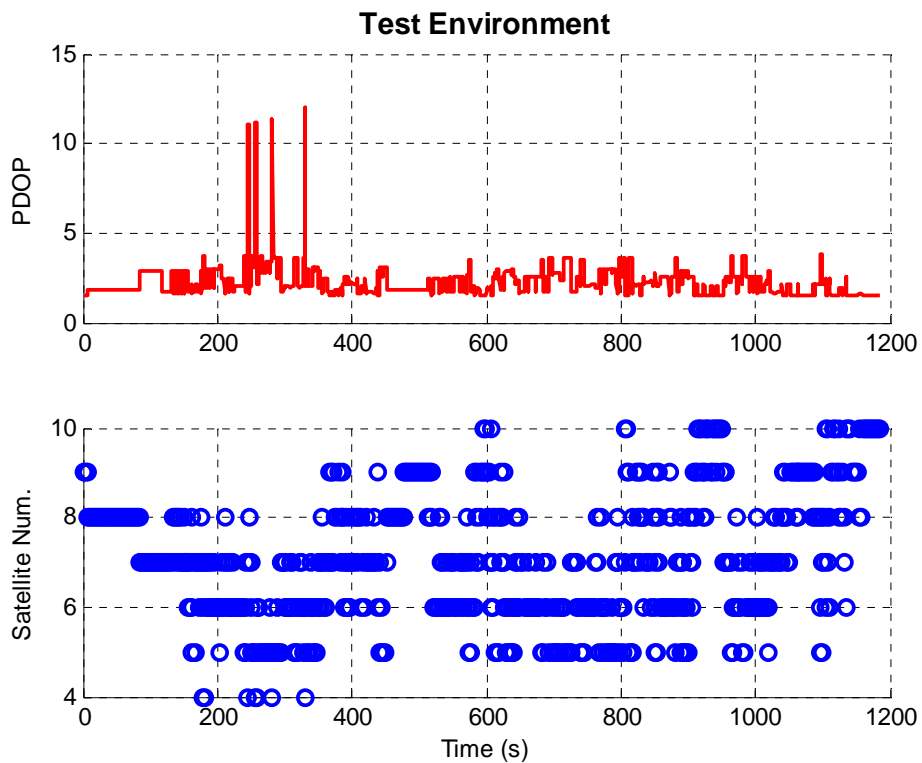
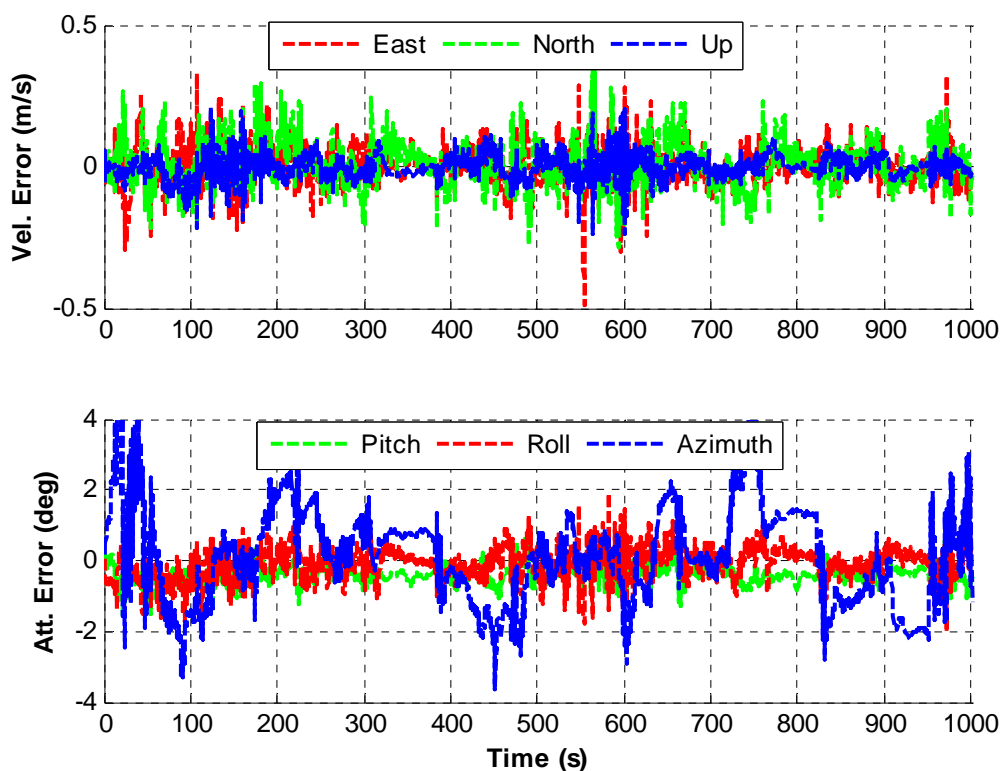


Figure 5.23: PDOP and satellite number plots of the open sky test

### Full Crista IMU

Figure 5.24 shows the velocity and attitude errors when using the full Crsita IMU as a function of time without any aiding information. The RMS velocity and attitude errors are summarized in Table 5.2.



**Figure 5.24: Velocity and attitude error plots for full Crista**

In order to limit the errors induced by the low quality MEMS IMU, Zero Velocity Updates (ZUPT) and 3D velocity updates are also used. Although this additional information has minimal effect on the tracking performance, it noticeably improves the velocity and attitude estimates. As clearly shown in Figure 5.25, ZUPT decreases velocity errors when the vehicle is static. Since a wheel speed sensor is used, the vehicle static

condition can be identified by verifying the wheel speed sensor outputs. The outputs are exactly zero when the vehicle is stopped. Besides, the wheel speed sensor and non-holonomic constraints derived 3D velocity are also used to update the integration filter.

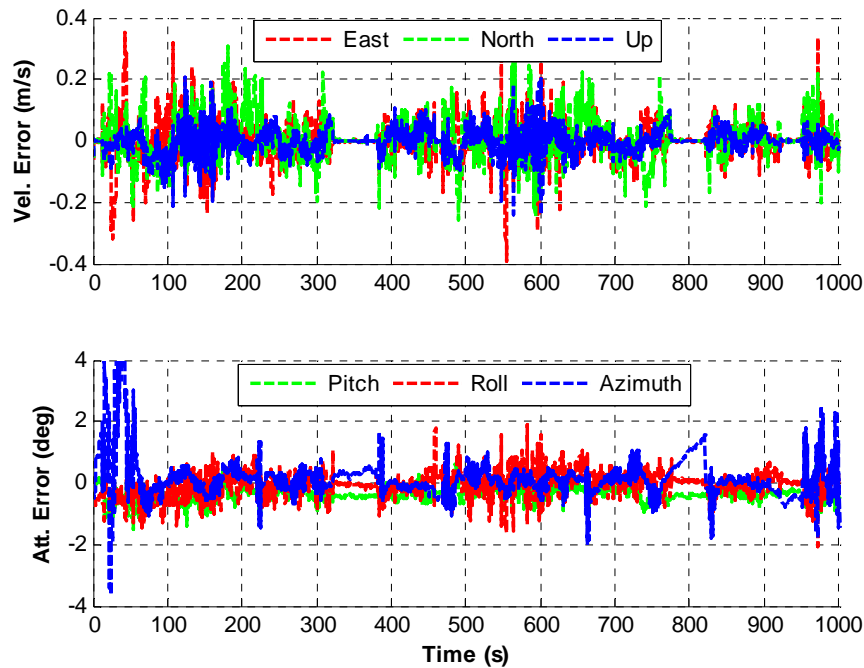


**Figure 5.25: Velocity and attitude error plots for full Crista+3D**

In order to analyze the benefits of the 3D velocity updates, the integration filter is updated using the wheel speed only (denoted as “WSS”), lateral constraint (denoted as “lateral”), vertical constraint (denoted as “vertical”), combination of lateral and wheel speed (denoted as “L+WSS”), non-holonomic constraints (“2D”) and finally 3D velocity updates. The results are listed in Table 5.2.

As shown in the table, when only the wheel speed sensor derived velocity is fed into the integration filter, the major improvement occurs in the pitch and azimuth estimates. This can be explained by the following:

$$\delta Z_{3D} = \begin{bmatrix} 0_{cons} \\ \hat{v}_{WSS} \\ 0_{cons} \end{bmatrix} - \begin{bmatrix} \hat{v}_x^b \\ \hat{v}_y^b \\ \hat{v}_z^b \end{bmatrix} = R_l^b \delta v^l + \begin{bmatrix} 0 & -v_z^b & v_y^b \\ v_z^b & 0 & -v_x^b \\ -v_y^b & v_x^b & 0 \end{bmatrix} \begin{bmatrix} \delta\theta \\ \delta\phi \\ \delta\psi \end{bmatrix} \quad 5.2$$

The wheel speed sensor derived velocity is related with  $\delta\theta$  and  $\delta\psi$  by  $v_z^b$  and  $-v_x^b$  respectively. Correspondingly, the pitch and azimuth estimates can be improved through the wheel speed sensor derived velocity updates.

It is also noted that there is no velocity improvement because the integration filter weighs more the GPS velocity in the open sky scenario. In other words, the system's velocity accuracy mainly depends on the GPS velocity in this case.

**Table 5.2: Velocity and attitude error for full Crista IMU**

Constraint/ Sensors	Velocity (m/s)			Attitude (deg)		
	Ve	Vn	Vu	Roll	Pitch	Azimuth
<b>None</b>	0.06	0.07	0.04	0.46	0.42	1.41
<b>WSS</b>	0.06	0.07	0.04	0.42	0.40	1.26
<b>Lateral</b>	0.06	0.07	0.04	0.44	0.40	0.83
<b>Vertical</b>	0.06	0.07	0.03	0.44	0.42	1.41
<b>L+WSS</b>	0.06	0.06	0.04	0.45	0.38	0.77
<b>2D</b>	0.06	0.07	0.03	0.42	0.39	0.83
<b>3D</b>	0.06	0.06	0.03	0.42	0.37	0.77

If a lateral constraint is applied, the azimuth and roll can be improved. However, the azimuth improvement is relatively larger compared with that of the roll. This is because, with reference to Equation (5.2), the lateral velocity error is mainly related to azimuth by  $v_y^b$ . And in vehicle navigation applications,  $v_y^b$  indicates the longitudinal velocity, which is usually larger than the magnitude of  $v_z^b$ . Therefore, the lateral constraint has a relatively higher correlation with the azimuth error state. Thus, the lateral constraint mainly improves the azimuth estimates.

Vertical constraints have only a minor contribution to the attitude error as shown in Table 5.2. The reason is the choice of the measurement noise. The noise standard deviations of these velocity updates are selected pessimistically. The selection criterion is that the final accuracy of the navigation solution does not decrease when either the lateral, vertical or longitudinal velocity updates are used. Therefore, the vertical constraint is chosen to be relatively larger as shown in Table 5.3 so that it has no negative effect on the navigation solution. This is important since any error in the navigation solution would feed into the tracking filter which in turn influences the GPS measurement generation.

**Table 5.3: Standard Deviations of three-dimensional velocity updates**

Constraint	Noise STD (m/s)		
	Lateral	Longitudinal	Vertical
<b>3D</b>	1.0	1.0	3.0

Since a vertical constraint has minimal influence on the final navigation solution, the “L+WSS” updates have similar performance as the 3D velocity updates. Therefore, in an open sky environment, only the lateral constraint and the wheel speed sensor are sufficient to update the integration filter without losing any benefits from non-holonomic constraints.

Finally, the RMS position errors of the system with and without 3D velocity updates are listed in Table 5.4. The 3D velocity slightly improves the east and north position estimates. The vertical position accuracy remains the same as that without 3D velocity updates. Therefore, in the open sky test, the contribution of 3D velocity updates to the positioning accuracy improvement is small compared with the attitude improvement.

**Table 5.4: RMS position errors for full Crista IMU**

Constraint	Position Error (m)		
	East	North	Up
<b>None</b>	1.08	1.26	3.38
<b>3D</b>	1.02	1.24	3.28

### **Reduced Crista IMU**

Having analyzed the performance of full Crista IMU, the navigation accuracy of the reduced Crista IMU is now evaluated. Figure 5.26 and Figure 5.27 shows the velocity and attitude errors with and without 3D velocity updates, respectively.

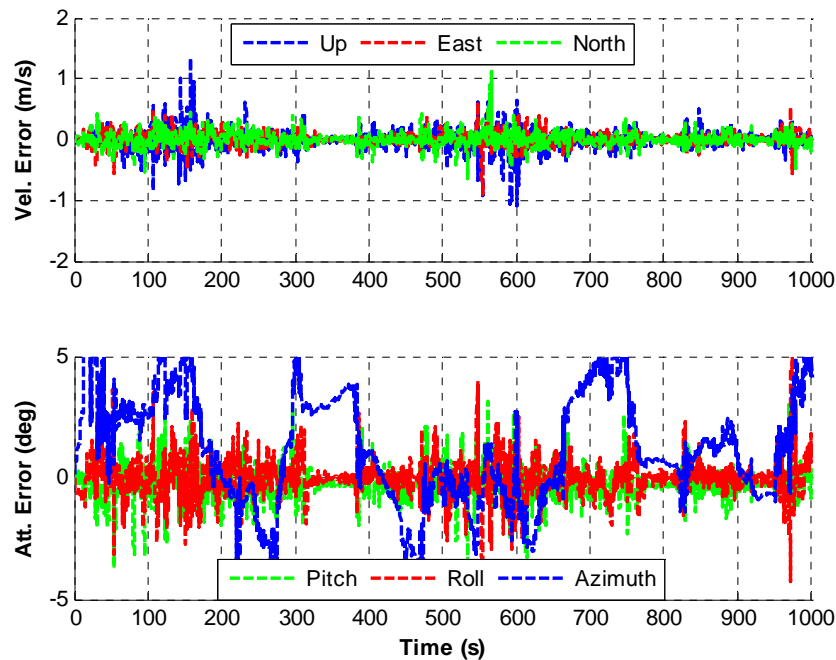


**Figure 5.26: Velocity and attitude error plots for reduced Crista**

Compared with the full Crista IMU, the accuracy deteriorates due to the reduced sensor configuration. This is because the velocity and attitude errors overflow into the entire state estimates, which can be explained by the system model of the integration filter. The pitch and roll errors are related to local terrain variations and vertical vehicle dynamics (primarily via the vehicle's suspension system). Terrain and vehicle suspension induced dynamics are modeled as white noise because the omitted sensors are replaced by the pseudo signals as explained in the previous chapter. Therefore, peaks in the pitch and roll errors can be explained by the un-modeled terrain and vehicle suspension induced dynamics. Those dynamics can be also expressed with other models, but this was beyond the scope of this work. For example, Sun (2008) applies first order Gauss-Markov process to model the local terrain.

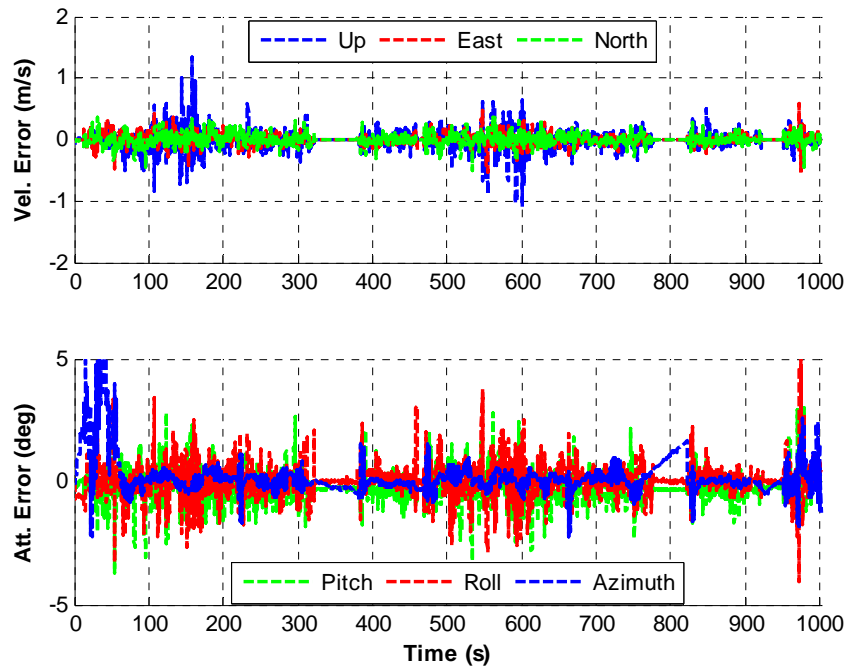


**Figure 5.27: Velocity and attitude error plots for reduced Crista + 3D**

Both velocity and attitude estimates can be improved when 3D velocity updates are used. The results are summarized in Table 5.5. Similar to the analysis of the full Crista case, the lateral and wheel speed sensor derived velocity updates have major influence on the navigation solution. The vertical constraint does not improve the velocity and attitude estimates and it even deteriorates the azimuth accuracy slightly because of the violation of the constraints. The RMS position errors of the system with and without 3D velocity updates are given in Table 5.6. As shown in this table, the 3D velocity updates improve the positioning accuracy in all the directions.

**Table 5.5: Velocity and attitude errors for reduced Crista IMU**

Constraint/Sensors	Velocity (m/s)			Attitude (deg)		
	Ve	Vn	Vu	Roll	Pitch	Azimuth
<b>None</b>	0.09	0.10	0.14	0.70	0.72	2.60
<b>WSS</b>	0.09	0.10	0.14	0.70	0.68	2.28
<b>Lateral</b>	0.09	0.09	0.14	0.65	0.70	0.85
<b>Vertical</b>	0.09	0.10	0.14	0.70	0.71	2.65
<b>L+WSS</b>	0.08	0.08	0.14	0.65	0.67	0.84
<b>2D</b>	0.08	0.08	0.14	0.65	0.69	0.85
<b>3D</b>	0.08	0.08	0.14	0.65	0.67	0.84

**Table 5.6: RMS position errors for reduced Crista IMU**

Constraint	Position Error (m)		
	East	North	Up
<b>None</b>	1.84	2.35	3.34
<b>3D</b>	1.21	1.38	3.22

### Production IMU

Similar results as with reduced Crista IMUs were obtained when the external production IMU was used. The production IMU is also a reduced IMU with two horizontal accelerometers and one vertical gyro. Furthermore, the production IMU has similar noise characteristics as that of the Crista IMU, as was shown in Table 4.1. The velocity and attitude errors with and without 3D velocity updates are shown in Figure 5.28 and Figure 5.29, respectively. The RMS velocity and attitude errors with different velocity updates are summarized in Table 5.7. Because the production IMU and Crista IMU are of similar quality, their positioning performance is also very similar. In addition, the vertical

constraint slightly improves the attitude estimates. However, compared with the wheel speed sensor and lateral constraints, its benefits are minimal. The position errors are given in Table 5.8.

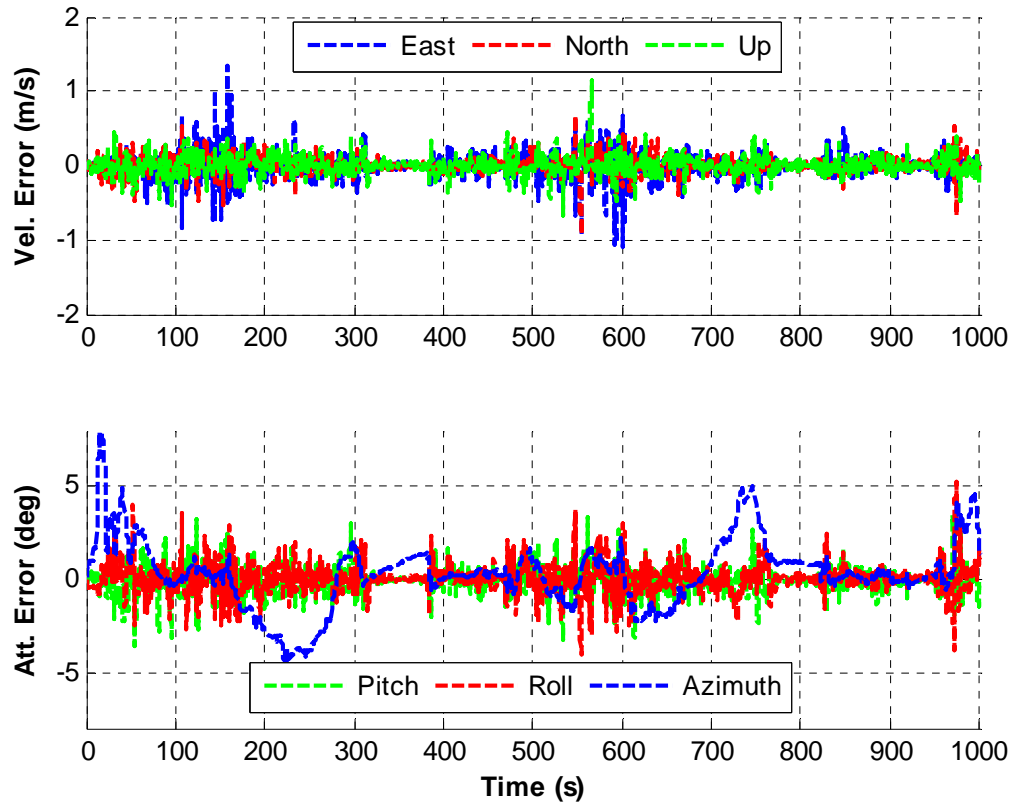


**Figure 5.28: Velocity and attitude errors plots for the production IMU**

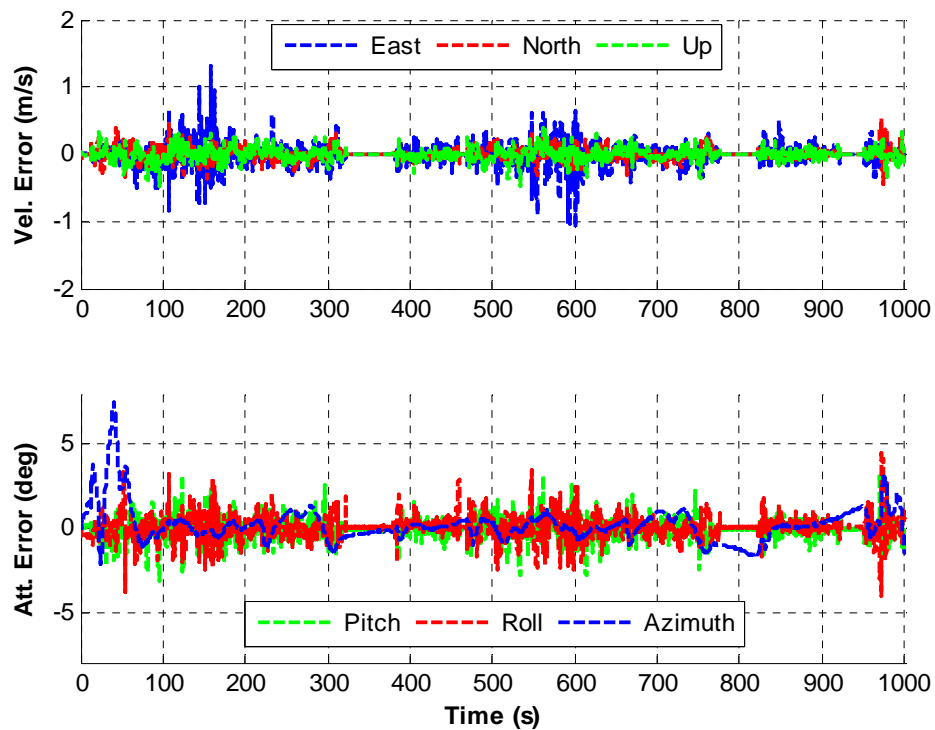


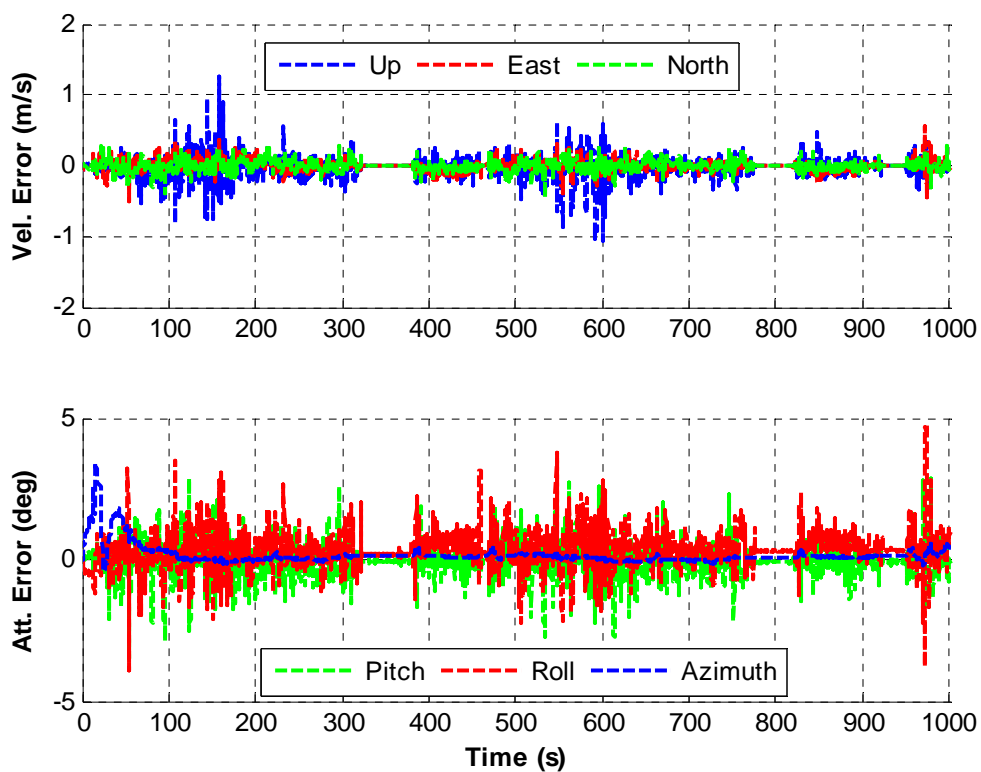
**Figure 5.29: Velocity and attitude error plots for the production IMU + 3D**

**Table 5.7: Velocity and attitude errors for the production IMU**

Constraint/Sensors	Velocity (m/s)			Attitude (deg)		
	$V_e$	$V_n$	$V_u$	Roll	Pitch	Azimuth
<b>None</b>	0.09	0.10	0.14	0.65	0.72	1.84
<b>WSS</b>	0.08	0.10	0.14	0.65	0.65	1.46
<b>Lateral</b>	0.09	0.10	0.14	0.61	0.71	1.09
<b>Vertical</b>	0.09	0.10	0.13	0.65	0.72	1.73
<b>L+WSS</b>	0.08	0.08	0.14	0.61	0.64	1.07
<b>2D</b>	0.09	0.09	0.14	0.61	0.71	1.09
<b>3D</b>	0.08	0.08	0.14	0.61	0.64	1.07

**Table 5.8: RMS position errors for the production IMU**

Constraint	Position Error (m)		
	East	North	Up
None	1.53	1.85	3.55
3D	1.35	1.19	3.37

**Figure 5.30: Velocity and attitude error plots for reduced HG1700**

### Reduced HG1700

The final step of the open sky analysis is to look at the results from the reduced HG1700.

To this end, Figure 5.30 shows the velocity and attitude errors as the function of time and the position errors are shown in Table 5.10. Compared with the reduced Crista and the

production IMU, the velocity accuracy is not improved by using higher grade accelerometers. The reason is that the velocity accuracy of the reduced system in the open sky scenario depends on the GPS velocity accuracy (Sun 2008). Furthermore, the roll and pitch accuracies remain at the same level as the reduced Crista and the production IMU. The reason has been explained previously and is because the pitch and roll estimates are related to the vehicle suspension and local terrain induced dynamics for the reduced sensor configuration and they cannot be well estimated until GPS and 3D velocity updates are available. Therefore, higher grade horizontal accelerometers and the vertical gyro make a limited contribution to the pitch and roll estimates. The pitch and roll estimates are related to vehicle dynamics, GPS and wheel speed sensor measurement accuracy. However, the reduced HG1700 has better azimuth accuracy. This is due to the higher quality vertical gyro used.

**Table 5.9: Velocity and attitude errors for reduced HG1700**

Constraints/Sensors		Velocity (m/s)			Attitude (deg)		
		V <sub>e</sub>	V <sub>n</sub>	V <sub>u</sub>	Roll	Pitch	Azimuth
None	<b>HG1700</b>	0.09	0.10	0.14	0.61	0.69	0.96
	<b>Crista</b>	0.09	0.10	0.14	0.70	0.72	2.60
	<b>Production</b>	0.09	0.10	0.14	0.65	0.72	1.84
3D	<b>HG1700</b>	0.08	0.08	0.14	0.58	0.65	0.39
	<b>Crista</b>	0.08	0.08	0.14	0.65	0.67	0.84
	<b>Production</b>	0.08	0.08	0.14	0.61	0.64	1.07

In summary, for reduced systems in an open sky environment, the velocity accuracy mainly depends on the accuracy of measurements used to update the integration filter. It cannot be improved by using high quality accelerometers because the reduced system induced attitude error limits the contribution of accelerometers. In addition, roll and pitch estimates are related to the vehicle dynamics and local terrain. High quality reduced IMU plays only a minimal role in the improvements of these estimates. Finally, the improved azimuth accuracy can be obtained by using a higher grade vertical gyro. According to the above conclusion, a reduced system with low quality accelerometers and high quality gyro is suggested to balance the system cost and navigation performance.

**Table 5.10: RMS position errors for reduced HG1700**

Constraint	Position Error (m)		
	East	North	Up
None	1.58	1.75	3.25
3D	1.37	1.01	3.07

For comparison purpose, the position and velocity errors of a standard GPS receiver are given in Table 5.11. The results show that the ultra-tight receiver performs slightly better in the open sky scenarios.

**Table 5.11: RMS Position and velocity errors for standard GPS**

Position (m)			Velocity (m/s)		
East	North	Up	East	North	Up
2.49	2.57	4.04	0.14	0.15	0.16

## 5.5 Foliage test results

Having confirmed the basic performance of the ultra-tight receiver for the open sky data, the analysis now shifts to the foliage test. To this end, a similar analysis strategy as above is used.

### 5.5.1 Tracking domain

The tracking domain analysis is also conducted using different receiver structures and different sensor configurations.

#### Standard GPS receiver Vs Ultra-tight GPS/Full IMU

First, the performance comparison between a standard GPS receiver and an ultra-tightly coupled GPS/full IMU is presented. Figure 5.31 shows the tracking results for PRN 4 (approximately 15 degrees elevation) which has a relatively low elevation angle. Therefore, compared with the results of PRN 23 (approximately 60 degrees elevation) shown in Figure 5.33, its tracked Doppler frequency is larger which indicates that it would suffer more from vehicle dynamics. The lower PLI values shown in the middle plots of Figure 5.31 and Figure 5.33 indicate that the incoming signals were shaded by trees. From the Doppler plot of both the high and low elevation angle cases, the ultra-tight GPS receiver outperforms the standard GPS receiver by avoiding false frequency lock and by providing better Doppler estimates. Also the ultra-tight GPS receiver has better  $C/N_0$  estimates. Figure 5.32 and Figure 5.34 show the mean and standard deviation of PLI values as a function of  $C/N_0$  for different receiver architectures. Ultra-tight GPS receiver has a larger improvement (higher PLI mean value and lower STD) for the tracking of

PRN 4 as compared to that of PRN 23. The reason is that the high elevation satellites do not experience much Doppler shift due to user motion and thus the ultra-tight receiver is of reduced benefit. Nevertheless, the improvement in carrier tracking is still very noticeable.

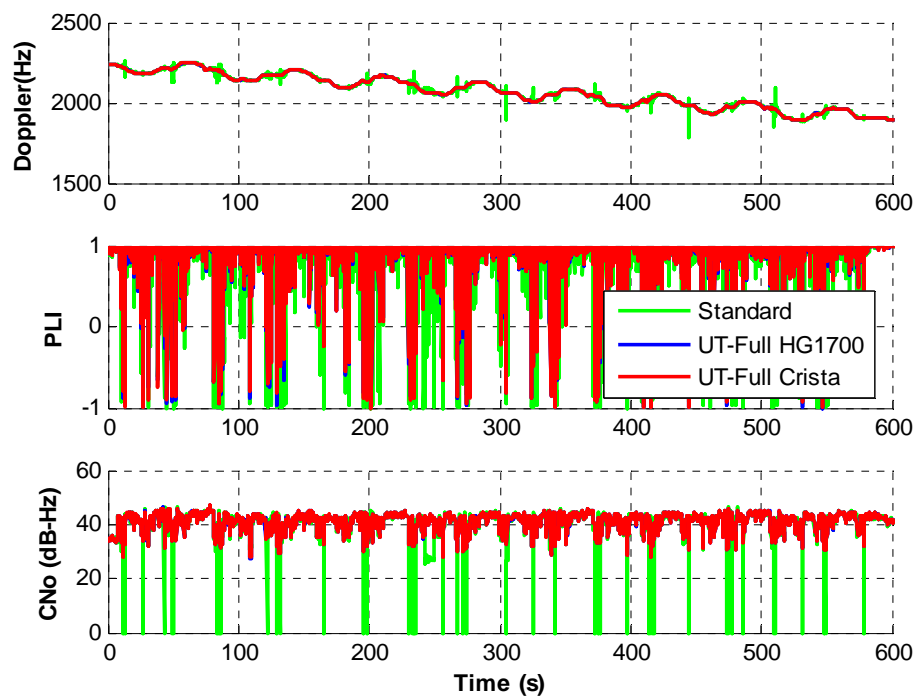


**Figure 5.31: Tracking performance of PRN 4**

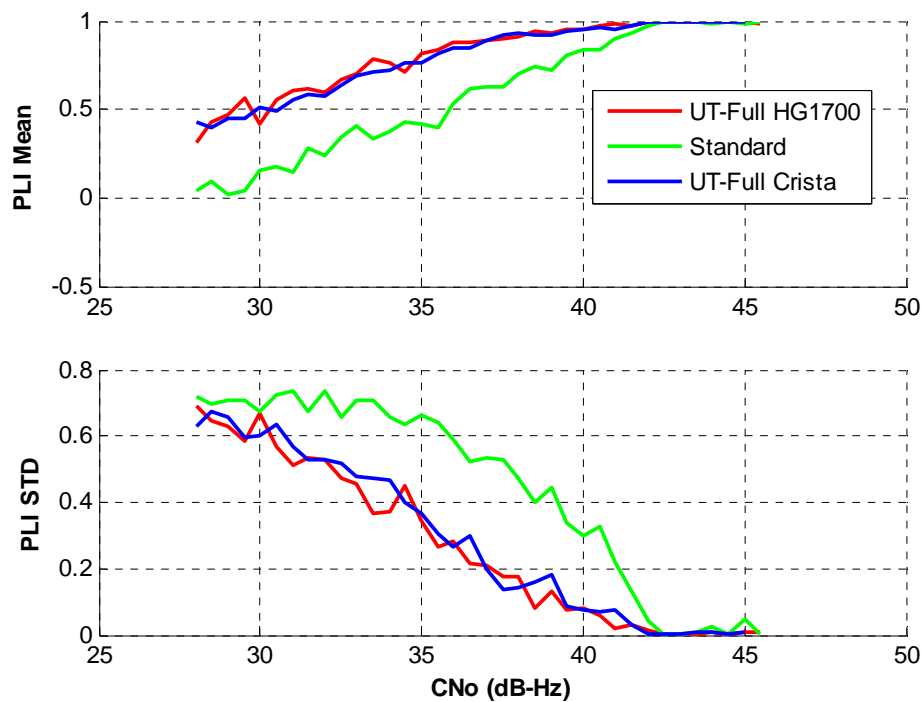


Figure 5.32: Mean and standard deviation of PLI as a function of  $C/N_0$  for PRN 4

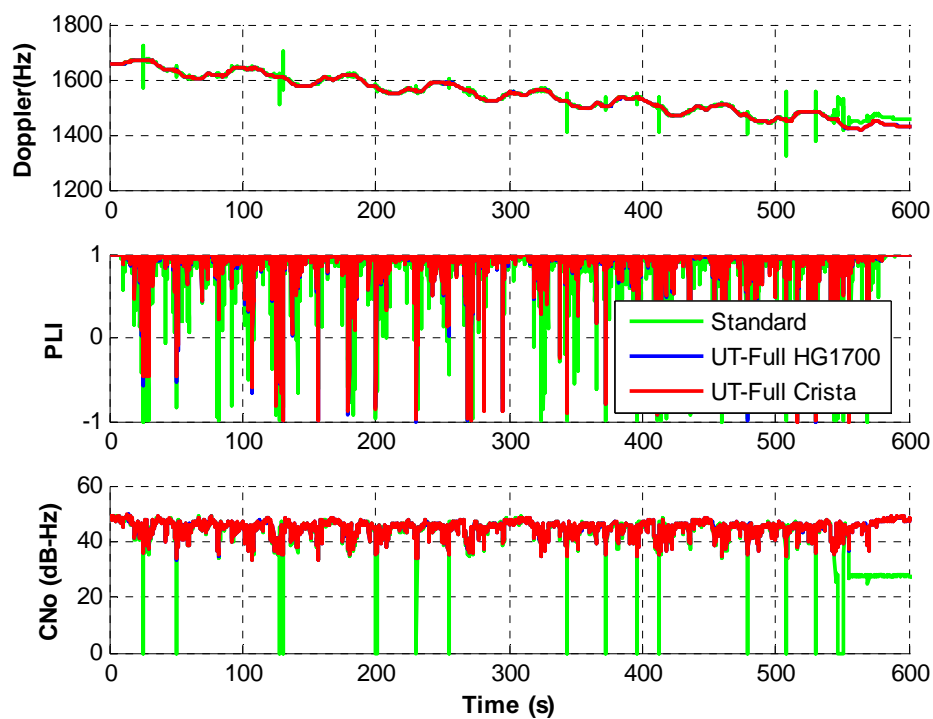
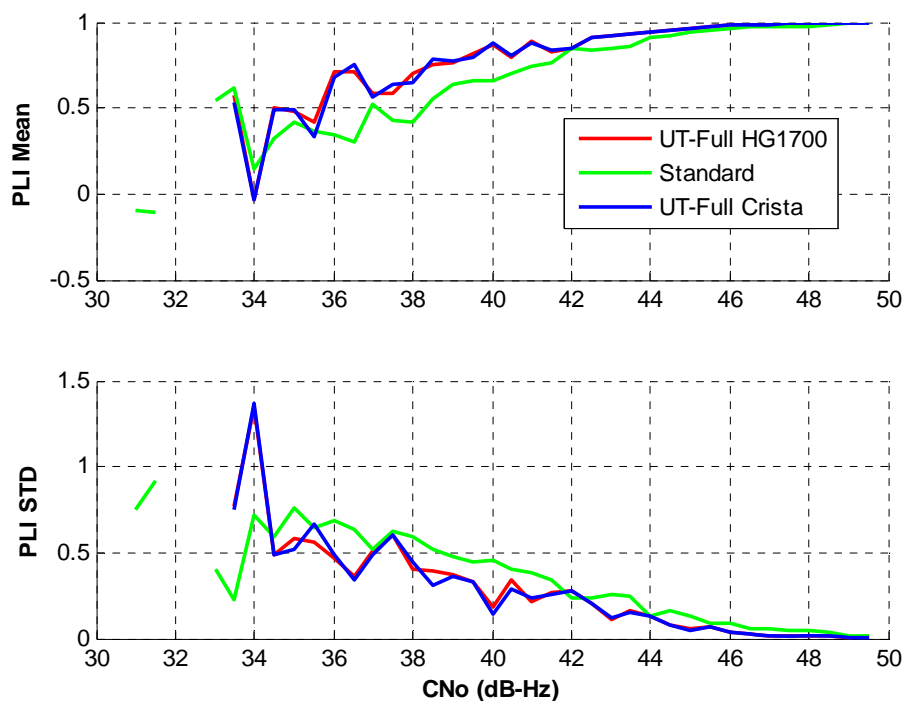


Figure 5.33: Tracking performance of PRN 23



**Figure 5.34: Mean and standard deviation of PLI as a function of  $C/N_0$  for PRN 23**

It is also noted that when the low cost Crista MEMS IMU is used for ultra-tight integration, tracking does not experience noticeable performance degradation due to the low quality of MEMS sensors. The reason may be that the computed Doppler and code phase from the integrated navigation solution using MEMS sensors that are used to update NCOs has a negligible accuracy deterioration even for the tracking of low satellites. Furthermore, similar to the open sky analysis, the line of sight dynamics induced by the MEMS system error still play a minimal roll in the performance of the channel filters.

### **Ultra-tight GPS/Full IMUs Vs Ultra-tight GPS/Reduced IMUs**

Having evaluated the ultra-tight integration of full IMUs, the performance of the integration of reduced IMUs is investigated here. The analysis is still conducted on both the high and low elevation angle satellites (PRN 23 and PRN 4 respectively). Figure 5.35 and Figure 5.36 show the mean and standard deviation of PLI values as a function of  $C/N_0$  for different receiver architectures and with different sensors. Similar to the full IMU case, the ultra-tight GPS receiver has better carrier tracking performance compared to that of the standard GPS receiver even when low cost reduced MEMS sensors are used. In addition, there is no noticeable tracking performance degradation when the reduced sensor sets are used. The reason has been explained for the full MEMS case. It is noted that the value of line of sight residual acceleration process noise when using reduced IMUs should be selected to be larger to reflect the line of sight dynamics resulting from the reduced system. Furthermore, for the high elevation angle satellite (PRN 23), the ultra-tight receiver has nearly the same performance as the standard receiver. The reason has been explained in the previous section.

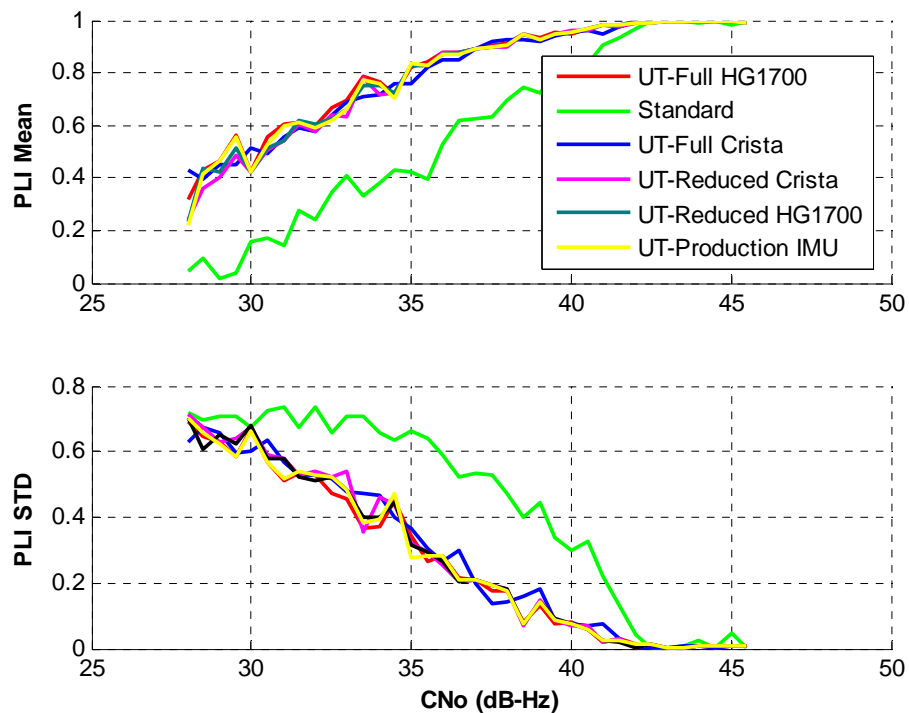


Figure 5.35: Mean and standard deviation of PLI as a function of  $C/N_0$  for PRN 4

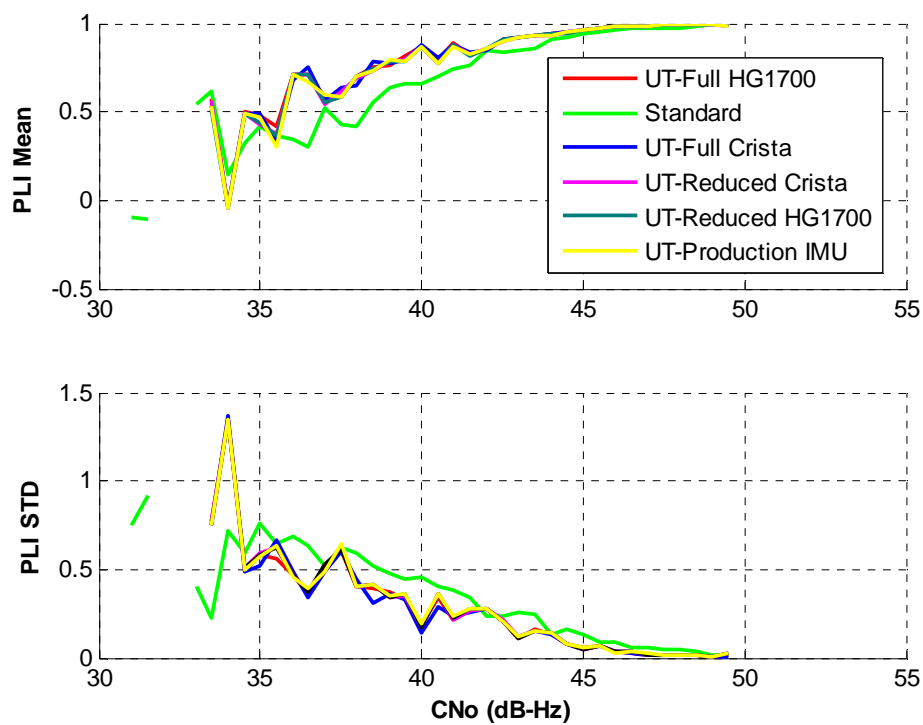
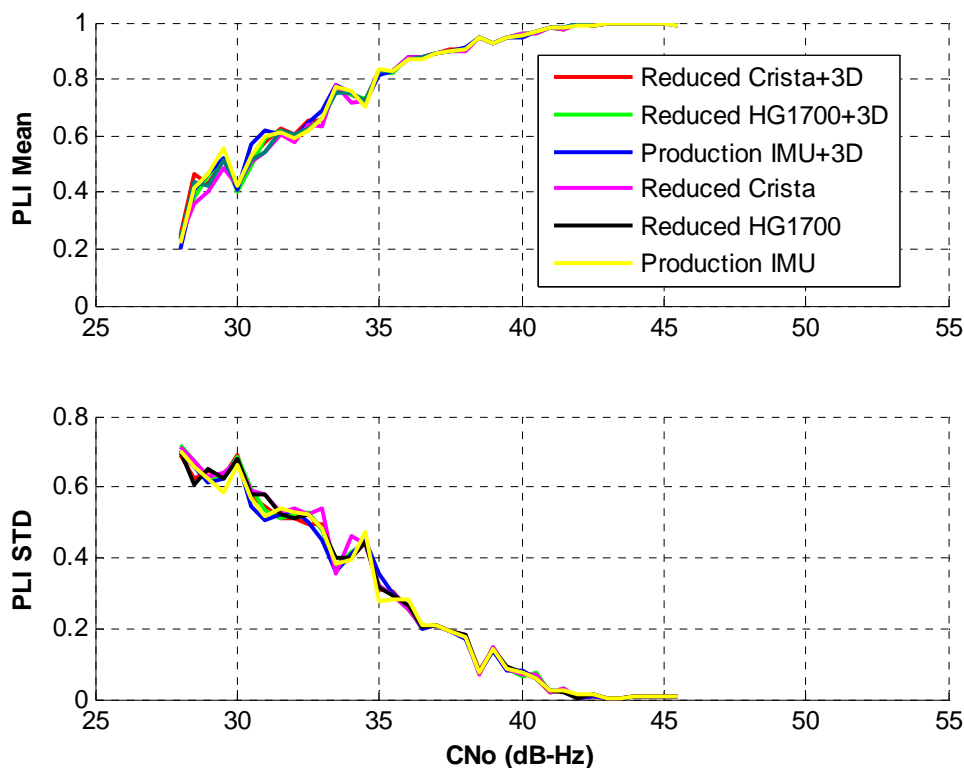


Figure 5.36: Mean and standard deviation of PLI as a function of  $C/N_0$  for PRN 23

### Ultra-tight GPS/Reduced IMUs with Three-Dimensional Velocity Updates

The final tracking-domain analysis investigates the performance of the ultra-tight integration of reduced IMUs when 3-Dimensional velocity updates are used. Figure 5.37 and Figure 5.38 show the mean and standard deviation of PLI values as a function of  $C/N_0$  for different receiver architectures and with different sensors. The contribution of the 3D velocity updates to the tracking improvement is minimal. The three different reduced IMU systems with different sensor qualities have nearly the same performance. Therefore, the quality and sensor configurations play a minor roll in the tracking performance for the ultra-tight receiver. However, in the navigation domain, different sensors indeed perform differently.



**Figure 5.37: Mean and standard deviation of PLI as a function of  $C/N_0$  for PRN 4**

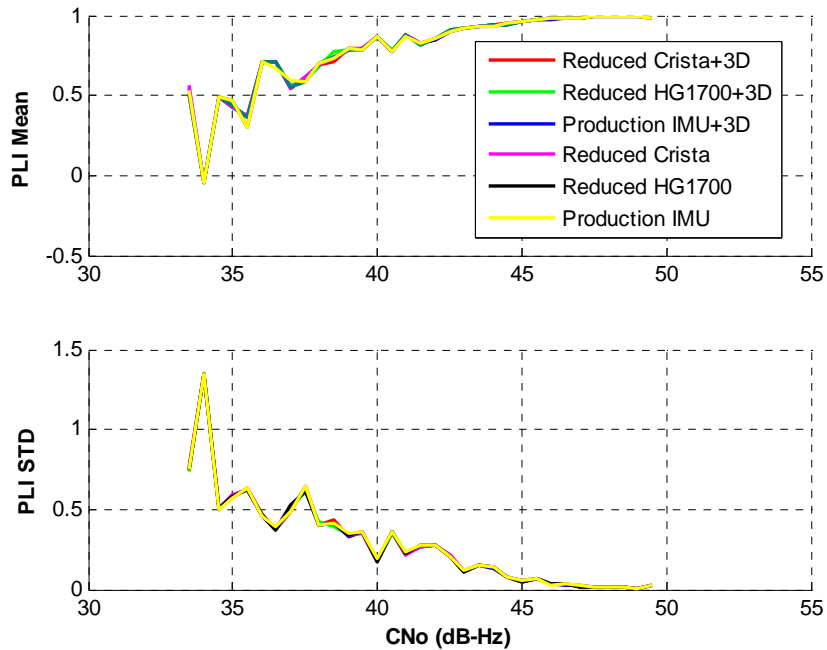


**Figure 5.38: Mean and standard deviation of PLI as a function of  $C/N_0$  for PRN 23**

### 5.5.2 Navigation domain

Having analyzed the tracking performance of ultra-tight receiver under foliage test, the navigation accuracy is presented in the following. Similar analysis procedure as in the open sky test is used to assess the performance of the ultra-tight integration in the foliage scenario.

#### Reference solution

Similar to the open sky scenario, the reference solution is generated by the loose integration of DGPS and HG1700. The velocity and attitude of the vehicle during the foliage test are shown in Figure 5.39 and Figure 5.40, respectively. Since the foliage test was conducted in a relatively flat road, the pitch and roll of the vehicle are smaller compared with those of the open sky test.

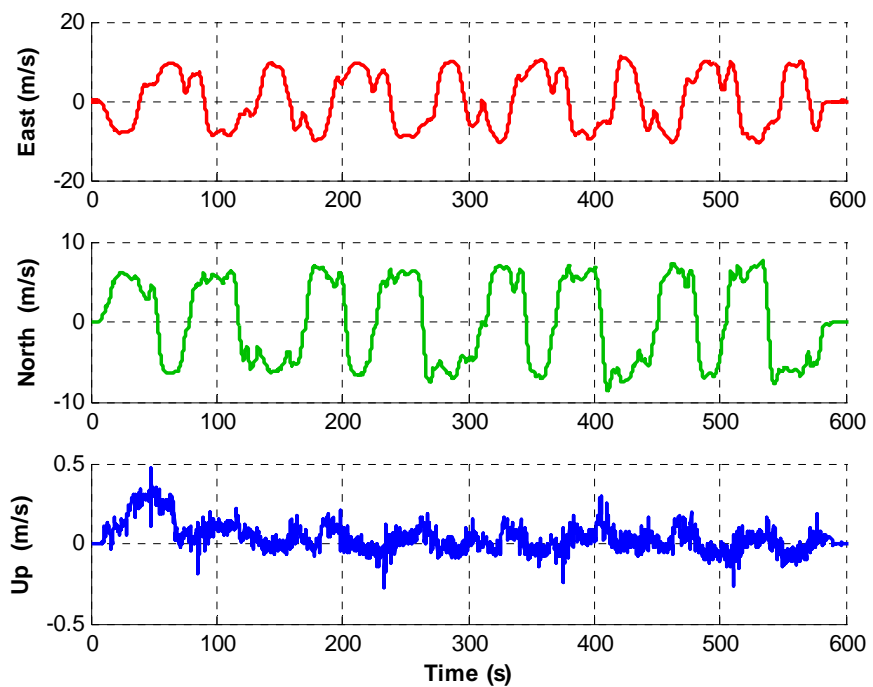


**Figure 5.39: Reference velocity plots of the foliage test**

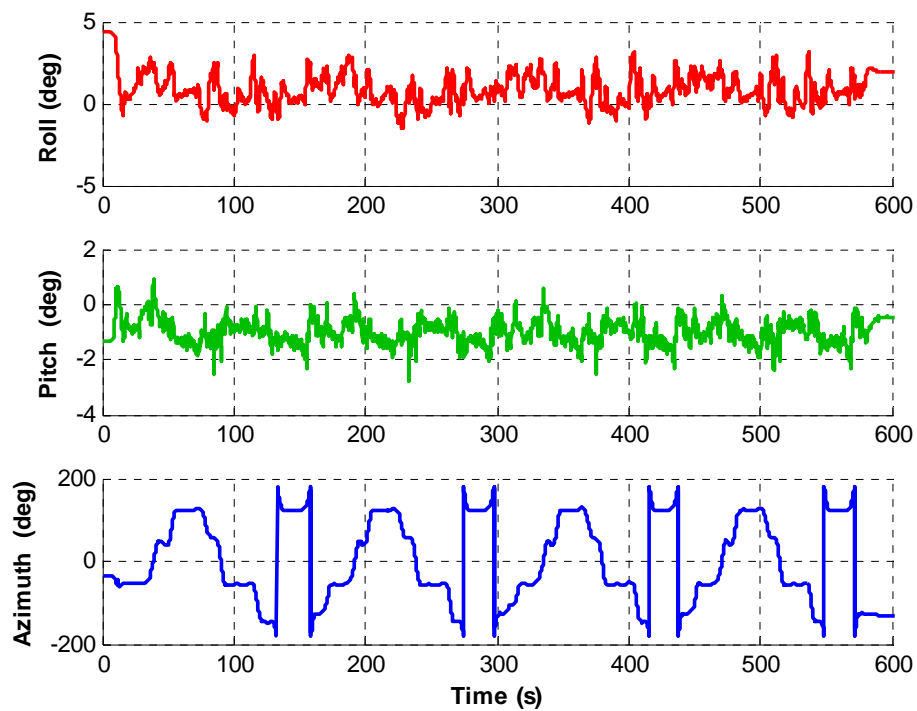


**Figure 5.40: Reference attitude plots of the foliage test**

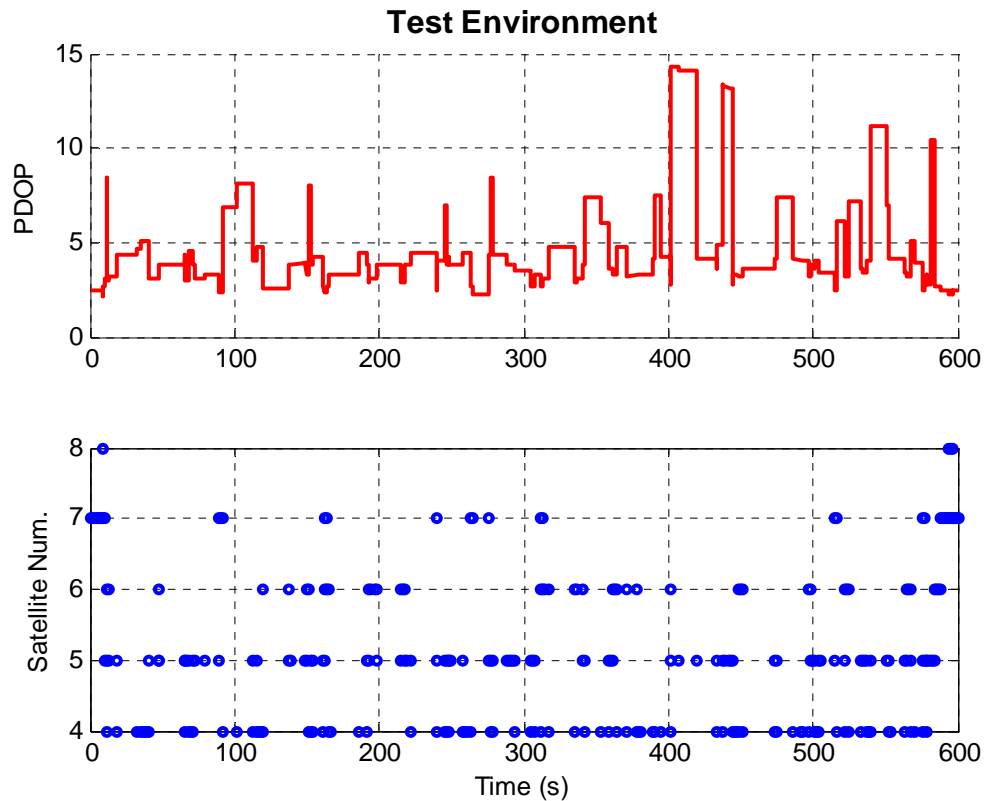


**Figure 5.41: PDOP and satellite number plots of the foliage test**

The PDOP and number of satellites computed from the reference solution are shown in Figure 5.41. The satellite number used for generating the navigation solution is between four and eight but there are many cases where fewer than four satellites were available. The PDOP varies with the number of satellite. The maximum PDOP values reach 15.

### Full Crista IMU

Firstly, when the full Crista IMU is employed, the RMS velocity and attitude errors are listed in Table 5.12 and the RMS position error in Table 5.13.

**Table 5.12: Velocity and attitude errors for full Crista IMU**

Constraint	Velocity (m/s)			Attitude (deg)		
	V <sub>e</sub>	V <sub>n</sub>	V <sub>u</sub>	Roll	Pitch	Azimuth
<b>None</b>	0.12	0.12	0.15	0.60	0.63	1.46
<b>WSS</b>	0.12	0.12	0.15	0.65	0.56	1.30
<b>Lateral</b>	0.12	0.12	0.15	0.48	0.63	1.28
<b>Vertical</b>	0.12	0.12	0.15	0.65	0.63	1.46
<b>L+WSS</b>	0.12	0.12	0.15	0.47	0.56	1.28
<b>2D</b>	0.12	0.12	0.15	0.48	0.63	1.29
<b>3D</b>	0.12	0.12	0.15	0.47	0.56	1.28

**Table 5.13: RMS position errors for full Crista**

Constraint	Position Error (m/s)		
	East	North	Up
<b>None</b>	4.55	4.84	5.02
<b>3D</b>	3.01	3.32	3.34

According to the results listed in Table 5.12 and Table 5.13, similar conclusions as for the open sky scenario can be drawn. Firstly, the 3D velocity updates improve both attitude and position estimates. Secondly, the lateral and wheel speed sensor derived velocity updates play a major roll in the navigation performance improvement. Thirdly, no noticeable velocity improvement is obtained by using 3D velocity updates. Figure 5.42 shows the velocity and attitude errors using the full Crista MEMS IMU with 3D velocity updates in the foliage test.

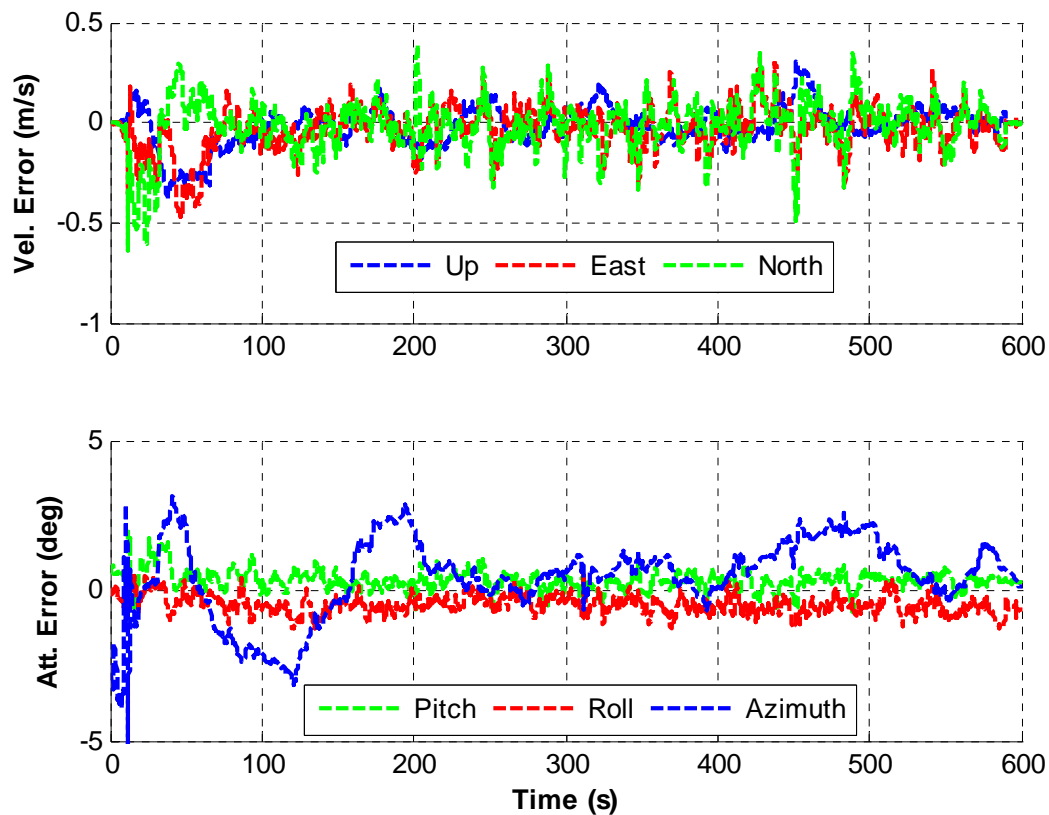


**Figure 5.42: Velocity and attitude error plots for full Crista IMU**

### Reduced IMUs

When reduced IMU is employed in the ultra-tight receiver, the RMS velocity and attitude errors in the foliage scenario are listed in Table 5.14 and the corresponding RMS position errors in Table 5.15.

**Table 5.14: Velocity and attitude errors for reduced IMUs**

Sensors		Velocity (m/s)			Attitude (deg)		
		V <sub>e</sub>	V <sub>n</sub>	V <sub>u</sub>	Roll	Pitch	Azimuth
None	<b>HG1700</b>	0.12	0.12	0.15	1.21	1.07	2.07
	<b>Crista</b>	0.12	0.12	0.15	1.35	1.08	2.72
	<b>Production</b>	0.12	0.12	0.15	1.32	1.08	2.56
3D	<b>HG1700</b>	0.12	0.12	0.15	1.18	1.01	1.12
	<b>Crista</b>	0.12	0.12	0.15	1.30	1.03	1.57
	<b>Production</b>	0.12	0.12	0.15	1.31	1.03	1.46

**Table 5.15: RMS position errors for reduced IMUs**

Sensors		Position Error (m/s)		
		East	North	Up
None	<b>HG1700</b>	3.89	3.84	5.56
	<b>Crista</b>	3.98	3.76	5.78
	<b>Production</b>	3.90	3.70	5.71
3D	<b>HG1700</b>	3.21	3.57	3.69
	<b>Crista</b>	3.24	3.55	3.81
	<b>Production</b>	3.23	3.52	3.77

Compared with the results in the open sky scenario, the position velocity and attitude accuracies are all degraded due to the decreased satellite visibility under the tree canopy.

Similar to the results of the open sky test, the position, velocity, roll and pitch accuracies stay at the same level for all IMUs. The reason, which has been explained when discussing the the open sky test, is that the position and velocity accuracy of the reduced system mainly depends on the GPS measurements. Furthermore, the roll and pitch

accuracy relies on the local terrain and vehicle dynamics and the azimuth estimates are related to the gyro quality. Therefore, the reduced HG1700 has better azimuth estimates.

Finally, the position and velocity errors of the standard GPS receiver are listed in Table 5.16. It is clear that the ultra-tight GPS receiver with different sensor configurations has better positioning performance in the foliage test.

**Table 5.16: RMS Position and velocity errors for standard GPS**

Position (m)			Velocity (m/s)		
East	North	Up	East	North	Up
3.99	4.09	6.52	0.60	0.71	0.55

## CHAPTER SIX: CONCLUSIONS AND RECOMMENDATIONS

The contribution of this thesis was to use wheel speed sensor to enhance the performance of ultra-tightly coupled integration with reduced low cost MEMS IMU. The performance of the system was assessed using different sensors and sensor configurations including full and reduced HG1700 and Crista IMU, and the production IMU. A field test under different operational environments was used to verify the feasibility of the ultra-tight integration with low cost vehicle sensors for land vehicle navigation application.

A pseudo-signal approach was employed for the IMU in this work because of the sensor configuration of vehicle sensors. The unavailable output signals of the reduced IMU (i.e., vertical accelerometer and horizontal gyros) were replaced by pseudo signals that have constant values plus white noise. Therefore, the outputs of the vertical accelerometer were modeled as gravity plus white noise and the two horizontal gyros were modeled as white noise. Then these pseudo signals combined with the real horizontal accelerometer and vertical gyro outputs were fed into the full IMU/GPS navigation algorithm to obtain the final navigation solution.

In order to limit the error induced by the reduced MEMS IMU/GPS integrated system, the wheel speed sensor and non-holonomic constraints derived three-dimensional velocity updates were applied in this thesis. The 3D velocity updates improved the velocity and attitude estimates of the integration filter. The improved positioning estimates in turn helped the receiver's carrier tracking loops. The benefits of each constraint including vertical, lateral and longitudinal were also analyzed.

The analysis of the processed results was performed in both the tracking domain and navigation domain. In the tracking domain, PLI was used to evaluate the receiver's carrier phase tracking ability. In the navigation domain, the RMS position, velocity and attitude errors were used to assess the performance of the navigation solutions. The above performance parameters were compared between different receiver architectures including the standard GPS receiver (without attitude information), and ultra-tightly coupled GPS receiver.

## **6.1 Conclusions**

The following conclusions can be drawn from the work presented herein:

The ultra-tight GPS receiver outperforms a standard GPS receiver in both tracking and position domains even when a low cost reduced MEMS IMU is used. The improvement of the ultra-tight receiver is as function of the  $C/N_0$ . The higher the  $C/N_0$ , the smaller improvement of PLI from the ultra-tight integration.

The quality of the IMU plays a minimal roll in the tracking performance of an ultra-tight GPS receiver. The obtained PLI of the system with HG1700, Crista and the production IMU are very similar in either open sky or foliage environments.

With a reduced IMU, the pitch and roll estimates can still be obtained without losing too much accuracy by using a pseudo-signal approach. The obtained attitude accuracy is related to GPS signal quality, vehicle dynamics and local terrain.

The integrated system with a reduced IMU has similar tracking performance as that of its corresponding full IMU configuration. This means that the velocity and position accuracy degradation induced by the omitted sensors can be neglected and therefore tracking performance remains the same.

A wheel speed sensor combined with the lateral and vertical velocity constraints can be used to further improve the MEMS and the reduced MEMS IMU/GPS system. The wheel speed sensor and lateral constraint derived velocity updates play a major role in the improvement of the velocity and attitude updates. The wheel speed sensor mainly improves the pitch and azimuth estimates and, in particular the azimuth estimates. The lateral constraint mainly improves the roll and azimuth estimates and its azimuth improvement is more pronounced compared with that of roll.

Although three-dimensional velocity updates improve the positioning accuracy of the system, they play a minimal role in the improvement of the tracking performance in both open sky and foliage scenarios.

## **6.2 Recommendations**

Based on the results and conclusions of this research, the following recommendations can be made:

Improve the modeling of the pseudo signals used in the reduced IMU integration. This thesis only applied white noise to model the unavailable inertial sensor signals. Since these pseudo signals are related with local terrain and vehicle dynamics, a more suitable

model could be used to reduce the modeling error based on the road condition and vehicle dynamics. An adaptive method is recommended to automatically detect the current vehicle operational conditions and choose the most suitable models and parameters to improve the state estimates of the integration filter.

Implement in-motion alignment algorithm for MEMS IMU. Because of the large sensor bias of the MEMS gyros, the conventional static alignment is not feasible to obtain the initial attitude. In this thesis, the initial attitude of the MEMS IMU was setup by that of HG1700. Since this is not practical in real situations, a new in-motion alignment algorithm should be developed to initialize the MEMS attitude with GPS and vehicle sensors.

Implement an algorithm to allow integration with multiple wheel speed sensors. Most modern vehicles include four wheel speed sensors. However, only one wheel speed sensor was used in this thesis. The other wheel speed sensors could potentially improve the velocity and attitude estimates. The differential front wheel velocity could provide yaw information with certain accuracy which can be used to feed into the integration filter. Besides, the averaged wheel velocity may provide a more accuracy longitudinal velocity.

Implement an algorithm to integrate with a steering angle sensor. A steering angle sensor is another common vehicle sensor inside a vehicle. It can provide information of the intended vehicle direction. Integration with a steering angle sensor could improve the

azimuth estimates of the vehicle especially when a MEMS IMU is used. In addition, this yaw information can be used to initialize the orientation of MEMS IMUs.

Apply sensor fault detection algorithm. All vehicle sensors could encounter faults. In this case, the outputs of faulty sensors should be excluded from the integration procedure to avoid degraded performance induced by the errors sensor outputs.

**REFERENCES**

- Abbott, A.S. and W.E. Lillo (2003) "Global Positioning Systems and Inertial Measuring Unit Ultratight Coupling Method," Patent, US 6,516,021 B1, United States, 22 pages.
- Alban, S., D. Akos, S. Rock (2003) "Performance Analysis and Architectures for INS-Aided GPS Tracking Loops," in *Proceedings of ION NTM 2003*, 22-24 January, Anaheim CA, pp.611-622, U.S. Institute of Navigation, Fairfax VA
- Allan D.W. (1966) "Statistics of Atomic Frequency Standards," in *Proceedings of the IEEE*, 54(2): 221, February 1966.
- Anderson, R. and D. M. Bevly (2004) "Estimation of Slip Angles Using a Model Based Estimator and GPS," in *Proceedings of the American Control Conference*. Boston, Massachusetts, pp. 2122-2127.
- Babu, R. and J. Wang (2006) "Ultra-Tight Integration of Pseudolites With INS," in *Proceedings of IEEE/ION PLANS 2006*, 25-27 April, San Diego CA, pp.705-713
- Beach and Kintner (2001) "Development and Use of a GPS Ionospheric Scintillation Monitor," *IEEE Transactions on Geoscience and Remote Sensing*, Vol. 39, No. 5, May 2001.

Beser J., S. Alexander, R. Crane, S. Rounds, J. Wyman (2002) “TRUNAV™: A Low-Cost Guidance/Navigation Unit Integrating A SAASM-Based GPS and MEMS IMU in A Deeply Coupled Mechanization,” in *Proceedings of ION GPS 2002*, 24-27 Sept., Portland OR, pp. 545-555, U.S. Institute of Navigation, Fairfax VA

Best, R. E. (1999). *Phase-Locked Loops*. McGraw-Hill.

Bevly et al. (2000) “Use of GPS based velocity measurements for improved vehicle state estimation,” in *Proceedings of the 2000 American Control Conference*, pages 2538–2542, Chicago, IL, 2000.

Bevly, R. Sheridan, and J. C. Gerdes (2001) “Integrating ins sensors with GPS velocity measurements for continuous estimation of vehicle sideslip and tire cornering stiffness,” in *Proceedings of the 2001 American Control Conference*, pages 25–30, Arlington, VA, 2001. 106

Bosch (2009) *Technical specifications*  
[http://www.bosch-esential.com/us/language1/technical\\_features.html](http://www.bosch-esential.com/us/language1/technical_features.html)

Brandit, A., J. F. Gardner (1998) “Constrained Navigation Algorithm for Strapdown Inertial Navigation Systems with Reduced Set of Sensors,” in *Proceedings of the American Control Conference 1998*, June, Philadelphia PA, pp. 1848-1852

Brenner, M. (1995) "Integrated GPS/Inertial Fault Detection Availability," in *Proceedings of ION GPS*, 12-15 September, Palm Springs CA, pp. 1949-1958, U. S. Institute of Navigation, Fairfax VA

Brown, R. G. and P. Y. C. Hwang (1992) *Introduction to Random Signal and Applied Kalman Filtering*. John Wiley & Sons, Inc., second edition.

Buck, T., J. Wilmot, M. J. Cook (2006) "A High G, MEMS Based, Deeply Integrated, INS/GPS, Guidance, Navigation and Control Flight Management Unit," in *Proceedings of IEEE/ION PLANS 2006*, 25-27 April, San Diego CA, pp.772-794

Chiou, T. (2005) "GPS Receiver Performance Using Inertial-Aided Carrier Tracking Loop," in *Proceedings of ION GNSS 2005*, 13-16 Sept, Long Beach CA, pp. 2895-2910, U.S. Institute of Navigation, Fairfax VA

Christopher R. Carlson (2003) *Estimate with applications for automobile dead reckoning and control*, Ph.D Thesis, Stanford University, USA

Clark, B.J. , Bevly, D.M. , S. Farritor (2006), "Analysis of Improvement to Two-Wheel Robot Navigation Using Low-Cost GPS/INS Aids", in *Proceedings of the ION GNSS*, Fort Worth, TX.

Curtis Hay (2005) "Wheel-Speed Dead Reckoning for Vehicle Navigation," GPS World

Daum, P., J. Beyer, T. Köhler (1994) "Aided Inertial land navigation System (ILANA) with a Minimum Set of Inertial Sensors," in *Proceedings of IEEE-IEE Vehicle Navigation & Information Systems Conference, Yokohama-VNIS'94*, pp. 284-291

Dissanayake, G., S. Sukkarieh, E. Nebot and H. DurrantWhyte (2001) "The aiding of a Low Cost Strapdown Inertial Measurement Unit using Vehicle Model Constraints for Land vehicle Applications," *IEEE Transactions on Robotics and Automation*, vol.17, no. 5, pp. 731-747.

Farrell.A.Jay (2008) *Aided Navigation: GPS with high rate sensors*, McGraw-Hill Comapany, USA

Fujiwara, T., H. Tomita, M. Harigae (2007) "Robustness Improvement of a Low Cost MEMS-based GPS/INS, Micro-GAIA," in *Proceedings of ION NTM 2007, 22-24 January, San Diego CA*, pp.736-742, U.S. Institute of Navigation, Fairfax VA

Gautier, J., B. Parkinson (2003) "Using the GPS/INS Generalized Evaluation Tool (GIGET) for the Comparison of Loosely Coupled, Tightly Coupled and Ultra-Tightly Coupled Integrated Navigation Systems," in *Proceedings of ION 59th Annual Meeting/CIGTF 22nd Guidance Test Symposium, 23-25 June, 2003, Albuquerque, NM*, pp. 65-76, U.S. Institute of Navigation, Fairfax VA

Gao, J., M.G. Petovello and M.E. Cannon (2007) "GPS/Low-Cost IMU/Onboard Vehicle Sensors Integrated Land Vehicle Positioning System," in *EURASIP Journal on Embedded Systems*, Volume 2007, Article ID 62616, 14 pages.

Gao, J. (2007) *Development of a Precise GPS/INS/On-Board Vehicle Sensors Integrated Vehicular Positioning System* PhD Thesis, Published as Report No. 20255, Department of Geomatics Engineering, The University of Calgary.

Gao, G. and G. Lachapelle (2006) "INS-Assisted High Sensitivity GPS Receivers For Degraded Signal Navigation," in *Proceedings of ION GNSS 2006*, 26-29 September, Fort Worth TX, pp. 2977-2989, U. S. Institute of Navigation, Fairfax VA

Gebre-Egziabher, D. (2007), "GNSS Solutions: Variations of GNSS/INS Integration," *Inside GNSS*, Vol 2., No. 1, pp. 28-33.

Gebre-Egziabher, D., and A. Ravzi, P. Enge, J. Gautier, S. Pullen, B. Pervan, and A. Akos (2005) "Sensitivity and Performance Analysis of Doppler-Aided GPS Carrier-Tracking Loops," *Navigation*, vol 52, no 2, Summer 2005, U.S. Institute of Navigation, Fairfax VA, pp. 49-60

Gelb, A. (1974) *Applied Optimal Estimation*. The M.I.T Press.

Gillespie, Thomas, *Fundamentals of Vehicle Dynamics*, *Society of Automotive Engineers*, Warrendale, PA, 1992.

Godha, S.(2006) *Performance Evaluation of Low Cost MEMS-Based IMU Integrated With GPS for Land Vehicle Navigation Application*, M.Sc. thesis, Department of Geomatics Engineering, University of Calgary, Canada (Available at <http://www.geomatics.ucalgary.ca/research/publications/GradTheses.html>)

Greenspan, R.L. (1996). "GPS and Inertial Integration" in Parkinson, B. W., editor, *Global Positioning System: Theory and Applications*, Volume 2, pp. 187-220, American Institute of Aeronautics and Astronautics, Washington, DC.

Grewal, M., A. P. Andrews (2001) *Kalman Filtering: Theory and Practice Using MATLAB*, John Wiley & Sons

Grewal, M. and Andrews, A. P. (1993). *Kalman Filtering: Theory and Practice Using Matlab*. John Wiley and Sons Inc.

Gustafson, D., J. Dowdle and K. Flueckiger (2000) "A Deeply Integrated Adaptive GPS-Based Navigator with Extended Range Code Tracking," *IEEE PLANS*, San Diego, CA, IEEE, 118-124.

Gunawardena, S., A. Soloviev, F. van Graas (2004) “Real Time Implementation of Deeply Integrated Software GPS Receiver and Low Cost IMU for Processing Low-CNR GPS Signals,” in *Proceedings of ION 60th Annual Meeting/U.S. Air Force Institute of Technology & The U.S. Air Force Research Laboratory*, Sensor Directorate, 7-9 June 2004, Dayton OH, pp.108-114, U.S. Institute of Navigation, Fairfax VA

Hamm, C., W. Flenniken, D. Bevly, D. Lawrence (2004) “Comparative Performance Analysis of Aided Carrier Tracking Loop Algorithms in High Noise/High Dynamic Environments,” in *Proceedings of ION GNSS 2004*, 21-24 Sept., Long beach CA, pp.523-532, U.S. Institute of Navigation, Fairfax VA

Hernańdez (2003) “Improving the response of a wheel speed sensor using an adaptive line enhancer,” *Measurement*, Volume 33, Issue 3, April 2003, Pages 229-240

Humphreys, T., M. Psiaki, P. Kintner, B. Ledvina (2005) “GPS Carrier Tracking Loop Performance in the Presence of Ionospheric Scintillations,” in *Proceedings of ION GNSS 2005*, 13-16, Sept., Long Beach CA, pp. 156-167, U.S. Institute of Navigation, Fairfax VA

IEEE Std 952-1997 *IEEE Standard Specification Format Guide and Test Procedure for Single –Axis Interferometric Fiber Optic Gyros.*

- Izadpanah A. (2009) *Parameterization of GPS L1 multipath using a dual polarized RHCP/LHCP antenna*, MSc Thesis, published as Report No. 20280, Department of Geomatics Engineering, University of Calgary, Canada.
- Jee, G.I., H.S. Kim, Y.J. Lee and C.G. Park (2002) "A GPS C/A Code Tracking Loop Based on Extended Kalman Filter with Multipath Mitigation," in *Proceedings of ION GPS 2002*, Portland, OR, Institute of Navigation, 446-451.
- Jekeli, Christopher (2001) *Inertial Navigation Systems with Geodetic Applications*, Walter de Gruyter, pp.101-134
- Jovancevic, A., A. Brown, S. Ganguly, J. Noronha and B. Sirpatil (2004) "Ultra Tight Coupling Implementation Using Real Time Software Receiver," in *Proceedings of ION GNSS 2004*, Long Beach, CA, Institute of Navigation, 1575-1586.
- Kim, H.S., S.C. Bu, G.I. Jee and C.G. Park (2003) "An Ultra-Tightly Coupled GPS/INS Integration Using Federated Filtering," in *Proceedings of ION GPS/GNSS 2003*, Portland, OR, Institute of Navigation, 2878-2885.
- Kreye, C., Eissfeller, B., and Ameres, G. (2004). "Architectures of GNSS/INS Integrations: Theoretical Approach and Practical Tests," in *Symposium on Gyro Technology*, pages 14.0–14.16.

Kreye, C., B. Eissfeller, J. Winkel (2000) "Improvements of GNSS Receiver Performance Using Deeply Coupled INS Measurements," in *Proceedings of ION GPS 2000*, 19-22 Sept., Salt Lake City UT, pp. 844-854, U. S. Institute of Navigation, Fairfax VA

Kubo, J., T. Kindo, A. Ito and S. Sugimoto (1999) "DGPS/INS/Wheel Sensor Integration for High Accuracy Land-Vehicle Positioning" in *Proceedings of ION GPS 1999*, September, Nashville, TN, pp. 555-564

Kouba J, Heroux P (2001) "Precise point positioning using IGS orbit and clock products," *GPS Solution* 5(2):12–28

Lachapelle, G. (2007) *Advanced GNSS Theory and Applications, ENGO625 Course Notes*, Department of Geomatics Engineering, University of Calgary, Canada

Lashley (2006), *Kalman filter tracking algorithm for software GPS receiver*, M.Sc. thesis, Department of Electrical and Computer Engineering, Auburn University, USA

Lashley and D. M. Bevly (2006), "Analysis of Discriminator Based Vector Tracking Algorithms," in *ION National Technical Meeting*, San Diego, CA, 2007, pp. 570-576.

Legrand F. and Macabiau C. (2001) "Results of the implementation of the Fast Adaptive Bandwidth Lock Loops on a real GPS receiver in a high dynamics context," in *GNSS 2001 International Symposium*, pp. 1-6.

- Li, D., J. Wang (2006a) “Kalman Filter Design Strategies for Code Tracking Loop in Ultra-Tight GPS/INS/PL Integartion,” in *Proceedings of ION NTM 2006*, 18-20 January, Monterey CA, pp.984-992, U.S. Institute of Navigation, Fairfax VA
- Li, D., J. Wang (2006b) “System Design and Performance Analysis of Extended Kalman Filter-Based Ultra-Tight GPS/INS Integration,” in *Proceedings of IEEE/ION PLANS 2006*, 25-27 April, San Diego CA, pp.291-299
- Li, T., M.G. Petovello, G. Lachapelle and C. Basnayake (2009) “Performance Evaluation of Ultra-tight Integration of GPS/Vehicle Sensors for Land Vehicle Navigation,” in *Proceedings of GNSS09* (Savannah, GA, 22-25 Sep, Session D2), The Institute of Navigation, 12 pp.
- Li, Y., J. Wang, C. Rizos, P. Mumford, and W. Ding (2006c) “ Low-cost Tightly Coupled GPS/INS Integration Based on a Nonlinear Kalman Filter Design,” in *Proceedings of ION NTM 2006*, 18-20 January, Monterey CA, pp.958-966, U.S. Institute of Navigation, Fairfax VA
- Lian, P. (2004) *Improving Tracking Performance of PLL in High Dynamic Applications*. MSc Thesis, published as UCGE Report No. 20208, Department of Geomatics Engineering, University of Calgary, Canada.

Liebemann, E. K., K. Meder, J. Schuh and G. Nenninger, "Safety and Performance Enhancement: the Bosch Electronic Stability Control (ESP)." *SAE 2004-21-0060*.

Misra, P. and Enge, P. (2001). *Global Positioning System Signals, measurements and performance*. Ganga-Jamuna Press.

N. El-Sheimy (2008) "Inertial Techniques and INS/DGPS Integration," *ENGO699.64 Course Notes*, Department of Geomatics Engineering, University of Calgary.

Niu, X., Nassar, S. and El-Sheimy, N. (2007a) "An Accurate Land-Vehicle MEMS IMU/GPS Navigation System Using 3D Auxiliary Velocity Updates," in *Journal of the Institute of Navigation, USA.*, vol 54, no 3, pp.177-188

Niu, X., S. Nasser, C. Goodall, and N. El-Sheimy (2007b) "A Universal Approach for Processing any MEMS Inertial Sensor Configuration for Land-Vehicle Navigation," in *The Journal of Navigation*, vol 60, no 2, *The Royal Institute of Navigation*, pp.233-245

Numajima, T., M. Kihara, Y. Kubo and T. Seki (2002) "INS/DGPS/VMS Integration for In-motion Alignment" in *Proceedings of ION GPS 2002*, September, Portland, VR, pp. 556-564.

O'Driscoll, C., M.G. Petovello and G. Lachapelle (2008) "Impact of Extended Coherent Integration Times on Weak Signal RTK in an Ultra-Tight Receiver," in *Proceedings of NAV08 Conference*, Royal Institute of Navigation, London, 28-30 October, 11 pages.

Ohlmeyer, E. J. (2006) "Analysis of an Ultra-Tight Coupled GPS/INS System in Jamming," in *Proceedings of IEEE/ION PLANS 2006*, 25-27 April, San Diego CA, pp. 44-53.

Ouladsine, Hassan Shraim, Leonid Fridman and and Hassan Noura (2008), "Vehicle Parameter Estimation and Stability Enhancement using the Principles of Sliding Mode," in *Proceedings of 2007 American Control Conference*, Newyork, USA.

Pany, T., and B. Eissfeller (2006) "Use of a Vector Delay Lock Loop Receiver for GNSS Signal Power Analysis in Bad Signal Conditions," in *Proceedings of IEEE/ION PLANS 2006*, 25-27 April, San Diego CA, pp. 893-903

Pany, T., R. Kaniuth, and B. Eissfeller (2005) "Deep Integration of Navigation Solution and Signal Processing," in *Proceedings of ION GNSS 2005*, 13-16 Sept., Long Beach CA, pp. 1095-1102, U.S. Institute of Navigation, Fairfax VA

Phuyal, B. (2004). "An Experiment for a 2-D and 3-D GPS/INS Configuration for Land Vehicle Applications," in *Proceedings of the IEEE Position Location and Navigation Symposium (PLANS 2004)*, Monterey, California, USA, April 26-29, 148-152

Petovello, M., C. O'Driscoll and G. Lachapelle (2008a) "Weak Signal Carrier Tracking of Weak Using Using Coherent Integration with an Ultra-Tight GNSS/IMU Receiver," *in Proceedings of European Navigation Conference* (Toulouse, 23-25 April), 11 pages.

Petovello, M., C. O'Driscoll and G. Lachapelle (2008b) "Carrier Phase Tracking of Weak Signals Using Different Receiver Architectures," *in Proceedings of ION NTM08* (San Diego, 28-30 Jan, Session A4). The Institute of Navigation, 11 pages.

Petovello, M.G., C. O'Driscoll and G. Lachapelle (2007) "Ultra-Tight GPS/INS for Carrier Phase Positioning in Weak Signal Environment.," NATO RTO SET-104 Symposium on Military Capabilities Enabled by Advances in Navigation Sensors, Antalya, Turkey, 1-2 October 2007, 18 pages.

Petovello, M., and G. Lachapelle (2006) "Comparison of Vector-Based Software Receiver Implementations with Application to Ultra-Tight GPS/INS Integration," *in Proceedings of ION GNSS 2006*, 26-29 Sept., Fort Worth TX, pp.2977-2989, U.S. Institute of Navigation, Fairfax VA

Petovello, M. (2003) *Real-Time Integration of a Tactical-Grade IMU and GPS for High-Accuracy Position and Navigation*, Ph. D. Dissertation, Department of Geomatics Engineering, University of Calgary, Canada (Available at <http://plan.geomatics.ucalgary.ca>)

Psiaki, M., H. Jung (2002) "Extended Kalman Filter Methods for Tracking Weak GPS Signals," in *Proceedings of ION GPS 2002*, 24-27 Sept., Portland OR, pp. 2539-2553, U.S. Institute of Navigation, Fairfax VA

Psiaki, M, Humphreys, T, Cerruti, Paul,S, Kintner (2007) "Tracking L1 C/A and L2C Signals through Ionospheric Scintillations," in *Proceedings of GNSS 2007*, 25-28 Sept., Fort Worth, Texas, USA

”

Psiaki, M. (2001) "Smoother-Based GPS Signal Tracking in a Software Receiver," in *Proceedings of ION GPS 2001*, 11-14 Sept., Salt Lake City UT, pp. 2900-2913, U.S. Institute of Navigation, Fairfax VA

Ray, L.R. (1995) "Nonlinear State and Tire Force Estimation for Advanced Vehicle Control", in *IEEE Transactions on Control System Technology*, vol.3, no. 1, 1995, pp. 117-124.

Rajamani (2008) *Vehicle Dynamics and Control*, springer ,USA

Rogers R.M. (2007) *Applied Mathematics in Integrated Navigation Systems*. American Institute of Aeronautics and Astronautics, Inc., Reston, VA, USA

Rogers R.M. (2000) *Applied Mathematics in Integrated Navigation Systems*. American Institute of Aeronautics and Astronautics, Inc., Reston, VA, USA

Ryu and J. C. Gerdes (2004) “Integrating inertial sensors with GPS for vehicle dynamics control,” in *ASME Journal of Dynamic Systems, Measurement, and Control*, 2004.

Savage, P.G. (2000) *Strapdown Analytics*, Volume 1. Strapdown Associates, Inc, Maple Plain, MA, USA.

Shin, E.H. (2005) *Estimation Techniques for Low-Cost Inertial Navigation*, Ph.D thesis, Department of Geomatics Engineering, University of Calgary, Canada

Shin, E.H. (2001) *Accuracy Improvement of Low Cost INS/GPS for Land Applications*, M.Sc. thesis, Department of Geomatics Engineering, University of Calgary, Canada

Shin, E.-H. and El-Sheimy, N. (2004). “An Unscented Kalman Filter for In-Motion Alignment of Low-Cost IMUs,” in *Proceedings of IEEE Position, Location, and Navigation Symposium*, pages 273–279, Monterey, CA.

Shraim, Mustapha Ouladsine, and Leonid Fridman (2008), “Vehicle Parameter and States Estimation Via Sliding Mode Observers,” *Modern Sliding Mode Control Theory*, Springer

Soloviev, A., D. Bruckner, F. van Graas and L. Marti (2007) “Assessment of GPS Signal Quality in Urban Environments Using Deeply Integrated GPS/IMU,” in *Proceedings of ION NTM 2007*, 22-24 January, San Diego, CA, pp. 815-828, U.S. Institute of Navigation, Fairfax VA

Spangenberg, V. Calmettes, D. Kubrak, and O. Julien (2007) “Optimized low-cost HSGPS/IMU/WSS land vehicle navigation system for urban navigation,” in *Proceedings of the 20th International Technical Meeting of the Satellite Division of the Institute of Navigation (ION GNSS '07)*, pp. 70–78, USA.

Spilker, J.J. Jr (1996). “GPS Signal Structure and Theoretical Performance,” in Parkinson, B. W., editor, *Global Positioning System: Theory and Applications*, Vol 1, American Institute of Aeronautics and Astronautics, Washington, DC.

Sun, D., M. Petovello and M.E. Cannon (2008) “GPS/Reduced IMU with a Local Terrain Predictor in Land Vehicle Navigation,” in *International Journal of Navigation and Observation*, Volume 2008

Titterton and Weston (2004) *Strapdown Inertial Navigation Technology-2nd Edition*, The Institution of Electrical Engineers

Tsui, J.B. (2000) *Fundamentals of Global Positioning System Receivers: A Software Approach*. John Wiley & Sons, Inc.

- Yang, Y., El-Sheimy, N. (2006) “Improving GPS Receiver Tracking Performance of PLL by MEMS IMU aiding,” in *Proceedings of ION GNSS 2006*, Forth Worth, TX, US, pp. 2192-2201.
- Yang Yong (2008) *Tightly Coupled MEMS INS/GPS Integration with INS Aided Receiver Tracking Loops*, (Ph.D. Thesis), UCGE Report 20270. Department of Geomatics Engineering, University of Calgary.
- Yu, W. (2007) *Selected GPS Receiver Enhancements for Weak Signal Acquisition and Tracking*, MSc Thesis, published as Report No. 20249, Department of Geomatics Engineering, University of Calgary, Canada.
- Yu, W., G. Lachapelle and S. Skone (2006) “PLL Performance for Signals in the Presence of Thermal Noise, Phase Noise, and Ionospheric Scintillation,” in *Proceedings of the 19th International Technical Meeting of the Satellite Division of the Institute of Navigation ION GNSS 2006*, ION, Fort Worth, Texas.
- Van Dierendonck, A. J. V. (1996) “GPS receivers,” in Parkinson, B. W., editor, *Global Positioning System: Theory and Applications*, Vol 1, American Institute of Aeronautics and Astronautics, Washington, DC.

Ward, P.W., J.W. Betz and C.J. Hegarty (2006) "Satellite Signal Acquisition, Tracking, and Data Demodulation," *Understanding GPS Principles and Applications*, E. D. Kaplan and C. J. Hegarty, Norwood, MA, Artech House, Inc., 153-241.

Wong, J.Y., *Theory of Ground Vehicles*, Wiley-Interscience Publication, New York, 1993.

Ziedan, Nesreen and Garrison, James L. (2004) "Extended Kalman Filter-Based Tracking of Weak GPS Signals Under High Dynamic Conditions," *in proceeding of ION GNSS 2004*, September 21-24, 2004, Long Beach, CA.

Ziedan, N.I. (2006) *GNSS Receivers for Weak Signals*, Artech House, Norwood, MA, USA